Experimental Study of Non-resolved Active Polarimetry for Space Surveillance

by

Michael C. Pasqual

S.M., Aeronautics and Astronautics, Massachusetts Institute of Technology (2010)
S.M., Technology and Policy, Massachusetts Institute of Technology (2010)
B.S.E., Electrical Engineering, Princeton University (2005)

Submitted to the Department of Aeronautics and Astronautics
in Partial Fulfillment of the Requirements for the Degree of

Doctor of Philosophy

at the
Massachusetts Institute of Technology
June 2016

Signature of Author .... Signature redacted
Department of Aeronautics and Astronautics
May 19, 2016

Certified by .... Signature redacted
Kerri L. Cahoy
Assistant Professor of Aeronautics and Astronautics
Thesis Supervisor

Certified by .... Signature redacted
Olivier L. de Weck
Professor of Aeronautics and Astronautics
Thesis Committee Member

Certified by .... Signature redacted
Eric L. Hines
Senior Technical Staff, MIT Lincoln Laboratory
Thesis Committee Member

Accepted by .... Signature redacted
Paulo C. Lozano
Associate Professor of Aeronautics and Astronautics
Chair, Graduate Program Committee

This page has been intentionally left blank.

Disclaimer

This material is based upon work supported by the United States Air Force under Air Force Contract No. FA8721-05-C-0002 and/or FA8702-15-D-0001. Any opinions, findings and conclusions or recommendations expressed in this material are those of the author and do not necessarily reflect the views of the United States Air Force.

This page has been intentionally left blank.

Experimental Study of Non-resolved Active Polarimetry
for Space Surveillance

by

Michael C. Pasqual

Submitted to the Department of Aeronautics and Astronautics
on May 19, 2016 in Partial Fulfillment of the
Requirements for the Degree of
Doctor of Philosophy

ABSTRACT

Man-made space debris constitutes a major threat to the future of the space enterprise. The space surveillance community continually seeks more efficient and robust techniques for detecting and characterizing on-orbit debris. This thesis investigates the potential utility of a technique known as active polarimetry, by which a laser radar would illuminate a space object with polarized light and measure the polarization state of the reflected light. A debris fragment's polarimetric signature can help identify its material, shape, and orientation, and, by inference, its mass, origin, and other characteristics. The research takes both an experimental and modeling and simulation approach A bench-top polarimeter (λ = 1064 nm) is used to determine the polarimetric Bidirectional Reflectance Distribution Function (BRDF) of several common spacecraft materials and coatings, including glossy white paint, matte black paint, black Kapton®, silver Teflon®, aluminum, and titanium. Measurements are made in both bistatic (in-plane scans for incident angles of 15°, 30°, 45°, 60°, and 75°) and monostatic (incident angles from 0° to 90°) geometries. The Mueller matrix of each material is then estimated as a function of the illumination and viewing angles. The results reveal notable trends in the materials' geometry-dependent polarimetric properties, particularly diattenuation (D), retardance (R), and depolarization power (Δ). At specular points, metallic surfaces (i.e., aluminum and titanium) exhibit mirror-like behavior ($D = 0$, $R = 180°$, $\Delta = 0$), while paints and thin films (e.g., Kapton®) are diattenuating ($D > 0$). All the materials tend to be more depolarizing in the monostatic diffuse regime. Silver Teflon® follows the trends of a metallic surface, with the exception of its distinct retardance at the specular point ($R = 115°$) and range of retardance values in the bistatic diffuse region ($R = 70°$ to $120°$).

Since measurements of on-orbit space debris will nominally be non-resolved (in angle), a simulation is also developed (and validated by experiments) to predict the polarimetric signature of non-resolved objects, given the measured polarimetric BRDFs of their constituent materials. The simulation is used to explore object signatures in a variety of engagement scenarios, including monostatic interrogations of stationary and tumbling objects with representative shapes (i.e., panels, spheres, and cylinders), as well as bistatic interrogations of objects with strong specular reflections. The results demonstrate that the signature of a non-resolved object is complex, but can be described as the weighted sum of the geometry-dependent polarimetric behaviors of its facets. In some cases, the signature bears a close resemblance to the behavior of the constituent material, e.g., a white-painted sphere exhibits $D = 0$, $R = 180°$, and $\Delta = 0.88$ in a monostatic geometry, which matches the behavior of glossy white paint in the monostatic diffuse regime. In other cases, the signature is unlike the behavior of any individual facet due to the way the facets' behaviors combine geometrically, e.g., a black-painted sphere exhibits $\Delta = 0.67$, unlike the behavior of matte black paint at any angle ($\Delta < 0.4$). It is shown that the effective Mueller matrix of a fast tumbling object is simply the average Mueller matrix of the object over all orientations.

The results reveal several opportunities for exploiting the signatures of non-resolved objects, at least in the context of the specific materials and shapes considered in this study. The signature of a stationary or slowly tumbling object can help exclude certain material identities, e.g., a slowly tumbling panel-shaped object with a diattenuation of $D > 0.5$ (or polarizance $P > 0.5$) cannot be metallic based on the distribution of possible signatures of metal surfaces. A fast-tumbling panel-shaped object covered in silver Teflon® exhibits the characteristic retardance ($R = 115°$) of silver Teflon® in a monostatic geometry. The monostatic signature of a fast tumbling object can still be indicative of its shape, e.g., a white-painted sphere exhibits a distinctly high depolarization power ($\Delta = 0.88$) compared to the low depolarization power ($\Delta < 0.12$) of a fast tumbling panel-shaped object or cylinder with the same coating. Since a passive system can only estimate an object's polarizance (P), current optical telescopes would not be able to determine and exploit many of these distinguishing features such as retardance and depolarization power.

Several operational schemes for interrogating space objects with a ground-based polarimetric laser radar are proposed, including short- and long-duration interrogations and interrogations whose measurements are synchronized with the tumbling period of the object. The utility of polarimetric features is discussed in terms of their ability to discriminate between objects with different materials, shapes, and orientations, as well as to obtain fingerprints that can be used to identify objects in the future and monitor their changes. A look-up table is proposed to determine the number and types of measurements required for estimating different polarimetric properties. The table may be referenced to optimally plan a measurement campaign in the field that maximizes the number of objects measurable in a given period of time. The simulation tools and experimental configuration developed for this research are generally useful for assessing the utility of active polarimetry for other applications.

Thesis Supervisor: Kerri L. Cahoy
Title: Assistant Professor of Aeronautics and Astronautics

Acknowledgements

My time at MIT would not have been nearly as successful, exciting, or enjoyable without the help and support of the following people.

First, I would like to thank my advisor Prof. Kerri Cahoy for accepting me into the Space Telecommunications, Astronomy, and Radiation Laboratory (STAR Lab). Kerri's expertise and technical guidance were invaluable throughout this research endeavor. I also thank Kerri for her constant enthusiasm and encouragement, which gave me the confidence to pursue new ideas and publish my research.

I thank Prof. Oli de Weck, who served as both my Master's advisor and a member of my Doctoral Committee, for his mentorship throughout my graduate education.

I thank Dr. Eric Hines, who served as my final core Committee member, for his technical guidance on my research and mentorship throughout my engineering career.

I thank Dr. Amanda Bosch and Dr. Michael Hecht, who served as External Readers at my Thesis Defense, for their expertise and feedback.

I would also like to thank my best friend and wife Marianne for loving and supporting me in every way throughout my MIT career.

I owe the same gratitude to Marianne's mother, father, and sister.

Last but not least, I would like to thank my mother, father, and two brothers for their loving support throughout graduate school and my entire life before MIT. I owe all of my life's successes, past, present, and future, to their constant love, guidance, and encouragement.

This page has been intentionally left blank.

Table of Contents

This page has been intentionally left blank.

List of Figures

List of Tables

List of Symbols

c	Speed of light
h	Planck's constant
$\vec{h}_{TxRx}$	1 x 16 vector form of linear equation for measurement for polarization pair TxRx
m	3 x 3 bottom-right sub-matrix of a Mueller matrix
m_D	3 x 3 bottom-right sub-matrix of diattenuating Mueller matrix M_D
m_{ij}	Element (i,j) of a Mueller matrix
m_R	3 x 3 bottom-right sub-matrix of a retarding Mueller matrix M_R
m_Δ	3 x 3 bottom-right sub-matrix of a depolarizing Mueller matrix M_Δ
p	Object pitch
r	Object roll
r_0	Fried parameter
$\vec{s}_n$	Unit surface normal of facet n
t_{pulse}	Pulse width
v_i	Eigenvector i of covariance matrix Σ
y	Object yaw
A_c	Clear area of the receiver aperture
A_n	Area of facet n
A_r	Area of target
E_{pulse}	Pulse energy
D	Diattenuation
H	System matrix of a polarimeter
$\vec{I}$	N x 1 vector of intensity measurements
I_{TxRx}	Intensity measurement for polarization pair TxRx
K_a	Aperture illumination constant
M	4 x 4 Mueller matrix
$\hat{M}$	4 x 4 Mueller matrix normalized by m_{00}
M^{Rx}	4 x 4 Mueller matrix describing receiver optics for polarization Rx
M_D	4 x 4 Mueller matrix of a pure diattenuator
M_R	4 x 4 Mueller matrix of a pure retarder
M_Δ	4 x 4 Mueller matrix of a pure depolarizer
P	Polarizance
P_R	Power received by a laser radar
$\vec{P}$	3 x 1 polarizance vector of a Mueller matrix M
$\vec{P}_\Delta$	3 x 1 polarizance vector of a depolarizing Mueller matrixM_Δ
R	Retardance
R_{tgt}	Range to target
SNR	Signal-to-noise ratio
$\vec{S}$	4 x 1 Stokes vector
$\vec{S}^{Tx}$	4 x 1 Stokes vector with polarization Tx
$\vec{S}^{Rx}$	4 x 1 Stokes vector with polarization Rx
T	Tumbling period

T_u	Transmittivity or reflectivity for incident unpolarized light
V	4 x 4 matrix of eigenvectors of covariance matrix Σ
α_{Solar}	Solar absorptivity
γ	Ratio of largest negative eigenvalue to largest positive eigenvalue of Σ
δ	Stagger time
$\varepsilon_{\mathrm{IR}}$	Infrared emissivity
η	Transmittance of atmosphere from ground to space
η_D	Quantum efficiency
η_{pol}	Transmittance of polarization filter
λ	Wavelength
λ_i	Eigenvalue i of covariance matrix Σ
λ_i^{Δ}	Eigenvalue i of depolarizing Mueller matrix M_{Δ}
σ_i	3 x 2 Pauli matrix i
θ	Scatter zenith angle for in-plane bistatic or monostatic BRDF
θ_i	Incident zenith angle
θ_s	Scatter zenith angle
θ_{T}	Beam width (or divergence)
ρ	Target reflectance
σ_D	Standard deviation on estimated diattenuation
σ_R	Standard deviation on estimated retardance
σ_{Δ}	Standard deviation on estimated depolarization power
$\vec{\sigma}_m$	16 x 1 vector of standard deviations on estimated Mueller matrix elements
ϕ_i	Incident azimuth angle
ϕ_{s}	Scatter azimuth angle
Δ	Depolarization power
Ω	Solid angle
Ω_{r}	Solid angle subtended by reflected light
Ω_{T}	Solid angle subtended by transmitted beam
Σ	4 x 4 covariance matrix
Λ	4 x 4 diagonal matrix of eignenvalues of covariance matrix Σ

List of Acronyms

+45	+45° linear polarization
-45	-45° linear polarization
AFB	Air Force Base
ASAT	Anti-Satellite
BRDF	Bidirectional Reflection Distribution Function
CSA	Chinese Space Agency
DoD	Department of Defense
ESA	European Space Agency
FAA	Federal Aviation Administration
GEO	Geostationary Orbit

H	Horizontal linear polarization
HST	Hubble Space Telescope
HWPH	Half-wave plate with horizontally-oriented fast axis
HWP+45	Half-wave plate with +45°-oriented fast axis
HWP+22.5	Half-wave plate with +22.5°-oriented fast axis
IADC	Inter-Agency Space Debris Coordination Committee
IR	Infrared
ISS	International Space Station
JAXA	Japanese Aerospace Exploration Agency
LC	Left-handed circular polarization
LEO	Low Earth Orbit
LPH	Horizontally-oriented linear polarizer
LWIR	Long-wave infrared
M&S	Model and Simulation
MEO	Medium Earth Orbit
MLI	Multi-layer insulation
MRDF	Monostatic BRDF
MSSS	Maui Space Surveillance System
NASA	National Aeronautics and Space Administration
NIR	Near infrared
PMF	Probability Mass Function
PRF	Pulse repetition frequency
QWP-45	Quarter-wave plate with -45°-oriented fast axis
RC	Right-handed circular polarization
RF	Radio frequency
Rx	Received polarization state
SSN	Space Surveillance Network
SST	Space Surveillance Telescope
Tx	Transmitted polarization state
TxRx	Pair of transmitted and received polarization states
U	Unpolarized
USSTRATCOM	United States Strategic Command
UV	Ultraviolet
V	Vertical linear polarization
VIS	Visible.

This page has been intentionally left blank.

1. Introduction

Man-made space debris is a growing problem for the continued development and operation of spacecraft [1, 2]. The increasing risk of collisions among debris and active spacecraft is changing the way mankind approaches the space enterprise, especially in the Low Earth Orbit (LEO) environment. Space agencies and organizations must consider ways to remove debris already in orbit, mitigate the creation of additional debris, and protect satellites from collisions through shielding and avoidance maneuvers [3, 4, 5, 6]. Any protection, mitigation, or removal strategy will require an accurate characterization of the space debris population, including the ephemerides, sizes, masses, tumbling behavior, and distribution of debris fragments. To this end, radars and passive optical telescopes have been able to make remote measurements of existing debris to track and characterize them in terms of radio frequency (RF), spectral, polarimetric, temporal, and orbital features [7, 8]. In the last two decades, several groups have also built ground-based laser radars for tracking space debris as small as 1 to 10 cm in size with 1 meter accuracy [9, 10, 11, 12, 13]. Despite the array of measurement methods and features used to characterize space debris today, the space surveillance community continually seeks more efficient and robust techniques for detecting and discriminating space debris [14].

One potentially valuable addition to current space surveillance capabilities is a technique known as *active polarimetry*. A laser radar could perform active polarimetry on a debris fragment or object by transmitting pulses with different polarization states and measuring the polarization state of the reflected light. As depicted in Figure 1, active polarimetry could be performed in either a monostatic geometry, in which the laser and sensor are co-located, or a bistatic geometry, in which the laser and sensor are separated in angle.

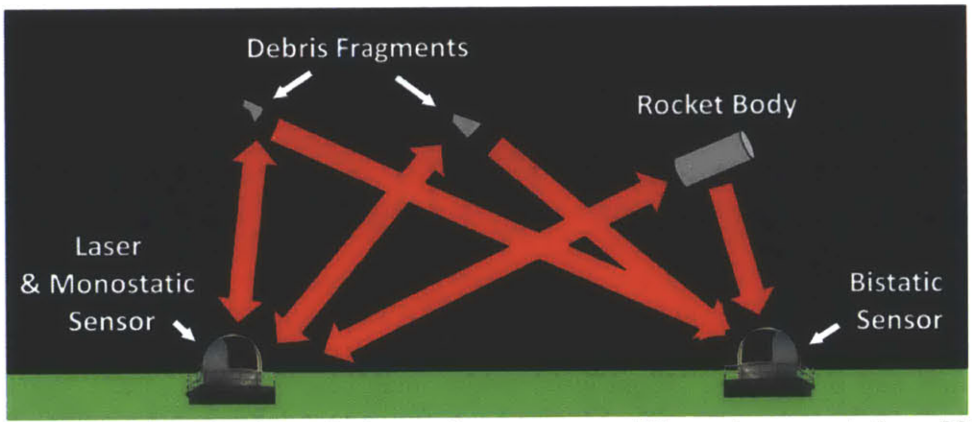

Figure 1: Illustration of active polariemtry for space surveilllance in monostatic and bistatic geometries. Original graphic created by the author.

The goal of active polarimetry would be to exploit the unique polarimetric behaviors of man-made materials, which reveal information about their surface roughness, refractive indices, and other optical properties that are difficult to obtain by other remote sensing techniques [15, 16]. Polarimetric phenomenology can be expected to vary depending on the operating wavelength of the laser and the geometry of the engagement. However, polarimetric sensing may be more robust than spectral or brightness-based techniques because polarization is unaffected by transmission through the non-birefringent atmosphere [17, 18] A high degree of polarization preservation has been demonstrated during optical transmission over a distance of 1,000 km from space to ground [19]. When combined with spectral, temporal, RF, and orbital information, the polarimetric features obtained through active polarimetry can help determine a debris fragment's material type and (by inference) its mass, as well as other important characteristics such as shape and orientation. Knowing a debris fragment's material type, mass, and geometry is critical for determining its origin and creation mechanism, tumbling behavior, ballistic coefficient and susceptibility to drag, potential to damage a spacecraft in a collision [2, 7, 20], and the feasibility of removing it from orbit [21].

Active polarimetry stands in contrast to the *passive* form of polarimetry that is currently used for space surveillance, whereby a telescope measures the polarization state of sunlight that has reflected from a space object [17, 20, 22, 23, 24, 25]. Compared to the passive method, active polarimetry is able to characterize many more dimensions of a target's polarimetric signature (Chapter 2), albeit at the cost of having to provide a light source with polarization control. Specifically, passive polarimetry only enables the estimation of a target's *polarizance*, or ability to induce polarization onto incident unpolarized light, whereas active polarimetry enables one to estimate the complete polarimetric behavior of a target, as described by its *Mueller matrix* and associated polarimetric properties, including *diattenuation*, *retardance*, and *depolarization power*. Just as optical telescopes are equipped to make passive polarimetric measurements, laser radars could be designed or augmented to perform active polarimetry on space objects. Many radar systems can already perform active polarimetry with radio waves, but their sensitivity to surface roughness and small features is limited by their relatively long operating wavelengths (centimeters) [26, 27]. Thus, relative to the polarimetric information obtainable by both optical telescopes and radar systems, the additional polarimetric features provided by a polarimetric laser radar (i.e., an active system at an optical wavelength) may improve the ability to detect and discriminate space debris.

In this thesis, the potential utility of active polarimetry for space surveillance is investigated with an emphasis on understanding the expected phenomenology. Space surveillance would be a unique application of active polarimetry because the measurements of debris object would almost always be non-resolved in angle (as opposed to resolved images), assuming a ground-based laser radar system. The signature of a non-resolved object is expected to be an aggregate of the polarimetric behavior of it surface facets, depending on the polarization-dependent Bidirectional Reflectance Distribution Function (BRDF) of the material(s) covering each facet at the operating wavelength. In addition to being non-resolved, debris objects will be moving in both position and orientation. Significant motion may blur the polarimetric signature of an object relative to the stationary case. Studies have shown that debris can have tumbling rates as high as 10s of degrees per second [20, 28], but the majority (75%) have rates less than 0.5°/s [29]. LEO objects have orbital velocities of ~7.5 km/s, causing additional apparent tumbling relative to an observer on the ground and requiring slewing of the laser and receiver [30].

Previous studies have made bench-top measurements of the polarimetric features of "coupon" samples of spacecraft materials, but only over a limited range of geometries and without consideration of the polarimetric signature of non-resolved objects [14, 31, 32, 33] . To address this gap, this research takes an experimental and modeling and simulation (M&S) approach to empirically determine the polarimetric BRDF of spacecraft materials (at a wavelength of λ = 1064 nm) and then simulate the polarimetric signatures of non-resolved objects made of or covered with those materials. The results of these experiments (Chapters 3 and 4) and simulations (Chapter 5) and their implications for the utility of active polarimetry for space surveillance (Chapter 6) are presented in this thesis.

The remainder of this chapter provides the motivation for this thesis and the chosen research approach. The discussion begins with an historical synopsis of the threat of space debris and the state of the art of space debris characterization techniques. Active polarimetry is proposed as a potentially useful technique for space surveillance, given the success of polarimetry in many other fields and application areas. Previous uses and studies of both passive and active polarimetry for space surveillance are discussed in terms of demonstrated utility and limitations. The chapter concludes with a description of the experimental and M&S approach taken in this research.

1.1. History of Space Debris

Space debris is defined as "any man-made object in orbit about the Earth which no longer serves a useful function," which includes non-functional spacecraft, rocket bodies, mission-related debris, and fragmentation debris [2, 7]. There are three primary mechanisms for the creation of space debris: operational activites, satellite deteoriation, and satellite fragmentations. *Operational actvities* create the largest (several meters) and most massive (100s to 1000s of kg) pieces of space debris in the form of spent rocket stages, including parking orbit stages (deorbiting within days), transfer orbit stages (deorbiting in years or 10s of years), and final stages (deorbiting in >10 years, unless intentionally deorbited). Smaller debris is generated by the explosive bolts used during deployment and staging events. Solid-fuel stages also eject gigantic amounts (10^{20}) of alunium particles (10 μm) per firing. Other examples of space debris from operational activites include inactive or retired satellites and planned experiments like Project West Ford, which intentionally introduced 300 million copper diopoles into medium Earth orbit (MEO) for a military communuications experiment [34].

Another key source of space debris is *satellite deterioration* due to erosion by atomic oxygen and solar radiation [2]. Atomic oxygen in LEO is known to strip the paint and coatings off satellite surfaces, including the Space Shuttle and the International Space Station (ISS). Solar radiation has also caused spent Delta second stages to explode due to propellants accidentally mixing upon the heat-induced rupture of internal membranes.

Finally, the largest source of space debris is related to *satellite fragmentations* [2]. Satellite breakups can occur for a variety of reasons, including deliberate acts [e.g., anti-satellite (ASAT) tests] and accidental events [e.g., explosions of stages during operation (as opposed to the deteoration of spent stages) and collisions among satellites and exisiting debris]. The reality of the space debris problem was highlighted by two major satellite breakups in the last decade, one intentional and one accidental. The intentional one occurred in 2007, when China successfully tested an ASAT weapon on an old Chinese weather satellite designated Fengyun-1C [35]. As indicated in Figure 2, this event created over 3,000 pieces of detectable space debris (over 5 cm each) and an estimated 35,000 smaller (1 cm) pieces. The event constitutes the single worst contamination of the LEO environment in the last 50 years. More recently in 2009, an accidental hypervelocity collision occurred between two LEO satellites [36]. One was Iridium 33, an operational US communications satellite, and the other was Cosmos 225, a decommissioned Russian communications satellite. As indicated in Figure 2, the collision spawned thousands of pieces of catalogued space debris. The Iridium-Cosmos event illustrates the two-fold effect of collisions: the damage or destruction of an operational satellite (i.e., an expensive or critical asset) and the creation of additional debris. Due to the dynamics of a satellite collision (or rocket body explosion) and orbital perturbations, the resulting cloud of debris does not stay contained in the orbital planes of the parent objects [20]. Instead, over the course of a year, the debris cloud from a single event can easily evolve into a shell around the Earth, spanning all orbital planes around the original altitude.

Unlike active satellites that have attitude control and therefore predictable orientations [30], space debris is uncontrolled and likely to be tumbling. The tumbling rate of a space object can be ascertained from "light curves," whereby temporal fluctuations in the observed brightness of an object reveal its tumbling period. Debris objects in LEO have demonstrated tumbling rates as high as ~10s of degrees per second [20]. Another study found that retired GEO satellites had maximum a tumbling rate of 2.5°/s, but that 90% and 40% of them had rates below 1°/s and 0.5°/s, respectively. The tumbling rate of a debris object, particularly in LEO, can be expected to decrease over time, due to the effects of drag and gravity [28]. Knowledge of current and changing tumbling rates is especially critical to active debris removal efforts in which the debris object must be physically secured [37].

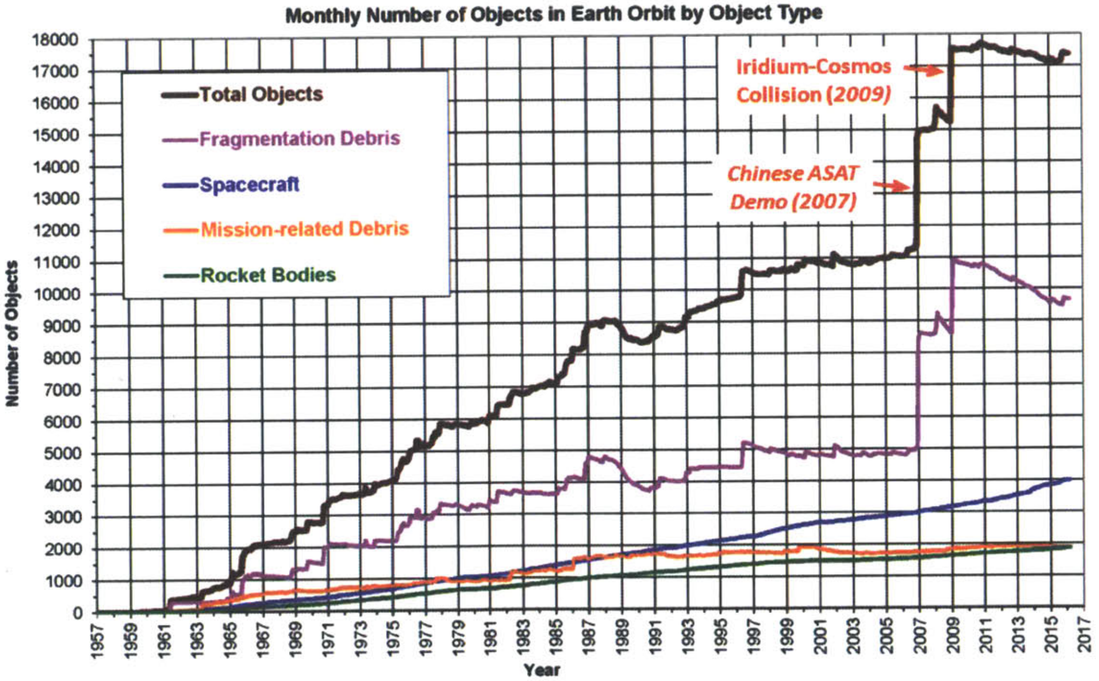

Figure 2: History of catalogued space objects. Graphic courtesy of the NASA Orbital Debris Program Office [38]

Concerns about space debris began to arise several decades ago, when there were only a few thousand known pieces of space debris [4]. Today, as illustrated in Figure 2, the number of objects (~10 cm or larger) in LEO and geostationary orbit (GEO) has grown to over 17,000 objects, as catalogued by the Joint Space Operations Center (JSpOC) within the United States Strategic Command (USSTRATCOM) [38]. Disturbingly, this total does not include the estimated hundreds of thousands objects in the <5 cm size range that are currently undetectable and not catalogued. The decade-by-decade growth of objects in LEO is further illustrated in Figure 3. Operational satellites constitute only about 5% of all catalogued objects in space, while the remaining 95% represents debris (i.e., 8% are spent rocket stages and 87% are satellite fragments) [8].

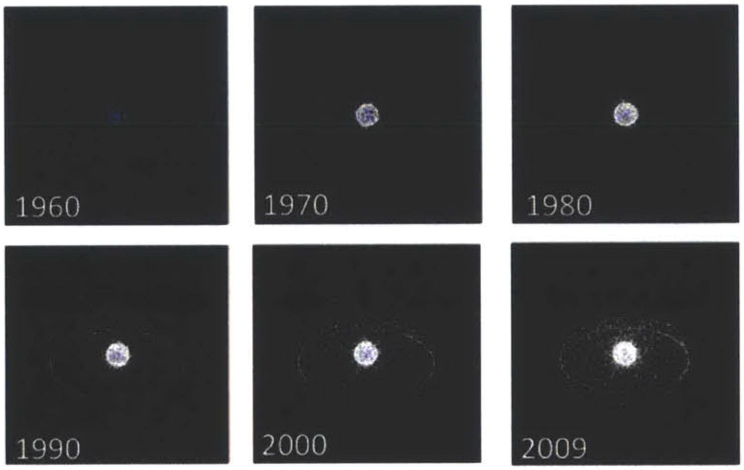

Figure 3: Evolution of LEO object population. Graphic courtesy of NASA [6]

The Inter-Agency Space Debris Coordination Committee (IADC) and several studies have concluded that the space debris population in LEO has already reached a state of instability (the so called Kessler syndrome [4]), even if nations and organization strictly adhere to mitigation guidelines, such as ensuring that spacecraft and rocket bodies only have a 25-year lifetime before de-orbiting [1, 3, 5]. In fact, over the next 200 years, catastrophic collisions (> 40 J/g energy-to-mass ratios) among spacecraft and debris are expected to occur every five to nine years. These types of collisions, such as the Iridium-Cosmos collision in 2009, create a significant amount of additional debris and will continually cause the space debris population to grow organically. The situation is so dire that the IADC now recommends that space agencies seriously consider space debris removal strategies and missions.

Managing the space debris problem requires an accurate understanding of the space debris population. Highlighting the criticality of space surveillance at the time this thesis is written (year 2016), it was recently announced that the United States (US) Department of Defense (DoD) intends to spend $6 billion on Space Situational Awareness (SSA) efforts through the year 2020 [39]. The National Aeronautics and Space Administration's (NASA) [40] and European Space Agency (ESA) [41] have an Orbital Debris Program Office and Space Debris Program Office, respectively, dedicated to understanding and addressing issue of space debris.

1.2. Current Space Debris Characterization Techniques

At the core of all space surveillance efforts is a host of measurement systems. Current techniques for characterizing space debris can be classified into the following three categories: remote sensing, *in situ* measurements, and break-up models and experiments.

1.2.1. Remote Sensors

The vast majority of data on existing debris are collected by passive and active *remote sensing* systems. The most widely used systems are *radars* and passive *optical telescopes*, which not only provide position and velocity information, but also RF, spectral, polarization, and temporal (e.g., periodic intensity fluctuations due to object tumbling) features. For example, in 2002, infrared (IR) spectroscopy revealed that a newly detected space object was likely a Saturn V rocket stage leftover from the Apollo 12 mission, rather than a near-Earth asteroid [42]. The use of optical telescopes to measure passive polarimetric features is discussed in Section 1.3.2.

Shown in Figure 4, the United States (US) Space Surveillance Network (SSN), which is tasked by JSpOC to maintain a running catalog of all detectable (i.e., > 5 cm at the time of writing this thesis) artificial objects in Earth orbit, is composed of over 30 ground-based radars and optical telescopes located around the world [8]. These systems include conventional radars, such as the Haystack Millstone facility at the Massachusetts Institute of Technology Lincoln Laboratory (MIT-LL), and phased array radars, such as those at Cavalier Air Force Base (AFB) in North Dakota and Eglin AFB in Florida. SSN also includes passive telescopes, such as the Advanced Electro-Optical Telescope, a 3.67 m aperture system (the largest in the US) that is part of the Maui Space Surveillance System (MSSS) operated at Mount Haleakala on the island of Maui, and the Space Surveillance Telescope (SST), a 3.5 m aperture system in New Mexico.

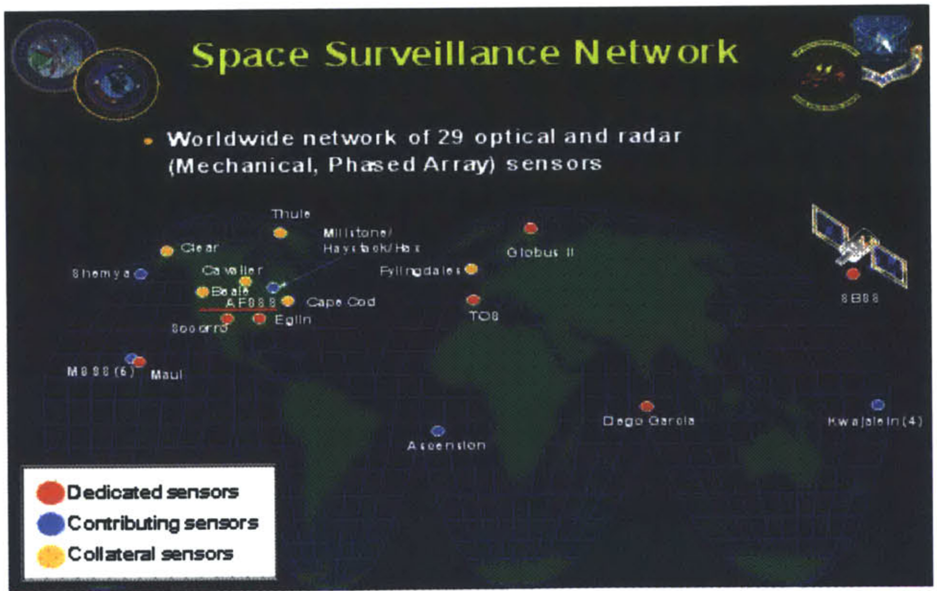

Space Surveillance Network

- Worldwide network of 29 optical and radar (Mechanical, Phased Array) sensors

Figure 4: United States Space Surveillance Network. Illustration courtesy of U.S. Strategic Command [8]

In the last two decades, several groups have also built ground-based *laser radars* for tracking space debris. The goal of these systems is to track debris fragments that are 1 to 10 cm in size with 1 meter accuracy [43]. Such small debris can cause catastrophic damage in a collision, yet cannot be tracked reliably with other techniques because of their small cross sections and orbital instability [43]. The most notable laser radar in operation today is the system at the Mount Stromlo facility located near Canberra, Australia [9, 10]. This system operates at a wavelength of 1064 nm, a pulse width of 5 ns, a pulse repetition frequency (PRF) of 100 Hz, and an average power of 200 W, and can reliably track LEO space objects less than 10 cm in size [9]. The Chinese Space Agency (CSA) operates another laser radar system (532 nm wavelength, 10 ns pulse width, 20 Hz PRF, 40 W average power) at the Shanghai Astronomical Observatory and has successfully detected and tracked orbiting rocket bodies [11]. Other ground-based laser radars used for space surveillance include the Métrologie Optique telescope in France [12] (532 nm, 8 ns, 10 Hz, 20 W) and Satellite Laser Ranging (SLR) Station Graz in Austria [13] (532 nm, 10 ps, 2 kHz, 0.8 W). Space-based laser radars have also been proposed for the detection and monitoring of small debris, but none has been implemented [44, 45]. This thesis contends that in addition to providing an enhanced tracking capability, laser radars could also perform active polarimetry on space objects for enhanced characterization.

1.2.2. In Situ Measurements

In situ measurements constitute another valuable technique for characterizing space debris, particularly fragments (as well as micrometeoroids) that are < 1 cm in size. *In situ* measurements of space debris are performed by placing an apparatus in orbit so that it collides with small debris over some period of time. The apparatus can either be inert or actually contain impact sensors on its surface.

Traditionally, the *in situ* apparatus is inert and must ultimately be retrieved in order to examine its surface for craters resulting from hypervelocity impacts with very small debris [46]. The presence of craters gives an indication of the amount of small debris at the operating altitude. Residual material within the craters can also be tested to determine the chemical composition of the debris. One of the most well known examples of *in situ* measurements via surface examination was the Long Duration Exposure Facility (LDEF), a school-bused sized cylindrical apparatus placed in LEO in 1984 and retrieved in 1990 [47, 48]. Other surfaces examined for debris craters include that of the Space Shuttle and the solar panels of the Hubble Space Telescope (HST) [49].

More sophisticated *in situ* measurements can be performed using an apparatus covered in *impact sensors*. Such an apparatus actually detects and records (and sends to a ground station) the occurrence of hypervelocity impacts, rather than it having to be retrieved and examined manually. As a recent example, in 2015 the Japanese Aerospace Exploration Agency (JAXA) launched an impact sensor called the Space Debris Monitor (SDM), whose surface is composed of closely-spaced, small (100 μm) metallic strips whose conductivities are disrupted, and hence detect impacts with very small debris [50]. Other impact sensor designs also rely on the detection of electrical disturbances triggered by physical collisions [51, 52].

1.2.3. Break-up Models and Experiments

Experiments and simulations have been conducted in coordinated campaigns to understand the phenomenology of satellite breakup and debris evolution. NASA has developed three separate tools for simulating space debris events and environments. These include the Orbital Debris (OD) Engineering Model to predict the debris flux density and collision risk for satellite designers and operators, the OD Evolutionary Model to predict the evolution of the space debris population as a function of future launch rate and other parameters, and the Standard Satellite Breakup Model to the predict the ejection of debris fragments from a satellite collision or explosion and the evolution of the debris cloud [53].

NASA has also conducted several hypervelocity impact (HVI) tests to validate its breakup models. A few HVI tests have been conducted at the Arnold Engineering and Development Center (AEDC) in Tennessee, in which real or mockup satellites are hit with a projectile at impact speeds of 6+ km/s and the resulting debris is collected in a surrounding canister. In the Satellite Orbital Debris Characterization Impact Test (SOCIT) of 1992, a fully functional Navy satellite was destroyed in an HVI test, and most recently in 2014, NASA conducted HVI tests on targets known as DebriSat (a satellite representative of modern payloads) and DebrisLV (a target resembling a launch vehicle upper stage). The results of HVI tests have been used to validate and update NASA's breakup models, in light of changes in modern satellite construction and materials, and discrepancies between the models and observed on-orbit breakups.

Despite the current suite of measurement and characterization capabilities, the space surveillance community continually seeks more efficient and robust techniques for detecting and discriminating space debris [14]. The holy grail of space surveillance is the ability to remotely determine the constituent material and mass of an individual space debris fragment, which are critical for determining its origin and creation mechanism, ballistic coefficient and susceptibility to drag, potential to damage a spacecraft in a collision [2], and the feasibility of debris removal [21]. However, the space surveillance community does not have a technique that can reliably identify the material and mass of a space object, especially in the centimeter and 10 centimeter size range [54]. This thesis investigates a potentially valuable remote sensing technique for space surveillance known as active polarimetry, by which a ground-based laser radar would illuminate a debris object with pulses of controlled polarization states and then measure the polarization state of the reflected light.

1.3. Polarimetry

As illustrated in Figure 5, active polarimetry is one of two possible forms (the other being passive) of the more general practice of *polarimetry*, by which one makes polarization-sensitive measurements of light reflecting off or transmitting through a target or target scene [15, 16]. With *passive* polarimetry, a target is illuminated by an external light source (e.g., the sun) [16, 55], while with *active* polarimetry, a target is illuminated by a laser or other light source with a variable, but controlled, polarization state [56, 57, 58, 59, 60]. As proven mathematically in Chapter 2, only active polarimetry can estimate the complete polarimetric behavior of a target, as described by its *Mueller matrix* and associated polarimetric properties.

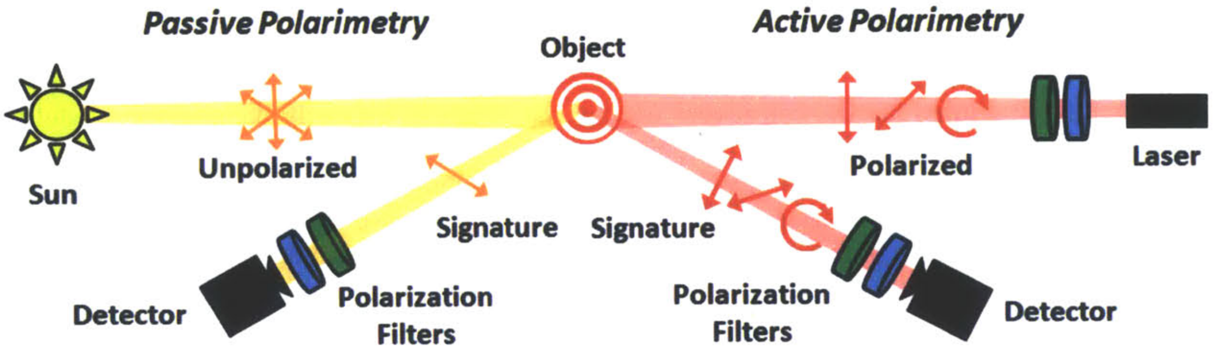

Figure 5: Illustration of passive and active polarimetry. Original graphic created by the author.

1.3.1. Applications of Polarimetry

Polarimetric observations, whether passive or active, can take the form of either *resolved* images (directly or by raster scanning) for the purpose of image contrast enhancement, or *non-resolved* measurements (i.e., the target of interest is contained within a single pixel) for the purpose of target detection or characterization. Polarimetry can also be performed at a variety of wavelengths, including ultraviolet (UV), visible (VIS), near infrared (NIR), long-wave infrared (LWIR), and radio wavelength regimes. Uses of resolved polarimetry (or imaging), whether passive or active, are widespread. Applications of *passive imaging* include medical diagnostics [61], meteorology [62], photography [63], and military surveillance [64], among many others Applications of *active imaging* include agriculture [65], ellipsometry [66], forestry [67], industrial engineering [68], medical diagnostics [69], meteorology [70, 71], and military surveillance [72]. By contrast, applications of non-resolved polarimetry are more limited. The most notable application of *passive non-resolved* polarimetry is astronomy, in which polarization features can reveal information about the surfaces and molecular structure, makeup, and orientation of distant astronomical bodies [73]. Finally, *active non-resolved* polarimetry is often used for long-range target detection in military and civilian aviation applications. Radars employ what is known as polarization diversity, whereby orthogonal polarization states (e.g., horizontal and vertical, or right- and left\-handed circular) are each transmitted and received (i.e., measured with polarization filters) to reject clutter and detect targets of interest based on the observed change or preservation of the incident polarization [74, 75, 76].

1.3.2. Polarimetry for Space Surveillance

Polarimetry has also been used and researched for the characterization of space debris. A critical aspect of polarimetry for space surveillance is that the measurements are likely tumbling and are almost always non-resolved, with the exception of the largest of space debris objects (i.e., rocket bodies and retired satellites).

Passive polarimetry has been performed using optical telescopes that measure the polarization state of sunlight reflecting from space objects. Since sunlight is unpolarized, passive techniques can only help estimate the *polarizance* of an object, or ability to induce polarization onto incident unpolarized light. In practice, optical telescopes (e.g., the Firepond telescope at the Haystack

Millstone facility [8]) make measurements at two orthogonal polarizations to determine the percentage of linear polarization (%POL) of the reflected light i.e., whether it is more linearly polarized or unpolarized [22, 23]. Dielectric materials tend to have higher polarizance than metals, so the measured %POL can reveal whether an object is relatively dielectric or metallic [25, 27]. Temporal variations in passive polarimetric signatures, or polarization "light curves," have also been proposed to help determine the shape and tumbling dynamics of an object [24]. Unfortunately, however, other potentially distinguishing polarimetric properties such as diattenuation, retardance, and depolarization power cannot be determined with any of these passive techniques. Only an active system can probe these additional features.

Active polarimetry at radio wavelengths has been performed for space surveillance using radar systems. Polarimetric radars, such as the Haystack Radio Telescope [77] transmit beams that are right-handed circularly polarized and then measure the left-handed circularly polarized and right-handed circularly polarized parts of the return, i.e., the Principle polarization (PP) and Orthogonal polarization (OP), respectively. Spherical objects only return a PP signal because they behave as mirrors due to their symmetry. By contrast, perfect dipoles (e.g., thin wires) return equal amounts of PP and OP, because their reflected waves are linearly polarized parallel to the dipole axis and so contain equal right- and left-handed circularly polarized components [78]. Consequently, space debris objects that exhibit mostly PP signals are assumed to be spheres or sphere-like [27]. For example, spherical droplets of sodium-potassium alloy (NaK) coolant ejected from Russian nuclear satellites have been remotely identified by polarimetric radars based on these object's high PP signals and orbital characteristics. A notable limitation of active polarimetry using radio waves is that it is insensitive to surface roughness that is smaller than radio wavelengths (centimeters). If such surfaces were actively interrogated at optical wavelengths, then a depolarization effect may be observed and the surface roughness could be inferred [79].

Active polarimetry at optical wavelengths (VIS or IR) has been considered in principle for the purpose of space surveillance, but, to the author's knowledge, has never actually been implemented with a laser radar. There have been several studies to determine whether active polarimetric phenomenology can actually be exploited for space surveillance purposes. Previous studies have performed bench-top experiments to measure polarimetric features of spacecraft materials (i.e., "coupon" samples, as opposed to 3D objects) as functions of geometry. Giakos et al. [14] measured materials over a small range of angles in a quasi-monostatic geometry (i.e., 10° separation between source and detector) at a wavelength of $\lambda = 830$ nm and noted that Teflon®-coated aluminum was more depolarizing than Mylar- or Kapton®-coated aluminum. Giakos et al. [31] and Peterman [32] made quasi-monostatic (i.e., 2.5° separation) measurements (concentrating on the specular peak) at $\lambda = 1065$ nm and discovered differences in the diattenuation, retardance, and depolarization power of amorphous- and poly-silicon solar panels, Mylar, and Kapton®. Reddy [33] made bistatic measurements at $\lambda = 830$ nm and determined that Teflon® is more depolarizing than Kapton® and aluminum. All previous studies conclude that spacecraft materials exhibit distinguishing polarimetric features that may potentially be exploited by active polarimetry at optical wavelengths. However, while these studies made some informative measurements of spacecraft materials, none of them considers the resulting active polarimetric signatures of non-resolved space objects, which are the ultimate measurements and features of interest. Inspired by previous work and the need to understand object signatures, this thesis research more thoroughly investigates the potential value of active polarimetry through a combination of measurements and simulations.

1.4. Research Nexus

Before introducing the specific experiments and simulations performed in this research, it is enlightening to consider how this thesis fits into the broader research landscape. As illustrated by the Venn diagram in Figure 6, this thesis sits at the intersection of space debris characterization and non-resolved active polarimetry. In the diagram, the left circle contains all currently used space surveillance techniques, organized according to Section 1.2, i.e., the techniques fall under the categories of remote sensing (right hemisphere), *in situ* measurements (top-left quadrant), and simulations (bottom-left quadrant). The remote sensing category is further split between passive (i.e., optical telescopes) and active (i.e., radars and laser radars) systems. The right circle in the diagram contains several representative application areas of polarimetry (Section 1.3.1), which are divided into quadrants depending on whether the application entails passive imaging (top-right quadrant), active imaging (bottom-right quadrant), passive non-resolved measurements (top- left quadrant), or active non-resolved measurements (bottom-left quadrant). Inside the overlap between the two circles are references to the most comprehensive or recent reports (Section 1.3.2) regarding the application of non-resolved polarimetry, both passive (top) and active (bottom), to the characterization of space debris. Since this thesis is an investigation of active polarimetry (at optical wavelengths) for space surveillance, it belongs in the bottom half of this intersection, as indicated on the Venn diagram.

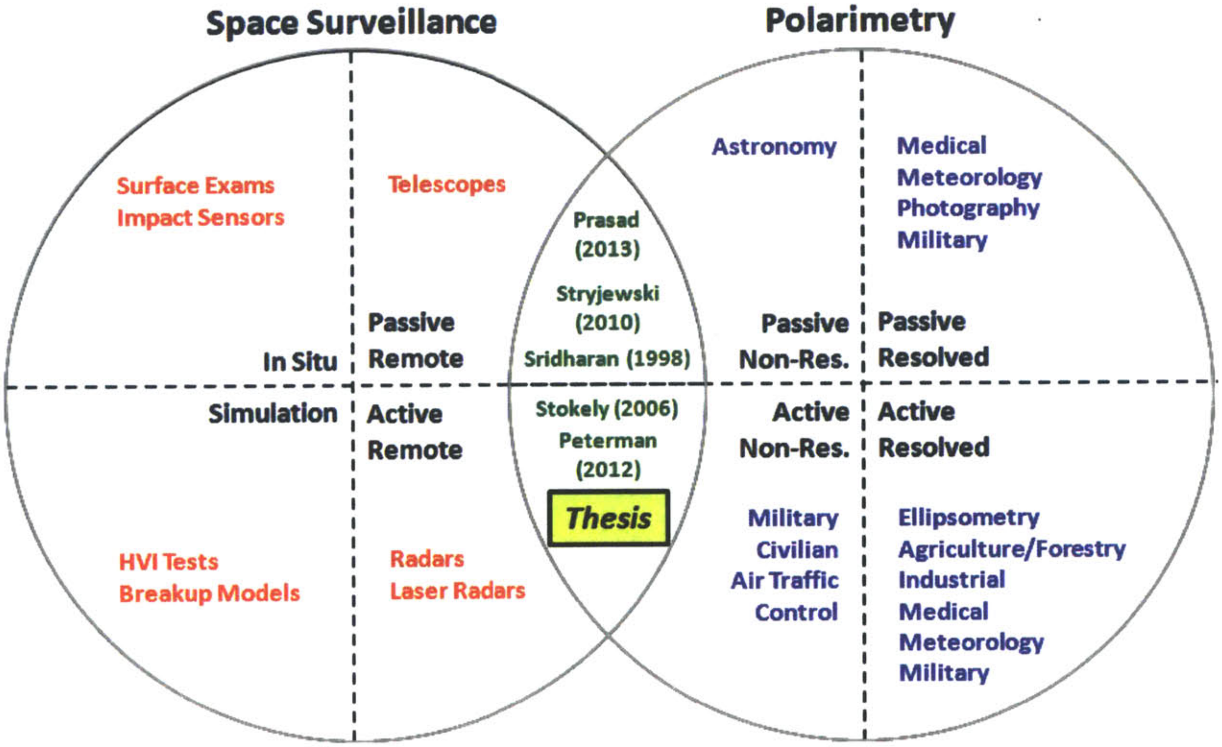

Figure 6: Venn diagram of research nexus. Original graphic created by the author.

1.5. Research Approach

This research takes an experimental and M&S approach, as depicted in Figure 7. The concept of the approach is to experimentally determine the polarimetric behavior of space materials in order to simulate polarimetric signatures of non-resolved objects covered in those materials. In Experiment *A*, measurements are conducted at a wavelength of 1064 nm to determine the polarimetric BRDF (both bistatic and monostatic) of several spacecraft materials, including glossy white paint, matte black paint, aluminum alloy, titanium alloy, black Kapton®, and silver Teflon®. In Experiment *B*, polarimetric images are taken of objects that are covered in spacecraft materials to determine the objects' polarimetric signatures as if they were non-resolved. A simulation is also developed and validated by Experiment *B*, to predict the polarimetric signatures of non-resolved objects, given the (measured) polarimetric BRDFs of their constituent materials. The simulation is used to explore the signatures of non-resolved objects in a variety of engagement scenarios. Thus, this thesis research is novel among previous studies with respect to the range of measured geometries and the attempt to model non-resolved object signatures.

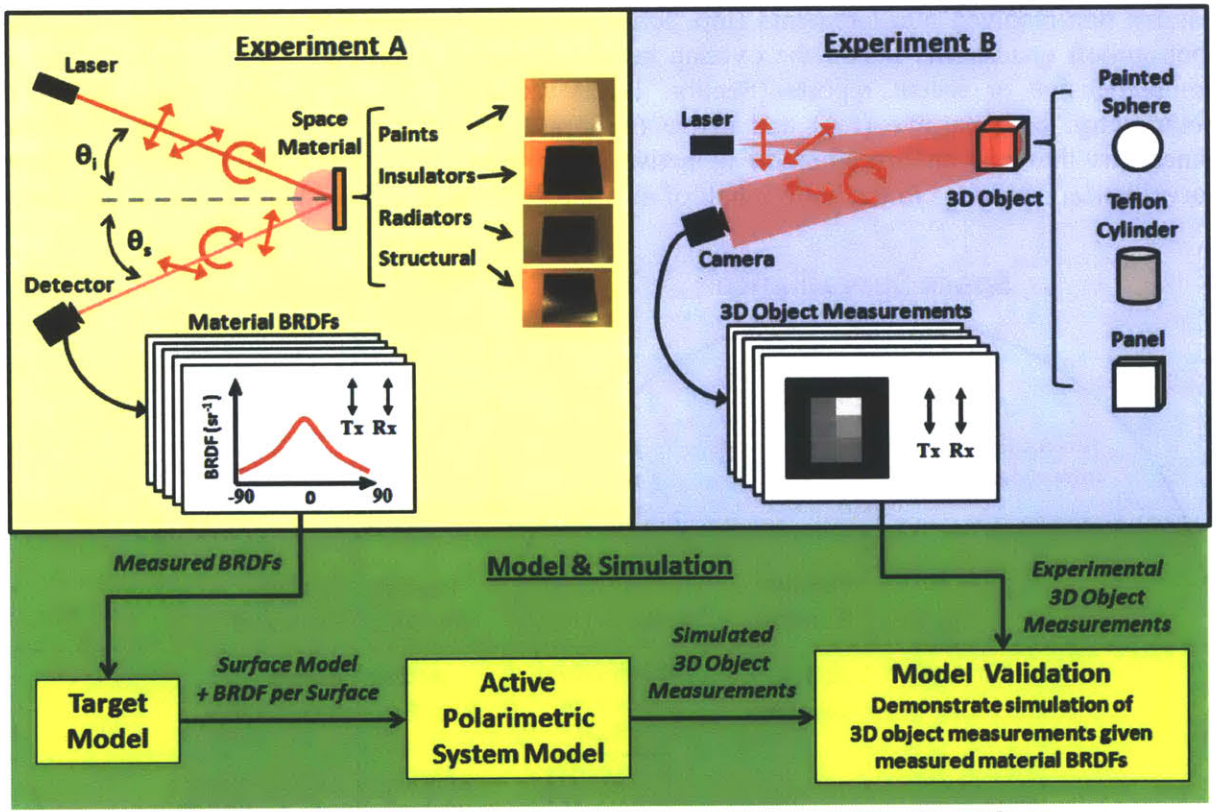

Figure 7: Research approach. Original graphic created by the author.

Referring to Figure 7, Experiment *A* uses a single-pixel detector to measure the polarimetric BRDF of "coupon" samples of several common spacecraft materials. Measurements are taken in both bistatic (in-plane scans for incident angles of θ_i = 15°, 30°, 45°, 60°, and 75°) and monostatic (incident angles from 0° to 90°) geometries. The BRDF of each material is measured as a function of the polarization state of the incident and reflected light, which allows for estimation of the material's Mueller matrix as a function of the incident and viewing angles. The Mueller matrices are decomposed to derive their underlying polarimetric properties. The results reveal notable trends in the materials' geometry-dependent polarimetric properties.

Experiment *B* uses a camera to measure polarimetric images of small objects (e.g., spheres, cylinders, and panels) that are coated or covered in the same spacecraft materials from Experiment *A*. Images are taken as functions of the polarization state of the incident and reflected light. By summing each image, it is possible to estimate the Mueller matrix and polarimetric properties of an object as if it was non-resolved.

Finally, M&S is developed to simulate the monostatic polarimetric signature of a non-resolved object. The simulation uses the measured polarimetric MRDFs (i.e., the monostatic BRDFs) of a database of materials and then geometrically determines the polarimetric signature of a non-resolved object coated or covered with one or more of those materials. To validate the results, the simulation is fed the measured monostatic BRDFs from Experiment *A* and the object shapes from Experiment *B*. The simulated signatures are then compared to the experimental signatures from Experiment *B*. Objects are then simulated for a variety of engagement scenarios, including monostatic measurements of stationary and tumbling objects with different shapes and dimensions, as well as bistatic measurements of objects with strong specular reflections.

The goal of the experiments and simulations are twofold. The first objective is to gain a better understanding of the phenomenology of non-resolved active polarimetry. The second objective is to assess whether the phenomenology can be exploited to identify or classify a non-resolved object's constituent material, shape, or orientation. Both objectives are met and this thesis presents the results and conclusions of this experimental and M&S approach.

1.6. Organization

The remainder of this thesis is organized as follows. Chapter 2 provides the technical background underlying the experimental and theoretical efforts in this research, including the mathematical framework used in all subsequent analysis. Chapter 3 presents the results of Experiment *A*, which measures the polarimetric MRDFs of several representative spacecraft materials and subsequently estimates their geometry-dependent Mueller matrices and polarimetric properties. Chapter 4 presents the results of Experiment *B*, which measures the polarimetric images of several test objects that are covered in spacecraft materials and subsequently estimates their polarimetric signatures as if they were non-resolved. Chapter 5 describes the results of simulating the polarimetric signatures of non-resolved objects of various material types, shapes, dimensions, orientations, and tumbling behaviors. Chapter 6 discusses the exploitability of non-resolved active polarimetry for characterizing objects and the implications for space surveillance. Finally, Chapter 7 concludes with a summary of all significant research contribution and avenues for future work towards the development of a polarimetric laser radar for space surveillance.

This page has been intentionally left blank.

2. Background

This chapter provides the technical background underlying the experimental and theoretical efforts of this research. Topics include Stokes vectors, Mueller matrices, matrix estimation and decomposition, polarimetric properties, error analysis, and the polarimetric BRDF. The discussion here presents the physical and mathematical framework used throughout the remainder of this thesis.

2.1. Stokes Vectors

The *polarization* state of light describes the orientation of its oscillating electrical field and can be conveniently represented by a 4 × 1 *Stokes vector* $\vec{S}$ as follows [80]:

Eq. 1

$$\vec{S} = \begin{bmatrix} s_0 \\ s_1 \\ s_2 \\ s_3 \end{bmatrix} = \begin{bmatrix} I_{total} \\ I_H - I_V \\ I_{+45} - I_{-45} \\ I_{RC} - I_{LC} \end{bmatrix}$$

where $s_0 = I_{total}$ is the total intensity of the light, $s_1 = I_H - I_V$ is the intensity of all horizontally polarized components minus that of all vertically polarized component, $s_2 = I_{+45} - I_{-45}$ is the intensity of all +45° linearly polarized components minus that of all -45° linearly polarized components, and $s_3 = I_{RC} - I_{LC}$ is the intensity of all right-handed circularly polarized components minus that of all left-handed circularly polarized components. By this definition, the Stokes vectors $\vec{S}^H$, $\vec{S}^V$, $\vec{S}^{+45}$, $\vec{S}^{-45}$, $\vec{S}^{RC}$, $\vec{S}^{LC}$, and $\vec{S}^U$ for horizontally (H) polarized, vertically (V) polarized, +45° linearly polarized, -45° linearly polarized, right-handed circularly (RC) polarized, left-handed circularly (LC) polarized, and perfectly unpolarized (U) light, respectively, are:

Eq. 2

$$\vec{S}^H = \begin{bmatrix} 1 \\ +1 \\ 0 \\ 0 \end{bmatrix} \quad \vec{S}^{+45} = \begin{bmatrix} 1 \\ 0 \\ +1 \\ 0 \end{bmatrix} \quad \vec{S}^{RC} = \begin{bmatrix} 1 \\ 0 \\ 0 \\ +1 \end{bmatrix}$$

$$\vec{S}^U = \begin{bmatrix} 1 \\ 0 \\ 0 \\ 0 \end{bmatrix}$$

$$\vec{S}^V = \begin{bmatrix} 1 \\ -1 \\ 0 \\ 0 \end{bmatrix} \quad \vec{S}^{-45} = \begin{bmatrix} 1 \\ 0 \\ -1 \\ 0 \end{bmatrix} \quad \vec{S}^{LC} = \begin{bmatrix} 1 \\ 0 \\ 0 \\ -1 \end{bmatrix}$$

2.2. Mueller Matrices

A material's effect on the polarization state of incident light can be quantified by a 4 × 4 real matrix called the *Mueller matrix* M [80]:

Eq. 3

$$M = \begin{bmatrix} m_{00} & m_{01} & m_{02} & m_{03} \\ m_{10} & m_{11} & m_{12} & m_{13} \\ m_{20} & m_{21} & m_{22} & m_{23} \\ m_{30} & m_{31} & m_{32} & m_{33} \end{bmatrix}$$

As useful examples, the Mueller matrices M_{LPH}, M_{HWPH}, M_{HWP45}, $M_{HWP22.5}$, M_{HWP-45} of a horizontally-oriented linear polarizer (LPH), half-wave plate with horizontally-oriented fast axis (HWPH), half-wave plate with +45°-oriented fast axis (HWP45), half-wave plate with +22.5°-oriented fast axis (HWP22.5), and quarter-wave plate with -45°-oriented fast axis (HWP-45), respectively, are

$$M_{LPH} = \frac{1}{2}\begin{bmatrix} 1 & 1 & 0 & 0 \\ 1 & 1 & 0 & 0 \\ 0 & 0 & 0 & 0 \\ 0 & 0 & 0 & 0 \end{bmatrix} \qquad M_{HWP22.5} = \begin{bmatrix} 1 & 0 & 0 & 0 \\ 0 & 0 & 1 & 0 \\ 0 & 1 & 0 & 0 \\ 0 & 0 & 0 & -1 \end{bmatrix}$$

Eq. 4

$$M_{HWPH} = \begin{bmatrix} 1 & 0 & 0 & 0 \\ 0 & 1 & 0 & 0 \\ 0 & 0 & -1 & 0 \\ 0 & 0 & 0 & -1 \end{bmatrix} \qquad M_{QWP-45} = \begin{bmatrix} 1 & 0 & 0 & 0 \\ 0 & 0 & 0 & 1 \\ 0 & 0 & 1 & 0 \\ 0 & -1 & 0 & 0 \end{bmatrix}$$

$$M_{HWP45} = \begin{bmatrix} 1 & 0 & 0 & 0 \\ 0 & -1 & 0 & 0 \\ 0 & 0 & 1 & 0 \\ 0 & 0 & 0 & -1 \end{bmatrix}$$

One can multiply the Stokes vector $\vec{S}^{in}$, describing the polarization state of incident light, by a material's Mueller matrix M to calculate the Stokers vector $\vec{S}^{out}$ describing the polarization state of the reflected (or transmitted) light:

Eq. 5

$$M\vec{S}^{in} = \vec{S}^{out}$$

For example, if horizontally polarized light ($\vec{S}^{H}$) enters a half-wave plate (M_{HWP45}) with its fast axis oriented at 45° from the horizontal plane, the output is expected to be vertically polarized. Indeed, plugging $\vec{S}^{in} = \vec{S}^{H}$ and $M = M_{HWP45}$ into Eq. 5 yields the Stokes vector $\vec{S}^{V}$ of vertically polarized light as follows:

Eq. 6
$$M_{HWP45}\vec{S}^H = \begin{bmatrix} 1 & 0 & 0 & 0 \\ 0 & -1 & 0 & 0 \\ 0 & 0 & 1 & 0 \\ 0 & 0 & 0 & -1 \end{bmatrix} \begin{bmatrix} 1 \\ 1 \\ 0 \\ 0 \end{bmatrix} = \begin{bmatrix} 1 \\ -1 \\ 0 \\ 0 \end{bmatrix} = \vec{S}^V$$

The Mueller matrix M can be converted to a *covariance matrix* Σ (not to be confused with the symbol for summation) as follows [81]:

Eq. 7
$$\Sigma = \frac{1}{2}\sum_{i=0}^{4}\sum_{j=0}^{4} m_{ij}\sigma_i \otimes \sigma_j$$

where $\otimes$ denotes the Kronecker product of matrices, and σ_i are the Pauli matrices defined as:

Eq. 8
$$\sigma_1 = \begin{bmatrix} 1 & 0 \\ 0 & 1 \end{bmatrix} \quad \sigma_2 = \begin{bmatrix} 1 & 0 \\ 0 & -1 \end{bmatrix}$$
$$\sigma_3 = \begin{bmatrix} 0 & 1 \\ 1 & 0 \end{bmatrix} \quad \sigma_4 = \begin{bmatrix} 0 & -i \\ i & 0 \end{bmatrix}$$

The covariance matrix Σ can also be expressed as:

Eq. 9
$$\Sigma = V\Lambda V^{-1}$$

where Λ is a 4 x 4 diagonal matrix containing the four eigenvalues λ_i of Σ , and V is the corresponding matrix of unitary column eigenvectors v_i. The covariance matrix of any physically realizable (i.e., valid) Mueller matrix is guaranteed to be a positive semi-definite Hermitian (PSDH) matrix, which means that all four of Σ's eigenvalues are positive or zero. Thus, a condition for an arbitrary 4 × 4 real matrix to be a physically realizable (i.e. valid) Mueller matrix is that the eigenvalues of its associated covariance matrix meet this criterion [81, 82]:

Eq. 10
$$\lambda_i \geq 0 \qquad i = 0, 1, 2, 3$$

2.3. Mueller Matrix Decomposition

A material's Mueller matrix can be decomposed to quantify its underlying polarimetric behavior. Any given material can exhibit a combination of three fundamental polarimetric behaviors [16]. *Diattenuation* is the preferential reflection (or transmittance) of certain polarization states over others. *Retardance* is the introduction of a phase shift between certain polarization states, by retarding one of their phases relative to the other. *Depolarization* is the conversion of polarized light into partially polarized or unpolarized light. Lu and Chipman [83] describe the mathematics for decomposing a Mueller matrix into the product of three matrices corresponding to these fundamental behaviors:

Eq. 11
$$M = M_{\Delta}M_R M_D$$

where M_D, M_R, and M_Δ are the 4 x 4 diattenuation, retardance, and depolarization factors, respectively. The general form of each matrix in Eq. 11 is

Eq. 12

$$M = \frac{1}{m_{00}} \begin{bmatrix} 1 & \vec{D}^T \\ \vec{P} & m \end{bmatrix}$$

Eq. 13

$$M_D = T_u \begin{bmatrix} 1 & \vec{D}^T \\ \vec{D} & m_D \end{bmatrix}$$

Eq. 14

$$M_R = \begin{bmatrix} 1 & \vec{0}^T \\ \vec{0} & m_R \end{bmatrix}$$

Eq. 15

$$M_\Delta = \begin{bmatrix} 1 & \vec{0}^T \\ \vec{P}_\Delta & m_\Delta \end{bmatrix}$$

where $T_u = m_{00}^{-1}$ is the reflectivity (or transmittivity) for unpolarized light, $\vec{D}$ is the diattenuation vector, $\vec{P}$ and $\vec{P}_\Delta$ are the polarizance vectors of M and M_Δ, respectively, m, m_D, m_R, and m_Δ are the 3 × 3 sub-matrices of their respective parent matrices, and $\vec{0}$ is a 3 × 1 vector of zeros.

Since matrix multiplication is not commutative, a Mueller matrix could also be decomposed with the factors permutated in five other possible sequences (e.g., $M = M_R M_D M_\Delta$), which can, in some cases, lead to a different interpretation of the material's behavior. In this research, analysis is restricted to the sequence in Eq. 8, since it is readily mathematically obtainable and has clear separation of the depolarizing (M_Δ) and nondepolarizing ($M_R M_D$) contributions [83]. The decomposition reveals an array of polarimetric properties describing the material's polarimetric behavior.

2.4. Polarimetric Properties

This thesis focuses on several polarimetric properties computed directly from the decomposed Mueller matrix. The first property is *diattenuation* (*D*), which is a dimensionless number (range 0 to 1) indicating how strongly the material reflects (or transmits) some incident polarization states relative to others [83]. A perfect diattenuator (e.g., an ideal linear polarizer) has a diattenuation of $D = 1$. Diattenuation is simply the magnitude of the diattenuation vector $\vec{D}$ from Eq. 12:

Eq. 16

$$D = |\vec{D}|$$

The second property considered in this paper is *retardance (*R), which is the relative phase shift, in units of radians or degrees (range 0 to 180°), induced by the material onto its orthogonal eigenpolarizations [83]. A half-wave and quarter-wave plate have retardances of $R = 180°$ and $R = 90°$, respectively. The retardance is related to the trace (tr) of the retardance factor M_R from Eq. 13 as follows:

Eq. 17

$$R = \cos^{-1}\left[\frac{\mathrm{tr}(M_R)}{2} - 1\right]$$

The third property of interest here is depolarization power (Δ), which is a dimensionless number (range 0 to 1) indicating how strongly the material depolarizes incident light [83]. An ideal depolarizer has a depolarization power of $\Delta = 1$. The depolarization power of a material is related to the three eigenvalues λ_i^Δ of the sub-matrix m_Δ inside the depolarization factor M_Δ from Eq. 14 as follows:

Eq. 18

$$\Delta = 1 - \frac{|\lambda_0^\Delta| + |\lambda_1^\Delta| + |\lambda_2^\Delta|}{3}$$

One final property is polarizance (*P*), which is a dimensionless number (range 0 to 1) indicating how strongly the material converts unpolarized light into polarized light. A polarizance value of $P = 1$ corresponds to perfect polarizance (e.g., a material illuminated at its Brewster angle [80]), meaning any reflected (or transmitted light) will be completely polarized. The polarizance of a material is simply the magnitude of the polarizance vector $\vec{P}$ from Eq. 12 as follows:

Eq. 19

$$P = |\vec{P}|$$

Even strong or perfect depolarizers can technically exhibit polarizance via the polarizance $P_\Delta = |\vec{P}_\Delta|$ found in the definition of a depolarizer (Eq. 15), indicating that the material can first depolarize the incident light and then induce polarization upon it [83].

Besides, *D*, *R*, Δ, and *P*, many other polarimetric properties are also obtainable from the elements of the Mueller matrix and its decomposition [56, 57, 83]. For example, the diattenuation (*D*) of a material can be divided into its linear diattenuation (D_L), describing the preferential reflection of linear polarized light, and circular diattenuation (D_C) describing the preferential reflection of circularly polarized light. All properties are potentially exploitable as a means of characterizing and identifying the material or object being measured. The analysis in this research revolves around the properties of diattenuation (*D*), retardance (*R*), depolarization power (Δ), and polarizance (*P*), since they quantify the basic polarimetric behaviors. As proven in Section 2.5, an active polarimetric system would be able to estimate the entire Mueller matrix and, after decomposition, all four of these properties (*D*, *P*, *R*, and *Δ*), while a passive system would only be able to estimate polarizance.

2.5. Mueller Matrix Estimation

Polarimetry makes it possible to partially or completely determine a material or object's Mueller matrix and associated polarimetric properties. Whether polarimetry is done passively or actively, the governing mathematics, as depicted in Figure 8, are the same.

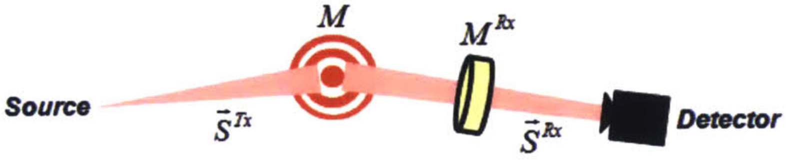

Figure 8: Depiction of active polarimetry with Mueller calculus notation. Original graphic created by the author.

If $\vec{S}^{Tx}$ is the Stokes vector of the light incident upon the material (whether from the sun or a laser), M is the Mueller matrix of the material being measured, and M^{Rx} is the Mueller matrix of the polarization filters placed in front of the detector, then the Stokes vector $\vec{S}^{Rx}$ of the light reaching the detector is given by applying Eq. 5 twice sequentially:

Eq. 20

$$\vec{S}^{Rx} = M^{Rx} M \vec{S}^{Tx}$$

In our notation, $\vec{S}^{Tx}$ is the Stokes vector of Tx-polarized (e.g., H-polarized, or horizontally polarized) light that is "transmitted" (Tx) or sent to the material, while M^{Rx} is a Mueller matrix that "receives" (Rx) or passes the Rx-polarized component of the reflected light. The Mueller matrices M^H, M^V, M^{+45}, and M^{RC} for receiving H, V, +45, and RC polarizations, respectively, can be computed as follows:

Eq. 21

$$M^{H} = M_{LPH} = \frac{1}{2}\begin{bmatrix} 1 & 1 & 0 & 0 \\ 1 & 1 & 0 & 0 \\ 0 & 0 & 0 & 0 \\ 0 & 0 & 0 & 0 \end{bmatrix} \qquad M^{V} = M_{LPH} M_{HWP+45} = \frac{1}{2}\begin{bmatrix} 1 & -1 & 0 & 0 \\ 1 & -1 & 0 & 0 \\ 0 & 0 & 0 & 0 \\ 0 & 0 & 0 & 0 \end{bmatrix}$$

$$M^{+45} = M_{LPH} M_{HWP+22.5} = \frac{1}{2}\begin{bmatrix} 1 & 0 & 1 & 0 \\ 1 & 0 & 1 & 0 \\ 0 & 0 & 0 & 0 \\ 0 & 0 & 0 & 0 \end{bmatrix} \qquad M^{RC} = M_{LPH} M_{QWP-45} = \frac{1}{2}\begin{bmatrix} 1 & 0 & 0 & 1 \\ 1 & 0 & 0 & 1 \\ 0 & 0 & 0 & 0 \\ 0 & 0 & 0 & 0 \end{bmatrix}$$

The Stokes vector $\vec{S}^{Rx}$ of the light that ultimately reaches the detector is actually inconsequential, since according to Eq. 1, the intensity I_{TxRx} measured by the detector is equal to the first element s_0^{Rx} of $\vec{S}^{Rx}$ (i.e., independent of polarization):

Eq. 22

$$I_{TxRx} = s_0^{Rx} = \sum_{i=0}^{3} m_{0i}^{Rx} \sum_{j=0}^{3} s_j^{Tx} m_{ij}$$

where m_{0i}^{Rx} is element i of the first row of M^{Rx}, s_j^{Tx} is element j of $\vec{S}_{Tx}$, and m_{ij} is element (i, j) of M. If the 4×4 matrix M is reshaped to be a 16×1 vector $\vec{M}$, then Eq. 22 can be rewritten as a dot product:

Eq. 23

$$I_{TxRx} = \vec{h}_{TxRx} \vec{M}$$

where the vectors $\vec{M}$ and $\vec{h}_{TxRx}$ are constructed as follows:

Eq. 24

$$\vec{M} = \begin{bmatrix} m_{00} & m_{10} & \dots & m_{33} \end{bmatrix}^T$$

Eq. 25

$$\vec{h}_{TxRx} = \begin{bmatrix} m_{00}^{Rx} s_0^{Tx} & m_{01}^{Rx} s_0^{Tx} & \dots & m_{03}^{Rx} s_3^{Tx} \end{bmatrix}$$

Eq. 19 is the crux of polarimetry. By measuring $I_{Tx^n Rx^n}$ for N different TxRx pairs, one can construct a system of N equations, each in the form of Eq. 23:

Eq. 26

$$\vec{I} = H\vec{M}$$

$$\begin{bmatrix} I_{Tx^1 Rx^1} \\ I_{Tx^2 Rx^2} \\ \dots \\ I_{Tx^N Rx^N} \end{bmatrix} = \begin{bmatrix} \vec{h}_{Tx^1 Rx^1} \\ \vec{h}_{Tx^2 Rx^2} \\ \dots \\ \vec{h}_{Tx^N Rx^N} \end{bmatrix} \begin{bmatrix} m_{00} \\ m_{10} \\ \dots \\ m_{33} \end{bmatrix}$$

where the vectors $\vec{I}$ and matrix H are concatenations of the N measured intensities $I_{Tx^n Rx^n}$ and associated vectors $\vec{h}_{Tx^n Rx^n}$, respectively. Assuming a determined system (N linear independent equations, N unknowns), Eq. 26 can be solved as follows:

Eq. 27

$$\vec{M} = H^{-1}\vec{I}$$

Depending on which elements of H are non-zero, the measured intensities $\vec{I}$ may be linear functions of some or all of the unknown Mueller matrix elements m_{ij}. With passive polarimetry, the sun always (nominally) transmits the same polarization state (Tx), specifically U, or "unpolarized" light, i.e., $\vec{S}^{Tx} = \vec{S}^U = [1\ 0\ 0\ 0]^T$ (Eq. 2). Meanwhile, one can receive different polarization states (Rx) by changing the polarization filters in front of the detector, i.e., the matrix M^{Rx}. Applying Eq. 22, any measured intensities I_{URx} will only be functions of m_{00}, m_{10}, m_{20}, and m_{30}. By making $N = 4$ different Rx measurements, one can construct a system of 4 equations (Eq. 26) to solve for these 4 unknown elements, as long as the equations are linearly independent. Thus, passive polarimetry can (at most) solve for the first column of M (i.e., elements m_{00},, m_{10}, m_{20}, and m_{30}), which provides the material's polarizance vector $\vec{P}$ and polarizance P (Eq. 19).

With active polarimetry, one has individual control over both Tx and Rx, so each measured intensity I_{TxRx} is generally a function of all 16 elements of M. Thus, by making $N = 16$ linearly independent TxRx measurements, active polarimetry can solve for the entire Mueller matrix and, after decomposition, all its polarimetric properties, including diattenuation (D), retardance (R), depolarization power (Δ), and polarizance (P). If more than 16 measurements are made, the over-determined systems of equations can be solved with a least-squares estimator [84]. There are infinitely many sets of 16 linearly independent measurements that would be sufficient for solving for the Mueller matrix. One such set of measurements, which is used for all the experiments and simulations in this research, is given in Table 1:

Table 1: Intensity measurements for 16 TxRx pairs

		Transmit Polarization (Tx)			
		H	**V**	**+45**	**RC**
Receive Polarization (Rx)	**H**	I_{HH}	I_{VH}	I_{+45H}	I_{RCH}
	V	I_{HV}	I_{VV}	I_{+45V}	I_{RCV}
	+45	I_{H+45}	I_{V+45}	I_{+45+45}	I_{RC+45}
	RC	I_{HRC}	I_{VRC}	I_{+45RC}	I_{RCRC}

Plugging in the corresponding Stokes vectors (Eq. 2) and receiver Mueller matrices (Eq. 21) into Eq. 25 for the set of 16 measurements in Table 1, Eq. 26 for the system of 16 linearly independent equations takes the following form:

Eq. 28

$$\vec{I} = H\vec{M}$$

$$\begin{bmatrix} I_{HH} \\ I_{HV} \\ I_{H+45} \\ I_{HRC} \\ I_{VH} \\ I_{VV} \\ I_{V+45} \\ I_{VRC} \\ I_{+45H} \\ I_{+45V} \\ I_{+45+45} \\ I_{+45RC} \\ I_{RCH} \\ I_{RCV} \\ I_{RC+45} \\ I_{RCRC} \end{bmatrix} = \frac{1}{2} \begin{bmatrix} 1 & 1 & 0 & 0 & 1 & 1 & 0 & 0 & 0 & 0 & 0 & 0 & 0 & 0 & 0 & 0 \\ 1 & -1 & 0 & 0 & 1 & -1 & 0 & 0 & 0 & 0 & 0 & 0 & 0 & 0 & 0 & 0 \\ 1 & 0 & 1 & 0 & 1 & 0 & 1 & 0 & 0 & 0 & 0 & 0 & 0 & 0 & 0 & 0 \\ 1 & 0 & 0 & 1 & 1 & -1 & 0 & 1 & 0 & 0 & 0 & 0 & 0 & 0 & 0 & 0 \\ 1 & 1 & 0 & 0 & -1 & -1 & 0 & 0 & 0 & 0 & 0 & 0 & 0 & 0 & 0 & 0 \\ 1 & -1 & 0 & 0 & -1 & 1 & 0 & 0 & 0 & 0 & 0 & 0 & 0 & 0 & 0 & 0 \\ 1 & 0 & 1 & 0 & -1 & 0 & -1 & 0 & 0 & 0 & 0 & 0 & 0 & 0 & 0 & 0 \\ 1 & 0 & 0 & 1 & -1 & 0 & 0 & 1 & 0 & 0 & 0 & 0 & 0 & 0 & 0 & 0 \\ 1 & 1 & 0 & 0 & 0 & 0 & 0 & 0 & 1 & 1 & 0 & 0 & 0 & 0 & 0 & 0 \\ 1 & -1 & 0 & 0 & 0 & 0 & 0 & 0 & 1 & -1 & 0 & 0 & 0 & 0 & 0 & 0 \\ 1 & 0 & 1 & 0 & 0 & 0 & 0 & 0 & 1 & 0 & 1 & 0 & 0 & 0 & 0 & 0 \\ 1 & 0 & 0 & 1 & 0 & 0 & 0 & 0 & 1 & 0 & 0 & 1 & 0 & 0 & 0 & 0 \\ 1 & 1 & 0 & 0 & 0 & 0 & 0 & 0 & 0 & 0 & 0 & 0 & 1 & 1 & 0 & 0 \\ 1 & -1 & 0 & 0 & 0 & 0 & 0 & 0 & 0 & 0 & 0 & 0 & 1 & -1 & 0 & 0 \\ 1 & 0 & 1 & 0 & 0 & 0 & 0 & 0 & 0 & 0 & 0 & 0 & 1 & 0 & 1 & 0 \\ 1 & 0 & 0 & 1 & 0 & 0 & 0 & 0 & 0 & 0 & 0 & 0 & 1 & 0 & 0 & 1 \end{bmatrix} \cdot \begin{bmatrix} m_{00} \\ m_{10} \\ m_{20} \\ m_{30} \\ m_{01} \\ m_{11} \\ m_{21} \\ m_{31} \\ m_{02} \\ m_{12} \\ m_{22} \\ m_{32} \\ m_{03} \\ m_{13} \\ m_{23} \\ m_{33} \end{bmatrix}$$

Given Eq. 28, the 16 unknowns (m_{ij}) can be solved for as follows:

Eq. 29

$$\vec{M} = H^{-1}\vec{I}$$

$$\begin{bmatrix} m_{00} \\ m_{10} \\ m_{20} \\ m_{30} \\ m_{01} \\ m_{11} \\ m_{21} \\ m_{31} \\ m_{02} \\ m_{12} \\ m_{22} \\ m_{32} \\ m_{03} \\ m_{13} \\ m_{23} \\ m_{33} \end{bmatrix} = \begin{bmatrix} 0.5 & 0.5 & 0 & 0 & 0.5 & 0.5 & 0 & 0 & 0 & 0 & 0 & 0 & 0 & 0 & 0 & 0 \\ 0.5 & -0.5 & 0 & 0 & 0.5 & -0.5 & 0 & 0 & 0 & 0 & 0 & 0 & 0 & 0 & 0 & 0 \\ -0.5 & -0.5 & 1 & 0 & -0.5 & -0.5 & 1 & 0 & 0 & 0 & 0 & 0 & 0 & 0 & 0 & 0 \\ -0.5 & -0.5 & 0 & 1 & -0.5 & -0.5 & 0 & 1 & 0 & 0 & 0 & 0 & 0 & 0 & 0 & 0 \\ 0.5 & 0.5 & 0 & 0 & -0.5 & -0.5 & 0 & 0 & 0 & 0 & 0 & 0 & 0 & 0 & 0 & 0 \\ 0.5 & -0.5 & 0 & 0 & -0.5 & 0.5 & 0 & 0 & 0 & 0 & 0 & 0 & 0 & 0 & 0 & 0 \\ -0.5 & -0.5 & 1 & 0 & 0.5 & 0.5 & -1 & 0 & 0 & 0 & 0 & 0 & 0 & 0 & 0 & 0 \\ -0.5 & -0.5 & 0 & 1 & 0.5 & 0.5 & 0 & -1 & 0 & 0 & 0 & 0 & 0 & 0 & 0 & 0 \\ -0.5 & -0.5 & 0 & 0 & -0.5 & -0.5 & 0 & 0 & 0 & 0 & 0 & 0 & 0 & 0 & 0 & 0 \\ -0.5 & 0.5 & 0 & 0 & -0.5 & 0.5 & 0 & 0 & 1 & 1 & 0 & 0 & 0 & 0 & 0 & 0 \\ 0.5 & 0.5 & -1 & 0 & 0.5 & 0.5 & -1 & 0 & 1 & -1 & 2 & 0 & 0 & 0 & 0 & 0 \\ 0.5 & 0.5 & 0 & -1 & 0.5 & 0.5 & 0 & -1 & -1 & -1 & 0 & 2 & 0 & 0 & 0 & 0 \\ -0.5 & -0.5 & 0 & 0 & -0.5 & -0.5 & 0 & 0 & -1 & -1 & 0 & 0 & 1 & 1 & 0 & 0 \\ -0.5 & 0.5 & 0 & 0 & -0.5 & 0.5 & 0 & 0 & 0 & 0 & 0 & 0 & 1 & -1 & 0 & 0 \\ 0.5 & 0.5 & -1 & 0 & 0.5 & 0.5 & -1 & 0 & 0 & 0 & 0 & 0 & -1 & -1 & 2 & 0 \\ 0.5 & 0.5 & 0 & -1 & 0.5 & 0.5 & 0 & -1 & 0 & 0 & 0 & 0 & -1 & -1 & 0 & 2 \end{bmatrix} \cdot \begin{bmatrix} I_{HH} \\ I_{HV} \\ I_{H+45} \\ I_{HRC} \\ I_{VH} \\ I_{VV} \\ I_{V+45} \\ I_{VRC} \\ I_{+45H} \\ I_{+45V} \\ I_{+45+45} \\ I_{+45RC} \\ I_{RCH} \\ I_{RCV} \\ I_{RC+45} \\ I_{RCRC} \end{bmatrix}$$

In every experiment (or simulation) in this research, intensity measurements (I_{TxRx}) are taken (or simulated) for all 16 TxRx pairs in Table 1, so that the Mueller matrix ($\vec{M}$, in vector form) can be solved for using Eq. 29.

2.6. Treatment of Experimental Mueller Matrices

In practice, experimentally determined Mueller matrices will have errors that affect their processing and interpretation.

2.6.1. Physical Realizability

An experimental Mueller matrix is unlikely to be physically realizable (according to Eq. 7), which means its decomposition will yield nonsensical results. Cloude [81] provides a method for *filtering* an experimental Mueller matrix that does not satisfy Eq. 7 due to having a covariance matrix Σ (Eq. 4) with negative eigenvalues. Specifically, one can change all the negative eigenvalues to zero, calculate the new covariance matrix using Eq. 6, and calculate the associated Mueller matrix using the inverse of Eq. 4. The "filtered" Mueller matrix is now, in some sense, the closest physically realizable Mueller matrix to the original noisy one, and can be legitimately decomposed as desired. The eigenvalue ratio γ of the largest (in magnitude) negative eigenvalue (of the original Σ) to the largest positive one can be calculated in decibels as follows:

Eq. 30
$$\gamma = 10 \cdot \log_{10}\left(\frac{|\,\text{max negative}\,\lambda\,|}{\text{max positive}\,\lambda}\right)$$

The ratio γ is a measure of how close the original experimental Mueller matrix was to being physically realizable. Negative values of γ are expected, indicating that the negative eigenvalues are smaller (in magnitude) than the positive ones. Values of $\gamma < -10$ dB generally indicate experimental Mueller matrices that are very close to being physically realizable [81, 85].

2.6.2. *Error Bounds*

The errors of experimental Mueller matrices are derived from errors on the measured intensities used to estimate them. Consequently, the error bounds on an experimental Mueller matrix can be computed as follows. Let $f(X_1, X_2, \ldots X_N)$ a function of N uncorrelated random variables X_n (i = 1 to N). If each X_n has variance σ_n^2, then the variance σ_f^2 of f is equal to the sum of the individual variances, each weighted by the square of the partial derivative with respect to X_n, as follows [86]:

Eq. 31
$$\sigma_f^2 = \sum_{n=1}^{N}\left(\frac{\partial f}{\partial X_n}\right)^2 \sigma_i^2$$

A relevant case is when f is a simple weighted sum:

Eq. 32
$$f(X_1, X_2, \ldots X_N) = \sum_{n=1}^{N} w_n X_n$$

where w_n is a scalar weight on each term. Still assuming that the random variables X_n are uncorrelated, the variance σ_f^2 of f follows from Eq. 31:

Eq. 33
$$\sigma_f^2 = \sum_{n=1}^{N} w_n^2 \sigma_n^2$$

Another relevant case is when $f(X_1, X_2)$ is a function of only two random variables, X_1 and X_2, that are also correlated with covariance σ_{12}^2. In this case, Eq. 31 for the uncorrelated case must be modified as follows:

Eq. 34
$$\sigma_f^2 = \left(\frac{\partial f}{\partial X_1}\right)^2 \sigma_1^2 + \left(\frac{\partial f}{\partial X_2}\right)^2 \sigma_2^2 + 2\left(\frac{\partial f}{\partial X_2}\right)\left(\frac{\partial f}{\partial X_1}\right)\sigma_{12}^2$$

These formulas can be applied to active polarimetry to determine the error bounds on an experimental Mueller matrix. According to Eq. 29, each Mueller matrix element m_{ij} is a linearly weighted sum of a subset of the measured intensities I_{TxRx}, where the weights are the elements of the matrix H^1. Let $\vec{\sigma}_m^2$ be the 16 ×1 vector of the variances σ_{mij}^2 of the 16 Mueller matrix elements. Let $\vec{\sigma}_{TxRx}^2$ be the 16 × 1 vector of the variances σ_{TxRx}^2 of the 16 intensity measurements, each taken at polarization pair TxRx. Applying Eq. 33, $\vec{\sigma}_m^2$ is related to $\vec{\sigma}_{TxRx}^2$ as follows:

Eq. 35

$$\vec{\sigma}_m^2 = K\vec{\sigma}_{TxRx}^2$$

$$\begin{bmatrix} \sigma_{m00}^2 \\ \sigma_{m10}^2 \\ \sigma_{m20}^2 \\ \sigma_{m30}^2 \\ \sigma_{m01}^2 \\ \sigma_{m11}^2 \\ \sigma_{m21}^2 \\ \sigma_{m31}^2 \\ \sigma_{m02}^2 \\ \sigma_{m12}^2 \\ \sigma_{m22}^2 \\ \sigma_{m32}^2 \\ \sigma_{m03}^2 \\ \sigma_{m13}^2 \\ \sigma_{m23}^2 \\ \sigma_{m33}^2 \end{bmatrix} = \begin{bmatrix} 0.25 & 0.25 & 0 & 0 & 0.25 & 0.25 & 0 & 0 & 0 & 0 & 0 & 0 & 0 & 0 & 0 & 0 \\ 0.25 & 0.25 & 0 & 0 & 0.25 & 0.25 & 0 & 0 & 0 & 0 & 0 & 0 & 0 & 0 & 0 & 0 \\ 0.25 & 0.25 & 1 & 0 & 0.25 & 0.25 & 1 & 0 & 0 & 0 & 0 & 0 & 0 & 0 & 0 & 0 \\ 0.25 & 0.25 & 0 & 1 & 0.25 & 0.25 & 0 & 1 & 0 & 0 & 0 & 0 & 0 & 0 & 0 & 0 \\ 0.25 & 0.25 & 0 & 0 & 0.25 & 0.25 & 0 & 0 & 0 & 0 & 0 & 0 & 0 & 0 & 0 & 0 \\ 0.25 & 0.25 & 0 & 0 & 0.25 & 0.25 & 0 & 0 & 0 & 0 & 0 & 0 & 0 & 0 & 0 & 0 \\ 0.25 & 0.25 & 1 & 0 & 0.25 & 0.25 & 1 & 0 & 0 & 0 & 0 & 0 & 0 & 0 & 0 & 0 \\ 0.25 & 0.25 & 0 & 1 & 0.25 & 0.25 & 0 & 1 & 0 & 0 & 0 & 0 & 0 & 0 & 0 & 0 \\ 0.25 & 0.25 & 0 & 0 & 0.25 & 0.25 & 0 & 0 & 0 & 0 & 0 & 0 & 0 & 0 & 0 & 0 \\ 0.25 & 0.25 & 0 & 0 & 0.25 & 0.25 & 0 & 0 & 1 & 1 & 0 & 0 & 0 & 0 & 0 & 0 \\ 0.25 & 0.25 & 1 & 0 & 0.25 & 0.25 & 1 & 0 & 1 & 1 & 4 & 0 & 0 & 0 & 0 & 0 \\ 0.5 & 0.25 & 0 & 1 & 0.25 & 0.25 & 0 & 1 & 1 & 1 & 0 & 4 & 0 & 0 & 0 & 0 \\ 0.25 & 0.25 & 0 & 0 & 0.25 & 0.25 & 0 & 0 & 1 & 1 & 0 & 0 & 1 & 1 & 0 & 0 \\ 0.25 & 0.25 & 0 & 0 & 0.25 & 0.25 & 0 & 0 & 0 & 0 & 0 & 0 & 1 & 1 & 0 & 0 \\ 0.25 & 0.25 & 1 & 0 & 0.25 & 0.25 & 1 & 0 & 0 & 0 & 0 & 0 & 1 & 1 & 4 & 0 \\ 0.25 & 0.25 & 0 & 1 & 0.25 & 0.25 & 0 & 1 & 0 & 0 & 0 & 0 & 1 & 1 & 0 & 4 \end{bmatrix} \cdot \begin{bmatrix} \sigma_{HH}^2 \\ \sigma_{HV}^2 \\ \sigma_{H+45}^2 \\ \sigma_{HRC}^2 \\ \sigma_{VH}^2 \\ \sigma_{VV}^2 \\ \sigma_{V+45}^2 \\ \sigma_{VRC}^2 \\ \sigma_{+45H}^2 \\ \sigma_{+45V}^2 \\ \sigma_{+45+45}^2 \\ \sigma_{+45RC}^2 \\ \sigma_{RCH}^2 \\ \sigma_{RCV}^2 \\ \sigma_{RC+45}^2 \\ \sigma_{RCRC}^2 \end{bmatrix}$$

where the matrix K was found by squaring the elements of the matrix H^1 (Eq. 29), which appropriately weights the variances σ_{TxRx}^2 according to Eq. 33.

Now consider the common practice of normalizing the Mueller matrix by its top-left element m_{00}. The normalized Mueller matrix $\hat{M}$ is written as:

Eq. 36

$$\hat{M} = \frac{1}{m_{00}} M = \frac{1}{m_{00}} \begin{bmatrix} m_{00} & m_{01} & m_{02} & m_{03} \\ m_{10} & m_{11} & m_{12} & m_{13} \\ m_{20} & m_{21} & m_{22} & m_{23} \\ m_{30} & m_{31} & m_{32} & m_{33} \end{bmatrix} = \begin{bmatrix} 1 & m_{01}/m_{00} & m_{02}/m_{00} & m_{03}/m_{00} \\ m_{10}/m_{00} & m_{11}/m_{00} & m_{12}/m_{00} & m_{13}/m_{00} \\ m_{20}/m_{00} & m_{21}.m_{00}. & m_{22}/m_{00} & m_{23}/m_{00} \\ m_{30}.m_{00} & m_{31}/m_{00} & m_{32}/m_{00} & m_{33}/m_{00} \end{bmatrix}$$

Eq. 36 shows that the elements of the normalized matrix $\hat{M}$ are each $\hat{m}_{ij} = m_{ij}/m_{00}$, i.e., a function of two random variables m_{ij} and m_{00}. The variance $\sigma_{\hat{m}ij}^2$ of each element $\hat{m}_{ij}$ can be found by applying Eq. 34:

Eq. 37
$$\sigma^2_{\hat{m}ij} = \left(\frac{m_{ij}}{m_{00}^2}\right)^2 \sigma^2_{m00} + \left(\frac{1}{m_{00}}\right)^2 \sigma^2_{mij} - 2\left(\frac{m_{ij}}{m_{00}^3}\right)\sigma^2_{mij,m00}$$

The variances σ^2_{mij} are given by Eq. 35, but the covariances $\sigma^2_{mij,m00}$ have yet to be computed. The covariance of two scalar random variables *X* and *Y* is given by:

Eq. 38
$$\sigma^2_{XY} = E[XY] - E[X]E[Y]$$

Let $\vec{\sigma}^2_{m,m00}$ be the 16 x1 vector of the covariances $\sigma^2_{mij,m00}$. Plugging Eq. 29 in Eq. 38, it can be shown that $\vec{\sigma}^2_{m,m00}$ is related to $\vec{\sigma}^2_{TxRx}$ as follows:

Eq. 39

$$\vec{\sigma}^2_{m,m00} = K_{\text{cov}}\vec{\sigma}^2_{TxRx}$$

$$\begin{bmatrix} \sigma^2_{m00,m00} \\ \sigma^2_{m10,m00} \\ \sigma^2_{m20,m00} \\ \sigma^2_{m30,m00} \\ \sigma^2_{m01,m00} \\ \sigma^2_{m11,m00} \\ \sigma^2_{m21,m00} \\ \sigma^2_{m31,m00} \\ \sigma^2_{m02,m00} \\ \sigma^2_{m12,m00} \\ \sigma^2_{m22,m00} \\ \sigma^2_{m32,m00} \\ \sigma^2_{m03,m00} \\ \sigma^2_{m13,m00} \\ \sigma^2_{m23,m00} \\ \sigma^2_{m33,m00} \end{bmatrix} = 0.25 \begin{bmatrix} 1 & 1 & 1 & 1 \\ 1 & -1 & 1 & -1 \\ -1 & -1 & -1 & -1 \\ -1 & -1 & -1 & -1 \\ 1 & 1 & -1 & -1 \\ 1 & -1 & -1 & 1 \\ -1 & -1 & 1 & 1 \\ -1 & -1 & 1 & 1 \\ -1 & -1 & -1 & -1 \\ -1 & 1 & -1 & 1 \\ 1 & 1 & 1 & 1 \\ 1 & 1 & 1 & 1 \\ -1 & -1 & -1 & -1 \\ -1 & 1 & -1 & 1 \\ 1 & 1 & 1 & 1 \\ 1 & 1 & 1 & 1 \end{bmatrix} \cdot \begin{bmatrix} \sigma^2_{HH} \\ \sigma^2_{HV} \\ \sigma^2_{H+45} \\ \sigma^2_{HRC} \\ \sigma^2_{VH} \\ \sigma^2_{VV} \\ \sigma^2_{V+45} \\ \sigma^2_{VRC} \\ \sigma^2_{+45H} \\ \sigma^2_{+45V} \\ \sigma^2_{+45+45} \\ \sigma^2_{+45RC} \\ \sigma^2_{RCH} \\ \sigma^2_{RCV} \\ \sigma^2_{RC+45} \\ \sigma^2_{RCRC} \end{bmatrix}$$

where the matrix K_{cov} was found by multiplying (element by element) each row of the matrix *K* (Eq. 35) by the first row of *K*.

Next, one must determine the error bounds on the Mueller matrix's polarimetric properties. Unfortunately, a closed-form expression for the error bounds on, say, diattenuation (*D*) is not easily propagated through the complex process of decomposition [83]. It is also intractable to determine the effect of Cloude's filtering method on downstream error propagation. In light of these difficulties, Hayes [87] ran Monte Carlo simulations to empirically determine the error bounds on estimated polarimetric properties as a function of the error bounds on the estimated Mueller matrix elements. Hayes determined that if the elements of a normalized Mueller matrix have standard deviation $\sigma_{\hat{m}ij} = \sigma$, then the standard deviations σ_D, σ_R, and σ_Δ of diattenuation (D), retardance (R), and depolarization power (Δ), respectively are:

Eq. 40
$$\begin{aligned}\sigma_D &= 0.9454\sigma - 0.0024\\ \sigma_R &= 1.5852\sigma - 0.0043\\ \sigma_\Delta &= 1.2573\sigma - 0.0102\end{aligned}$$

where σ_R is in radians. A closed-form or empirical formula for the error bound on polarizance is not found in the literature, but is likely similar to that of diattenuation. In every experiment in this research, Eq. 35 and Eq. 37 are used to determine the error bounds on the experimental Mueller matrices. Eq. 40 is then used to determine the error bounds on their underlying polarimetric properties.

2.7. Polarimetric BRDF

When performing polarimetry on a material or object, the apparent Mueller matrix will depend on the illumination and viewing geometry, as quantified by the *Bidirectional Reflectance Distribution Function* (BRDF) [88, 89]. Nominally, a material's $BRDF(\theta_i,\phi_i,\theta_s,\phi_s)$ or angular reflectance profile, expressed in inverse steradians (sr^{-1}), is a function of the zenith angle θ_i (0 to 90°) and azimuth angle ϕ_i (-180 to 180°) of the incident beam, as well as those of the direction of scatter (θ_s and ϕ_s). More specifically, a material's BRDF also varies as a function of polarization, such that one would measure a different amount of scatter depending on the polarization state (Tx) of the incident light and the polarization component (Rx) of the reflected light that is passed through to the detector. A material's polarimetric (or polarization-dependent) BRDF, written $BRDF(\theta_i,\phi_i,\theta_s,\phi_s,\text{Tx},\text{Rx})$, can be computed from its geometry-dependent Mueller matrix, written $M(\theta_i,\phi_i,\theta_s,\phi_s)$, using Eq. 17 as follows:

Eq. 41
$$BRDF(\theta_i,\phi_i,\theta_s,\phi_s,\text{Tx},\text{Rx}) = M^{Rx}_{row0}M(\theta_i,\phi_i,\theta_s,\phi_s)\vec{S}^{Tx}$$

where M^{Rx} and $\vec{S}^{Tx}$ are unitless, but $M(\theta_i,\phi_i,\theta_s,\phi_s)$ is given units of sr^{-1} [16]. By analogy with Eq. 22, one can make $N = 16$ different TxRx measurements at geometry $(\theta_i,\phi_i,\theta_s,\phi_s)$ to compute the Mueller matrix $M(\theta_i,\phi_i,\theta_s,\phi_s)$ at that geometry.

2.8. Motivation for Experiments and Simulations

The technical background provided in this chapter is the basis for all the experimental and theoretical efforts in this research. The theoretical concept of active polarimetry is derived from linear algebra relating a material's Mueller matrix to straightforward polarimetric measurements. In practice, however, active polarimetry can be complicated. Due to measurement errors, experimental Mueller matrices require filtering routines to ensure physical realizability before they can be decomposed. Another important nuance of active polarimetry is that a material's Mueller matrix is geometry-dependent, such that its observed polarimetric behavior depends on the illumination and viewing angles. In this way, a material's geometry-dependent Mueller matrix is directly related to its polarization-dependent BRDF (Eq. 41).

The goal of this thesis research is to investigate the potential utility of active polarimetry for characterizing space debris. As introduced in Section 1.3, space surveillance would be a unique application of active polarimetry because the targets (i.e., space debris fragments) are non-resolved, meaning all the light reflecting from a target would be collected in a single pixel. The phenomenology governing the performance of non-resolved active polarimetry is not well understood. Intuitively, it is expected that the polarimetric signature of a non-resolved object would be an aggregate of the polarimetric behavior of all its surface facets, each oriented differently with respect to the laser and receiver. However, previous studies [14, 31, 32, 33], which only conducted measurements of "coupon" material samples over a limited range of geometries (see Section 1.3.2), have not explored the issue of non-resolved object signatures in detail. This thesis research addresses this knowledge gap through a combination of experiments and modeling and simulation (M&S) to gain a better understanding of the phenomenology of non-resolved active polarimetry, particularly in the context of space surveillance.

The concept of the research approach here (Figure 7) is to experimentally determine the polarimetric behavior of spacecraft materials in order to simulate polarimetric signatures of non-resolved objects covered in those materials. Two types of experiments are presented. Experiment *A* uses a single-pixel detector to measure the polarimetric BRDF of a "coupon" sample of a material, which can be used to compute the material's Mueller matrix as a function of the illumination and viewing geometry, both bistatic and monostatic. Experiment *B* uses a camera to measure polarimetric images of small objects (e.g., spheres, cylinders, and panels) that are coated or covered in the same spacecraft materials from Experiment *A*, which can be used to determine the polarimetric signature of the object as if it was non-resolved. The setups for Experiments *A* and *B* are validated against reference data for several calibration materials. These experiments were conducted at a wavelength of $\lambda = 1064$ nm, since several ground-based laser radars currently used for space surveillance also operate at this wavelength using solid-state Nd:YAG lasers [9, 90]. Besides these experiments, a simulation is developed to predict the monostatic polarimetric signature of a non-resolved object. The simulation uses the measured (or modeled) polarimetric BRDFs of a database of materials and then geometrically determines the polarimetric signature of a non-resolved object coated or covered with one or more of those materials. The simulation is validated against the results of Experiment *B*. The next chapters describe the design, execution, and results of these experiments and simulations.

3. Experiment *A* - Polarimetric BRDFs

This chapter describes the design, execution, and results of Experiment *A*. The purpose of Experiment *A* is to experimentally determine the polarimetric behavior of "coupon" samples of spacecraft materials as a function of the illumination and viewing geometry. Experiment *A* uses a bench-top polarimeter with a single-pixel detector to measure the polarimetric BRDFs of spacecraft materials, thereby allowing the experimental estimation of their geometry-dependent Mueller matrices and polarimetric properties. Spacecraft materials are measured over a wide range of bistatic and monostatic geometries that is more comprehensive than any relevant dataset in the literature (Section 1.4). The spacecraft materials are then categorized in terms of their polarimetric behavior in the regions of diffuse (i.e., forward and backward scatter) and specular reflection. The polarimetric BRDFs measured in Experiment *A* are later shown to dictate the polarimetric signatures of objects covered in spacecraft materials.

3.1. Setup and Procedure

The setup for Experiment *A* is a bench-top *polarimeter* (diagram in Figure 9; picture in Figure 10). The polarimeter uses a continuous-wave (CW) laser (Spectra-Physics® model Excelsior 1064-800) with a wavelength of λ = 1064 nm. The raw laser beam, which is horizontally polarized, passes through a half-wave ($\lambda/2$) plate and quarter-wave ($\lambda/4$) plate, which are independently rotated (using Newport® PR50CC rotation stages) to control the polarization state (Tx) of the transmitted beam (i.e., $\vec{S}_{Tx}$ in Eq. 20). The beam (3 mm diameter) then encounters the material being measured. The reflected light is measured by two single-pixel, silicon detectors (Thorlabs model PDA36A), one for bistatic measurements and one for quasi-monostatic measurements (where the laser and detector are separated by < 1°). Each detector is preceded by a $\lambda/4$ plate and $\lambda/2$ plate, which are independently rotated (Newport® PR50CC) to control the received polarization state (Rx) (i.e., M^{Rx} in Eq. 20) and a fixed linear polarizer. The fixed linear polarizer ensures that regardless of which Rx is being measured, the detector is always directly illuminated with the same polarization state, thereby circumventing any unexpected polarization-dependent responsivity. Lenses and irises are used to give a field-of-view of 1 cm (on the material) and a subtended solid angle of Ω, respectively. To record a measurement, the laser is chopped at a frequency of 100 Hz and the detector's analog output is acquired using a lock-in amplifier (Princeton Applied Research Model 5209).

Rotation stages (Newport® RV120CCHL) are additionally used to control the illumination and viewing geometry. The material is rotated (in the plane of the diagram) to achieve arbitrary incident zenith angles (θ_i) for a fixed azimuth angle (ϕ_i). For monostatic angular scans, only the material is rotated to scan over incident/scatter zenith angle $\theta = \theta_i = \theta_s$. For bistatic angular scans for a fixed θ_i, the bistatic receiver assembly is rotated about the laser spot (on the material) to achieve arbitrary scatter zenith angles (θ_s) in the plane of incidence. All rotation stages are motorized and data collection is automated using Matlab®.

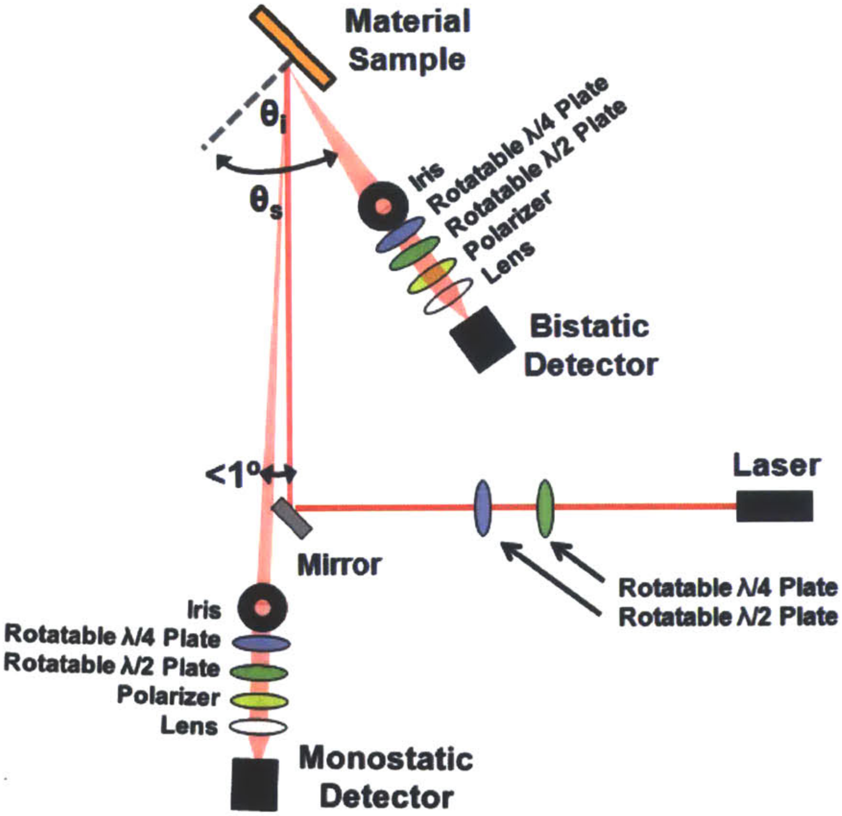

Figure 9: Diagram of bench-top polarimeter for Experiment *A*

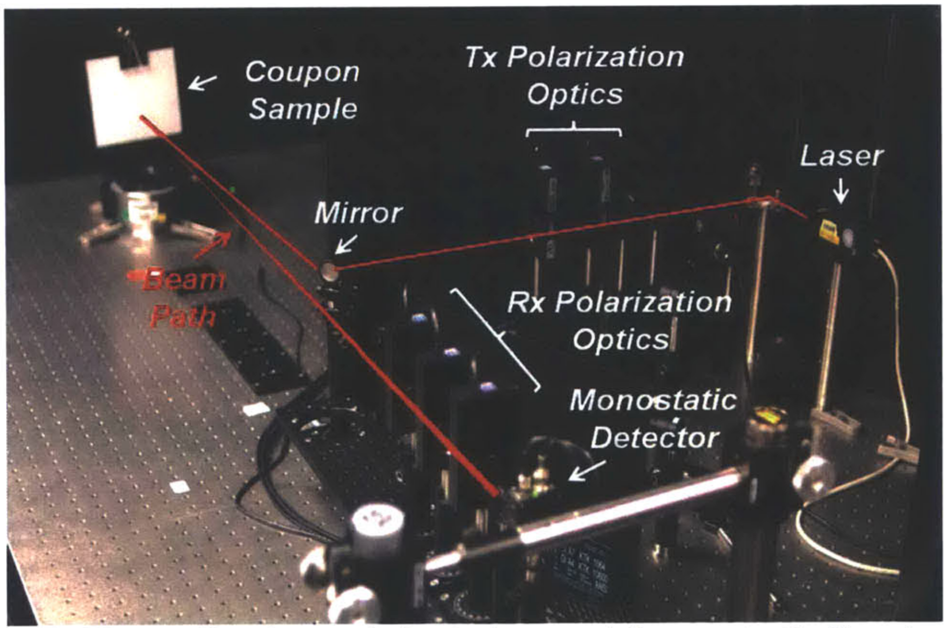

Figure 10: Picture of bench-top polarimeter in monostatic geometry for Experiment *A*

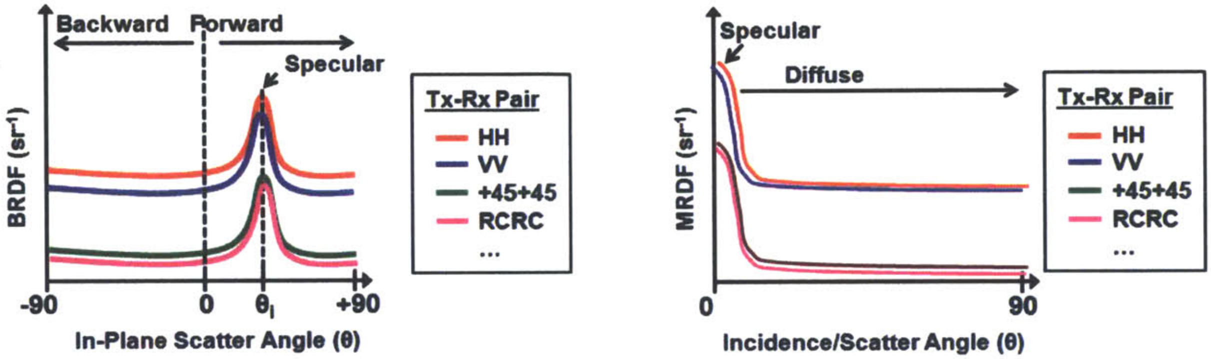

Figure 11: Hypothetical polarimetric BRDFs expected to be obtained in Experiment *A*: in-plane bistatic scans (left) and monostatic scans (right)

Since the bench-top polarimeter measures a material's bistatic or monostatic BRDF as a function of zenith angle at fixed azimuth angle, a simplified nomenclature and notation for the polarimetric BRDF is adopted here. Henceforth, the term "BRDF" will refer only to an in-plane bistatic scan (Figure 11), written mathematically as $BRDF(\theta_i,\theta,Tx,Rx)$ where the azimuth arguments have been dropped and the scatter zenith angle θ_s has been replaced by θ (-90° to 90°). The backward, forward, and specular scatter regimes are defined by $\theta < 0°$, $\theta > 0°$, and $\theta \approx \theta_i$, respectively. Meanwhile, the term "MRDF" ("M" for monostatic) refers to a monostatic scan (Figure 11), written mathematically as $MRDF(\theta,Tx,Rx)$ where the incident and scatter zenith angles are equal, by definition, and represented by θ (0° to 90°). Here, the specular and diffuse regimes are defined by $\theta \approx 0°$ and $\theta > 0°$, respectively.

At a given illumination and viewing geometry, the intensity $I_{TxRx}(\theta_i,\theta)$ [bistatic] or $I_{TxRx}(\theta)$ [monostatic] of the scattered light is measured for each of the 16 polarization pairs (TxRx) in Table 1. For simplicity, the intensity for each polarization pair is sequentially measured and immediately recorded, as opposed to a scheme with rotating retarders (DRR) and Fourier analysis [91]. The polarimetric BRDFs (in-plane bistatic scan) and MRDFs (i.e., monostatic scan) are then calculated as follows [88]:

Eq. 42

$$BRDF(\theta_i,\theta,\mathrm{Tx},\mathrm{Rx}) = \frac{I_{TxRx}(\theta_i,\theta)}{I_0\Omega\cos\theta}$$

$$MRDF(\theta,\mathrm{Tx},\mathrm{Rx}) = \frac{I_{TxRx}(\theta)}{I_0\Omega\cos\theta}$$

where I_0 is the intensity of the incident beam (which is the same for all Tx) and Ω is the solid angle subtended by the iris. The solid angle is related to the diameter d of the receiving iris and the range R from the material to the iris as follows:

Eq. 43

$$\Omega = 2\pi(1-\cos\chi)$$

Eq. 44

$$\chi = \frac{1}{2}\tan^{-1}\left(\frac{d}{R}\right)$$

where χ is half the angle subtended by the iris at the target distance. At a given illumination and viewing geometry, each polarimetric BRDF or MRDF contributes a linearly independent equation in the form of Eq. 19, which allows estimation of the geometry-dependent Mueller matrix using Eq. 27. For bistatic geometries, the Mueller matrix $\vec{M}(\theta_i, \theta)$ (in vector form) is solved by:

Eq. 45

$$\vec{M}(\theta_i, \theta) = H^{-1}\vec{I}(\theta_i, \theta)$$

where H^1 is same as in Eq. 29 and the intensity vector $\vec{I}(\theta_i, \theta)$ is defined similarly to Eq. 26 as:

Eq. 46

$$\vec{I}(\theta_i, \theta) = \begin{bmatrix} I_{Tx^1Rx^1}(\theta_i, \theta) \\ I_{Tx^2Rx^2}(\theta_i, \theta) \\ \cdots \\ I_{Tx^{16}Rx^{16}}(\theta_i, \theta) \end{bmatrix}$$

For the monostatic case, the Mueller matrix $\vec{M}(\theta)$ (in vector form) is solved by:

Eq. 47

$$\vec{M}(\theta) = H^{-1}\vec{I}(\theta)$$

where H^1 is same as in Eq. 29 and the intensity vector $\vec{I}(\theta)$ is defined similarly to Eq. 26 as

Eq. 48

$$\vec{I}(\theta) = \begin{bmatrix} I_{Tx^1Rx^1}(\theta) \\ I_{Tx^2Rx^2}(\theta) \\ \cdots \\ I_{Tx^{16}Rx^{16}}(\theta) \end{bmatrix}$$

Each estimate Mueller matrix is filtered to ensure physical realizability (Section 2.6.1) and then decomposed (in the form of Eq. 8) to calculate its polarimetric properties as functions of the illumination and viewing angles.

3.1.1. Error Analysis

Since the bench-top polarimeter computes BRDF values from measured variables, the estimated BRDF will have error bounds. According to Eq. 42, the BRDF or MRDF value is a function of the measured variables I_{TxRx}, I_0, Ω, and θ, which are uncorrelated. Therefore, the variance σ^2_{BRDF} on the estimated BRDF is found by applying Eq. 31:

Eq. 49

$$\sigma^2_{BRDF} = \left(\frac{\partial BRDF}{\partial I_{TxRx}}\right)^2 \sigma_I^2 + \left(\frac{\partial BRDF}{\partial I_0}\right)^2 \sigma_{I_0}^2 + \left(\frac{\partial BRDF}{\partial \Omega}\right)^2 \sigma_\Omega^2 + \left(\frac{\partial BRDF}{\partial \theta}\right)^2 \sigma_\theta^2$$

where σ_I^2, σ_{I0}^2, σ_Ω^2, and σ_θ^2 are variances on the measured I_{TxRx}, I_0, Ω, and θ, respectively. The partial derivatives in Eq. 49 are derived as follows:

Eq. 50

$$\frac{\partial BRDF}{\partial I_{TxRx}} = \frac{1}{I_0 \Omega \cos\theta}$$

Eq. 51

$$\frac{\partial BRDF}{\partial I_0} = \frac{-I_{TxRx}}{I_0^2 \Omega \cos\theta}$$

Eq. 52

$$\frac{\partial BRDF}{\partial \Omega} = \frac{-I_{TxRx}}{I_0 \Omega^2 \cos\theta}$$

Eq. 53

$$\frac{\partial BRDF}{\partial \theta} = \frac{I_{TxRx} \sin\theta}{I_0 \Omega \cos^2\theta}$$

Eq. 49 can be used to determine the error bounds on any BRDF measured by the bench-top polarimeter. All that is needed is a set of values for the standard deviations σ_I, σ_{I0}, σ_Ω, and σ_θ, i.e., the square roots of the variances. The standard deviation σ_I on the measured intensity I comes from laser power fluctuations, detector noise, and misalignment of the polarizers and wave plates in Figure 9. To determine the effect of laser power fluctuations and detector noise, the laser was sent directly into the detector and I was measured 1,000 times. The standard deviation of these measurements was found to be ±1%. It was judged that all polarizers and wave plates were aligned within a standard deviation of ±1°. Monte Carlo simulations were run to determine the standard deviation on the throughput power if each polarizer and wave plate were randomly misaligned with a standard deviation of ±1°. The result was a standard deviation of ±1% on the throughput power. Combing the effects from laser power fluctuations and detector noise (±1%) and polarizer/wave plate misalignments (±1%), the standard deviation σ_I on the measured intensity I during a BRDF scan would be about ±2%, i.e., $\sigma_I = 0.02\ I$. The standard deviation σ_{I0} of the incident beam power I_0 was determined to follow the same relationship, i.e., $\sigma_{I0} = 0.02\ I_0$.

Next, the standard deviation σ_Ω of the solid angle Ω is determined as follows. According to Eq. 43, the solid angle Ω is a function of the half-angle χ subtended by the iris. Applying Eq. 31, the variance σ_Ω^2 of the solid angle Ω is related to the variance σ_χ^2 of the subtended half-angle χ as follows:

Eq. 54

$$\sigma_\Omega^2 = \left(\frac{\partial \Omega}{\partial \chi}\right)^2 \sigma_\chi^2$$

According to Eq. 44, the half-angle χ is a function of two measured variables, i.e., the iris diameter (d) and the range (R). Applying Eq. 31 again, the variance σ_χ^2 of the subtended half-angle χ is related to the variance σ_d^2 of the iris diameter d and the variance σ_R^2 of the range R as follows:

Eq. 55
$$\sigma_\chi^2 = \left(\frac{\partial \chi}{\partial d}\right)^2 \sigma_d^2 + \left(\frac{\partial \chi}{\partial R}\right)^2 \sigma_R^2$$

where the partial derivatives in Eq. 54 and Eq. 55 are:

Eq. 56
$$\frac{\partial \Omega}{\partial \chi} = 2\pi \sin \chi$$

Eq. 57
$$\frac{\partial \chi}{\partial R} = \frac{-D}{2R^2\left[(D/R)^2+1\right]} = \frac{-D}{2D^2+2R^2}$$

Eq. 58
$$\frac{\partial \chi}{\partial d} = \frac{1}{2R\left[(D/R)^2+1\right]} = \frac{1}{2D^2/R+2R}$$

The iris diameter d was measured with a micrometer to within 0.001 inch or 25.4 μm. The range R was measured with a meter stick within 1 mm. The variance of a uniform distribution of width x is $x^2/12$, giving a standard deviation of $x/\sqrt{12}$. Applying this formula, the standard deviations of interest here are $\sigma_d = 25.4\ \mu\text{m}/\sqrt{12}. = 7.33\ \mu\text{m}$ and $\sigma_R = 1\ \text{mm}/\sqrt{12} = 0.29$ mm.

Finally, the standard deviation σ_θ on the viewing angle θ is determined as follows. A series of tests were conducted in which a laser was shined on a mirror placed at the center of the rotation stage used to rotate the bistatic arm or target material (for monostatic scans). The rotation stage was then rotated such that the mirror deflected the laser directly over fiducials placed at 0°, ±45°, ±90°, and ±135° around the stage. It was found that alignment between the deflected laser and the fiducials was always achieved within ±0.1° of the expected angle. This constitutes an error with a uniform distribution over a width of 0.1°, giving a standard deviation of $\sigma_\theta = 0.1° /\sqrt{12} = 0.029°$.

In summary, the standard deviation σ_{TxRx} of the estimated BRDF at polarization pair TxRx is computed using Eq. 49, given the standard deviations of the underlying measured variables listed in Table 2.

Table 2: Standard Deviations of Measured Variables

Measured Variable	Standard Deviation
Intensity I	$\sigma_I = 0.02I$
Incident Intensity I_0	$\sigma_{I0} = 0.02I_0$
Iris diameter d	$\sigma_d = 7.33\ \mu\text{m}$
Range R	$\sigma_R = 0.29$ mm
Angle θ	$\sigma_\theta = 0.29°$

The error bounds on the measured intensities (I_{TxRx}) an then be used to determine the error bounds on the estimated geometry-dependent Mueller matrices. For bistatic geometries, the variance $\vec{\sigma}_m^2(\theta_i,\theta)$ of the Mueller matrix $\vec{M}(\theta_i,\theta)$ (in vector form) is found using Eq. 35 as follows:

Eq. 59
$$\vec{\sigma}_m^2(\theta_i,\theta) = K\vec{\sigma}_{TxRx}^2(\theta_i,\theta)$$

where the matrix K is the same as in Eq. 35 and the vector $\vec{\sigma}_{TxRx}^2(\theta_i,\theta)$ is composed of the variances of the measured intensities at different polarization TxRx (from Eq. 35):

Eq. 60
$$\vec{\sigma}_{TxRx}^2(\theta_i,\theta) = \begin{bmatrix} \sigma_{HH}^2(\theta_i,\theta) \\ \sigma_{HV}^2(\theta_i,\theta) \\ \dots \\ \sigma_{RCRC}^2(\theta_i,\theta) \end{bmatrix}$$

For monostatic geometries, the variance $\vec{\sigma}_m^2(\theta)$ of the Mueller matrix $\vec{M}(\theta)$ (in vector form) is found using Eq. 35 follows:

Eq. 61
$$\vec{\sigma}_m^2(\theta) = K\vec{\sigma}_{TxRx}^2(\theta)$$

where the matrix K is the same as in Eq. 35 and the vector $\vec{\sigma}_{TxRx}^2(\theta)$ is composed of the variances of the measured intensities at different polarizations TxRx (from Eq. 35):

Eq. 62
$$\vec{\sigma}_{TxRx}^2(\theta) = \begin{bmatrix} \sigma_{HH}^2(\theta) \\ \sigma_{HV}^2(\theta) \\ \dots \\ \sigma_{RCRC}^2(\theta) \end{bmatrix}$$

3.1.2. Data Processing Chain

At this point, it is useful to summarize the measurement and processing chain of Experiment *A* using the bench-top polarimeter:

- Measure the incident beam intensity I_0 by removing the material sample and rotating the bistatic assembly such that the incident beam goes directly into detector. Measurement of I_0 only has to be performed once. The same value of I_0 can then be used while processing data for any angle of incidence θ_i and material sample.
- Compute the solid angle Ω using Eq. 43 after measuring the iris diameter *d* and range *R*. The solid angle (and subtended half-angle) for the bistatic receiver assembly was set at Ω = 500 μsr (and $\chi = 0.7°$), which was just large enough to allow the detection of scatter at cross-polarization (e..g, HV) for all spacecraft materials of interest. The solid angle for the monostatic assembly was less, i.e., Ω = 100 μsr ($\chi = 0.25°$), but could not be made any larger without the mirror (Figure 9) blocking the scattered light from flooding the iris. Solid angles of these sizes (for bistatic and monostatic) are common for measuring combinations of diffuse and specular materials [88], as were encountered in Experiment *A*. Computation of Ω only has to be performed once. The same value of Ω can then be used while processing data for any material sample.

- Insert and illuminate a material sample and measure the intensities $I_{TxRx}(\theta_i, \theta)$ [bistatic] and $I_{TxRx}(\theta)$ [monostatic] of the scattered light as functions of the illumination and viewing geometry and the polarization pair TxRx.
- Compute the polarimetric $BRDF(\theta_i,\theta,Tx,Rx)$ and $MRDF(\theta,Tx,Rx)$ using Eq. 42.
- Compute the geometry-dependent Mueller matrices $\vec{M}(\theta_i, \theta)$ and $\vec{M}(\theta)$ (in vector form) using Eq. 45 and Eq. 47, respectively.
- Compute the error bounds $\vec{\sigma}^2_{TxRx}(\theta_i, \theta)$ and $\vec{\sigma}^2_{TxRx}(\theta)$ of the BRDF and MRDF, respectively, using Eq. 49.
- Compute the error bounds $\vec{\sigma}^2_m(\theta_i, \theta)$ and $\vec{\sigma}^2_m(\theta)$ of the bistatic and monostatic Mueller matrices, respectively, using Eq. 59 and Eq. 61, respectively.
- Apply Cloude's filtering method to $\vec{M}(\theta_i, \theta)$ and $\vec{M}(\theta)$ according to Section 2.6.
- Decompose $\vec{M}(\theta_i, \theta)$ and $\vec{M}(\theta)$ in the form of Eq. 11 according to Section 2.6.
- Compute the geometry dependent diattenuation $D(\theta_i,\theta)$ and $D(\theta)$ using Eq. 16.
- Compute the geometry dependent retardance $R(\theta_i,\theta)$ and $R(\theta)$ using Eq. 17.
- Compute the geometry dependent depolarization power $\Delta(\theta_i,\theta)$ and $\Delta(\theta)$ using Eq. 18.
- Compute the geometry dependent polarizance $P(\theta_i,\theta)$ and $P(\theta)$ using Eq. 19.
- Compute the error bounds $\vec{\sigma}^2_D(\theta_i, \theta)$ and $\vec{\sigma}^2_D(\theta)$, $\vec{\sigma}^2_R(\theta_i, \theta)$ and $\vec{\sigma}^2_R(\theta)$, and $\vec{\sigma}^2_\Delta(\theta_i, \theta)$ and $\vec{\sigma}^2_\Delta(\theta)$ of the estimation diattenuation, retardance, and depolarization power, respectively, using Eq. 40.

Using the bench-top polarimeter, the steps above provide estimates of a material's polarimetric BRDF and MRDF, as well as its geometry-dependent Mueller matrix and polarimetric properties, all with error bounds. This was precisely the goal of Experiment *A*. All results from Experiment *A* are products of this processing chain.

3.2. Validation

The bench-top polarimeter (Figure 9) was validated in terms of its ability to measure (1) a reference sample with a known BRDF and MRDF and (2) some common optical elements with known Mueller matrices and polarimetric properties.

First, the polarimeter was used to measure the (in-plane bistatic) BRDF and MRDF of a sample of Spectraflect®, a coating that is approximately Lambertian over a wavelength range of 350 - 2400 nm [92]. The manufacturer (Labsphere®) provided reference data on Spectraflect®, including in-plane BRDF values at an incident angle of $\theta_i = 30°$, a wavelength of $\lambda = 633$ nm, a Tx polarization of H (i.e., horizontally or "p" polarized), and an Rx polarization of U (or unpolarized, i.e., there was no polarization analyzer in front of the detector). The manufacturer also provided limited MRDF values at $\lambda = 633$ and polarization pair HU. For comparison, the polarimeter was used to measure the (in-plane bistatic) BRDF of Spectraflect® for $\lambda = 1064$ nm, $\theta_i = 30°$, and TxRx polarizations of HH and HV (separately). Also measured was the MRDF at HH and HV. Following Pickering's method [93], the sum of the measurements at HH and HV should be equivalent to the reference data at HU. Spectral differences between the polarimeter's measurement (1064 nm) and the reference (633 nm) are expected to be negligible [92].

As plotted in Figure 12, the polarimeter's BRDF and MRDF measurements match the reference data within the error bounds of the measurement at almost every angle. This result validates the polarimeter's ability to accurately measure BRDF and MRDF curves.

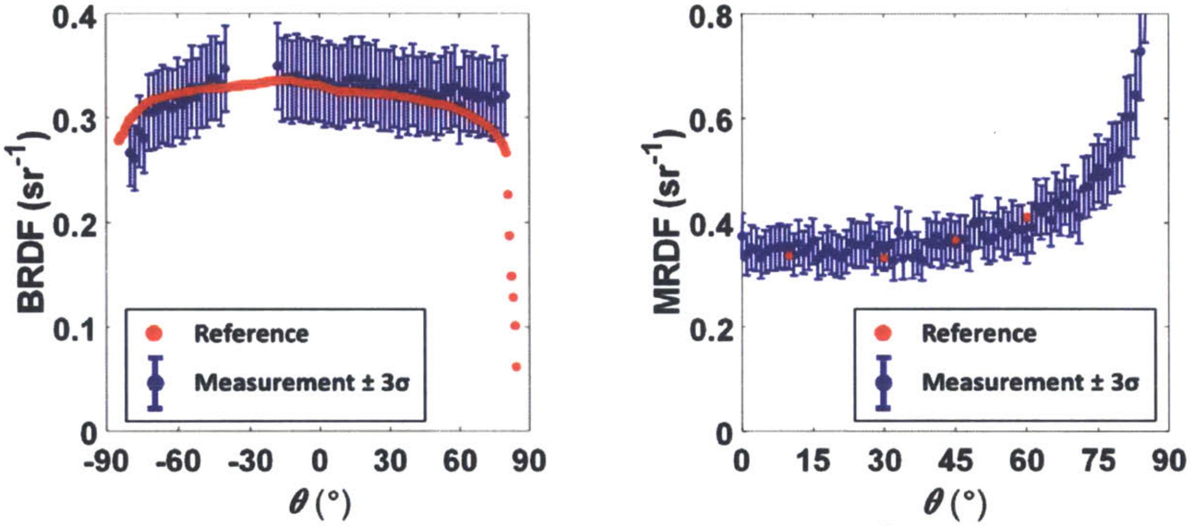

Figure 12: BRDF ($\theta_i = 30°$) [left] and MRDF [right] of Spectraflect® at polarization HU (measurement vs. reference)

For clarity, a few features of the reference data and the polarimeter's measurement should be noted. As expected for a Lambertian surface [88] the reference (and measured) bistatic BRDF of Spectraflect® is approximately constant at $\pi^{-1} \approx 0.32$ sr^{-1}. By contrast, the reference (and measured) MRDF increases with angle s, e.g., 0.34 sr^{-1} at $\theta = 0°$ and 0.41 sr^{-1} at $\theta = 60°$. Reference data points were provided for $\theta = -85°$ to 85° at 0.5 degree resolution for BRDF, but only at a few angles (θ = 0, 15, 30, 45 and 60°) for MRDF. In the BRDF measured by the polarimeter, there are no measurements at angles $\theta = -40°$ to -20°, because the bistatic receiver assembly would occlude (or block) the laser before hitting the material sample at these angles. These data gaps exist in all of the polarimeter's bistatic scans.

Next, the polarimeter was used to measure several common (transmissive) optical elements, where each element was illuminated at normal incidence and the detector assembly was positioned directly on the other side of the element. From the 16 prescribed polarimetric measurements (Table 1), the Mueller matrix and polarimetric properties of each optical element were calculated. Despite measurement noise, all estimated Mueller matrices have associated eigenvalue ratios (Eq. 30) of $\gamma < -18$ dB, indicating that they are all extremely close to physically realizable (i.e., valid) matrices.

Table 3 shows the theoretical and measured Mueller matrices for air, a horizontally-oriented linear polarizer, a half-wave with horizontally-oriented fast-axis, and a quarter-wave plate with horizontally-oriented fast axis. Table 4 compares the measured properties with the theoretical ones for each of the measured optical elements. The measured Mueller matrices and polarimetric properties match the theoretical ones well within the error bounds of the measurements. Previous studies [32] achieved errors comparable to the polarimeter here when measuring reference samples. These results validate that the bench-top polarimeter (Figure 9) accurately takes polarimetric measurements, computes Mueller matrices, decomposes them, and computes their polarimetric properties.

Table 3: Comparison of theoretical and measured Mueller matrices of reference samples

Ref. Sample	Mueller Matrix	
	Theory	**Measurement ± 3σ**
Air	$\begin{bmatrix} 1 & 0 & 0 & 0 \\ 0 & 1 & 0 & 0 \\ 0 & 0 & 1 & 0 \\ 0 & 0 & 0 & 1 \end{bmatrix}$	$\begin{bmatrix} 1.00 & -0.01 & 0.01 & -0.02 \\ -0.01 & 1.00 & 0.03 & -0.00 \\ 0.01 & -0.02 & 1.00 & -0.04 \\ -0.02 & 0.01 & 0.02 & 1.01 \end{bmatrix} \pm \begin{bmatrix} 0 & 0.04 & 0.06 & 0.06 \\ 0.04 & 0.00 & 0.06 & 0.06 \\ 0.06 & 0.06 & 0.10 & 0.10 \\ 0.06 & 0.06 & 0.09 & 0.10 \end{bmatrix}$
Polarizer	$\begin{bmatrix} 1 & 1 & 0 & 0 \\ 1 & 1 & 0 & 0 \\ 0 & 0 & 0 & 0 \\ 0 & 0 & 0 & 0 \end{bmatrix}$	$\begin{bmatrix} 1.00 & 1.00 & 0.01 & -0.01 \\ 1.00 & 1.00 & 0.01 & -0.01 \\ -0.01 & -0.01 & -0.01 & 0.00 \\ 0.00 & 0.00 & 0.00 & -0.01 \end{bmatrix} \pm \begin{bmatrix} 0 & 0.00 & 0.08 & 0.08 \\ 0.00 & 0.00 & 0.08 & 0.08 \\ 0.08 & 0.08 & 0.12 & 0.12 \\ 0.08 & 0.08 & 0..12 & 0.12 \end{bmatrix}$
λ/2 Plate	$\begin{bmatrix} 1 & 0 & 0 & 0 \\ 0 & 1 & 0 & 0 \\ 0 & 0 & -1 & 0 \\ 0 & 0 & 0 & -1 \end{bmatrix}$	$\begin{bmatrix} 1.00 & -0.01 & -0.01 & 0.02 \\ -0.01 & 1.00 & 0.00 & 0.00 \\ -0.01 & 0.00 & -1.00 & 0.05 \\ 0.01 & 0.00 & -0.01 & -1.01 \end{bmatrix} \pm \begin{bmatrix} 0 & 0.04 & 0.06 & 0.06 \\ 0.04 & 0.00 & 0.06 & 0.06 \\ 0.06 & 0.06 & 0.13 & 0.09 \\ 0.06 & 0.06 & 0.09 & 0.13 \end{bmatrix}$
λ/4 Plate	$\begin{bmatrix} 1 & 0 & 0 & 0 \\ 0 & 1 & 0 & 0 \\ 0 & 0 & 0 & 1 \\ 0 & 0 & -1 & 0 \end{bmatrix}$	$\begin{bmatrix} 1.00 & -0.01 & 0.03 & 0.01 \\ -0.01 & 1.00 & 0.01 & 0.00 \\ -0.01 & 0.00 & 0.03 & 0.98 \\ -0.01 & 0.01 & -1.04 & 0.00 \end{bmatrix} \pm \begin{bmatrix} 0 & 0.04 & 0.06 & 0.06 \\ 0.04 & 0..00 & 0.06 & 0.06 \\ 0.06 & 0.06 & 009 & 0.10 \\ 0.06 & 0.06 & 0.13 & 0.09 \end{bmatrix}$

Table 4: Comparison of theoretical and measured polarimetric properties of reference samples

Reference Sample	*D*		*R*		Δ	
	Theory	**Measurement ±3σ**	**Theory**	**Measurement ±3σ**	**Theory**	**Measurement ±3σ**
Air	0	0.03 ± 0.05	0°	1.7 ± 4.6°	0	0.01 ± 0.04
Polarizer	1	1.00 ± 0.06	0°	2.2 ± 5.8°	0	0.00 ± 0.06
λ/2 Plate	0	0.03 ± 0.05	180°	178.4 ± 5.0°	0	0.01 ± 0.05
λ/4 Plate	0	0.03 ± 0.05	90°	89.2 ± 4.8°	0	0.01 ± 0.05

3.3. *Measurement of Spacecraft Materials*

After validation, the bench-top polarimeter was used to measure the polarimetric BRDFs (i.e., in-plane bistatic scans) and MRDFs (i.e., monostatic scans) of several materials and coatings commonly found on man-made satellites and debris, including:

- **Glossy White Paint** (Aeroglaze® A276 on an aluminum substrate): an organic thermal control paint, with low solar absorptivity (α_{Solar} = 0.23) and high infrared (IR) emissivity (ε_{IR} = 0.9), used on spacecraft surfaces to maintain a cool temperature while in sunlight [30, 94, 95].
- **Matte Black Paint** (Aeroglaze® Z306 on an aluminum substrate): an organic thermal control paint with nearly equal solar absorptivity (α_{Solar} = 0.96) and IR emissivity (ε_{IR} = 0.91) used on spacecraft surfaces [96, 97].
- **Black Kapton®** (with Vapor Deposited Aluminum [VDA] on one side): a polyimide film used in the multi-layer insulation (MLI) commonly found on spacecraft [30].
- **Silver Teflon®**: a radiating material with a low absorptivity-emissivity ratio ($\alpha_{Solar}/\ \varepsilon_{IR}$ = 0.12) used as a "solar reflector" on spacecraft surfaces [30].
- **Aluminum** (6061-T6): a common aluminum alloy used in the structures of spacecraft in the form of a panels and struts.
- **Titanium** (6AL-4V): a common titanium alloy used in the structures and booms of spacecraft.

As pictured in Figure 13, these spacecraft materials were all procured in the form of "coupon" samples, i.e., flat, 6" x 6" squares, with the exception of the titanium sample, which was a 1" diameter cylindrical rod. The titanium rod was mounted with the rod oriented parallel to the plane of the schematic in Figure 9, such that the incident beam was extended along its length for non-zero angles of incidence. This mounting scheme avoided the curvature of the rod to ensure that the entire beam was incident on the sample at the approximately same angle.

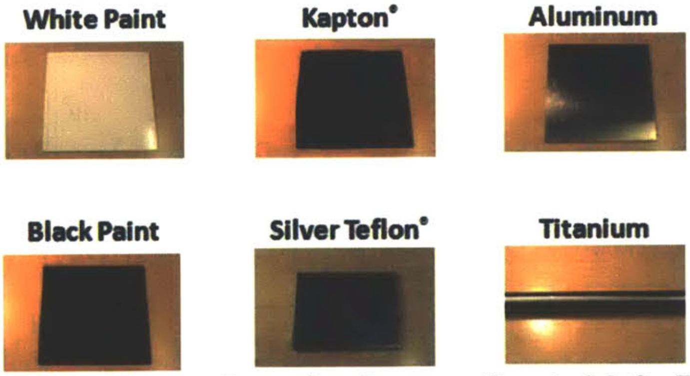

Figure 13: Pictures of "coupon" samples of spacecraft materials for Experiment *A*

The polarimeter was used to measure the polarimetric BRDF of each spacecraft material for incident angles of θ_i = 15°, 30°, 45°, 60° and 75° and scatter angles θ from -80° to 80° with 1° resolution around the expected specular point (±10°) and 5° resolution elsewhere. Also measured was the polarimetric MRDF (i.e., monostatic scan) at incident/scatter angles θ from 0 to 85° (at higher angles the spot size became elongated beyond the edge of the material samples) with 0.1° resolution around the expected specular point (±10°) and 1° resolution elsewhere. BRDFs and MRDFs were measured for the 16 prescribed polarization pairs (Table 1), allowing estimation of each material's Mueller matrices and polarimetric properties as functions of the illumination and viewing geometry.

3.4. Results and Analysis

This section presents the results of Experiment *A* for the spacecraft materials introduced above.

3.4.1. Polarimetric BRDFs

Considered first are the BRDFs and MRDFs measured for each spacecraft material for a single polarization pair. Figure 14 shows each spacecraft material's BRDF measured at polarization pair HH and several incident angles θ_i, while Figure 15 shows their MRDFs at HH. All materials have a dominant specular component at $\theta = \theta_i$, with the exception of matte black paint, which is mostly diffuse but with significantly increased forward scatter for high incident angles.

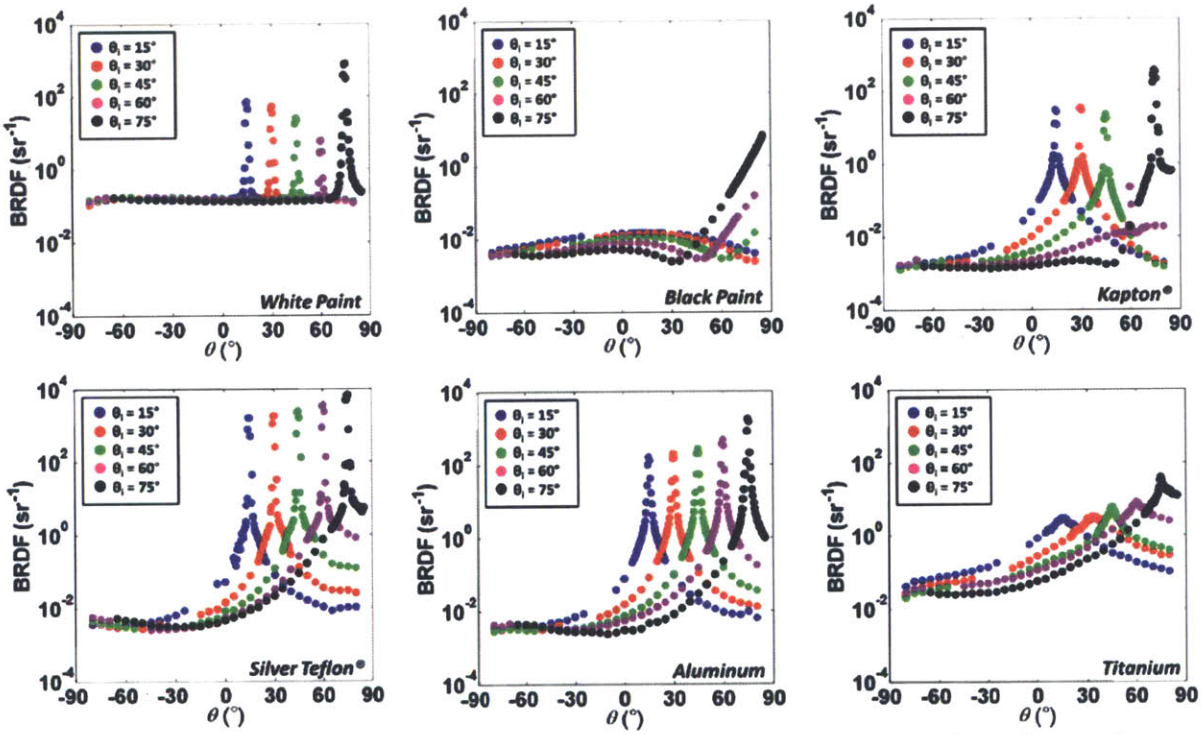

Figure 14: Measured BRDFs (i.e., in-plane bistatic scans) at HH from Experiment *A*

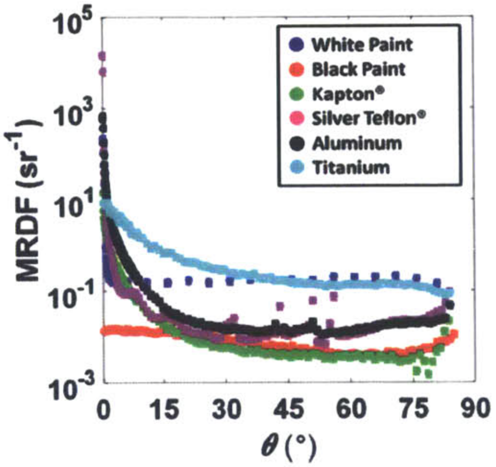

Figure 15: Measured MRDFs (i.e., monostatic scans) at HH from Experiment *A*

Next considered is the ensemble of 16 polarimetric BRDFs measured for a single material and incidence angle θ_i. Figure 16 shows such an ensemble for glossy white paint at $\theta_i = 60°$. Also shown is the computed Mueller matrix at a diffuse point ($\theta = -30°$) and specular point ($\theta = 60°$), each normalized by its top-left element m_{00}. The Mueller matrix at $\theta = -30°$ is visually recognizable as a strong depolarizer, such that all 16 BRDFs are of roughly equal magnitude at this point. By contrast, at the specular point, the Mueller matrix resembles that of a vertical linear polarizer, such that vertically (V) polarized incident light is preferentially reflected over horizontally (H) polarized incident light. At $\theta = 60°$ the BRDF at VV is significantly higher than the BRDF at HH (see inset). This diattenuating behavior at the specular point is expected from Fresnel's equation for a moderately high θ_i, which dictates that "s" polarized light (i.e., equivalent to V here) will be reflected more than "p" (or H) polarized light [16].

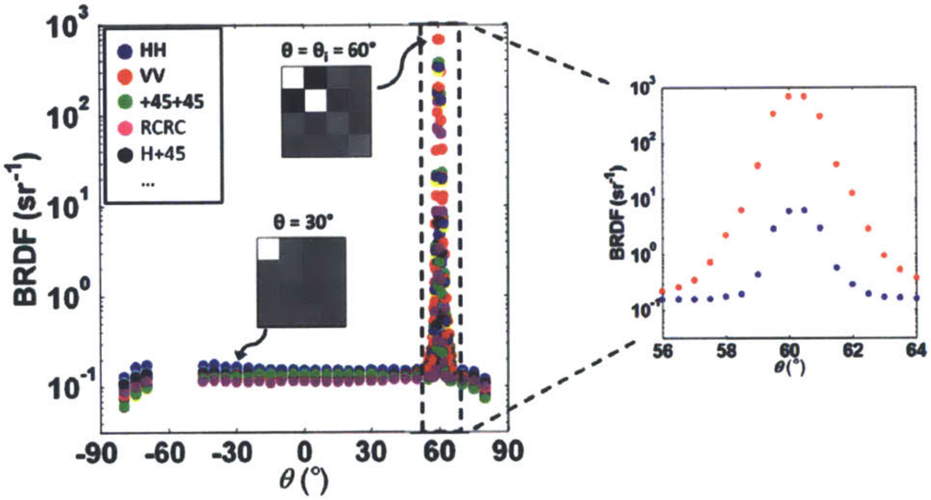

Figure 16: Measured BRDF ($\theta_i = 60°$) of white paint at 16 polarizations from Experiment *A*, with a magnified view of HH and VV in the inset. Estimated normalized Mueller matrices are shown as images at $\theta = 30°$ and 60°, where white, gray, and black squares correspond to values of +1, 0, and -1, respectively.

3.4.2. Polarimetric Properties

Plugging the 16 polarimetric BRDFs and MRDFs into Eq. 45 and Eq. 47, respectively, the Mueller matrices and polarimetric properties of each material were estimated as functions of angle, i.e., $M(\theta_i,\theta)$ for bistatic and $M(\theta)$ for monostatic. No attempt was made to smooth the measured polarimetric BRDFs or MRDFs with a low-pass filter or other smoothing method. All estimated Mueller matrices had associated eigenvalue ratios (Eq. 30) of $\gamma < -10$ dB, indicating that they were very close to physically realizable (i.e., valid) matrices.

3.4.3. Bistatic

Figure 17 plots the materials' bistatic polarimetric properties calculated from their measured polarimetric BRDFs (i.e., in-plane bistatic scans).. Each material's diattenuation (D), polarizance (P), retardance (R), and depolarization power (Δ) are plotted as functions of θ for all θ_i. The plots reveal some notable trends and value ranges in these bistatic polarimetric properties, as summarized in Table 5 according to the direction of scatter: backward ($\theta < 0$), forward ($\theta > 0$), and specular ($\theta \approx \theta_i$). All the materials exhibited mostly low diattenuation ($D < 0.5$) in the back scatter direction. However, in the forward scatter direction (including the specular), the metallic surfaces (i.e., titanium, aluminum, and silver Teflon®) continued exhibiting $D < 0.5$, while the two paints and Kapton® had the full range of diattenuation ($D = 0$ to 1). The polarizance (P) of each material follows the same trend as diattenuation. In terms of retardance, the silver Teflon® uniquely exhibited a finite range ($R = 30$ to 120°) in all scatter directions, while all other materials acted as mirrors ($R = 180°$) in the back scatter direction and had the full range of behavior ($R = 0$ to 180°) in the forward scatter direction. In terms of depolarization power, the glossy white paint was a nearly perfect depolarizer ($\Delta \approx 1$) in the back-scatter direction, but sharply lost depolarization power ($\Delta = 0$) at specular reflection. All other materials were mostly weak depolarizers ($\Delta < 0.5$) in all directions, except that silver Teflon® and aluminum exhibit moderately high depolarization power ($0.5 < \Delta < 0.8$) in the back scatter direction.

3.4.4. Monostatic

Figure 18 plots the materials' monostatic polarimetric properties (D, P, R, and Δ) calculated from their measured MRDFs. (i.e., monostatic scans). It should be mentioned that the polarimetric MRDFs at cross-polarizations (i.e., HV and VH) were undetectable for the matte black paint and Kapton® samples due to the monostatic assembly's relatively small solid angle (Section 3.1). Therefore, these undetectable MRDFs were simply set to zero at all angles θ, so that estimation of the geometry-dependent Mueller matrices of black paint and Kapton® was still possible. This manipulation of the data was deemed acceptable, because the resulting Mueller matrices were identical regardless of whether the undetectable MRDFs were set to zero (as was ultimately done) or to the sensitivity floor of the lock-in amplifier.

Table 6 summarizes the approximate trends in the materials' monostatic polarimetric properties with respect to the specular ($\theta \approx 0°$) and diffuse ($\theta > 0°$) regimes. All the materials exhibit very little diattenuation ($D < 0.1$) around the specular point, with the exception of Kapton®, which shows a slightly higher value of $D = 0.2$. Diattenuation increases monotonically into the diffuse region for all materials, achieving values as high as $D = 0.8$ for black paint and Kapton®, $D = 0.4$ for aluminum, and $D = 0.2$ for all other materials. The polarizance (P) of each material follows the same trend as diattenuation. In terms of retardance, all the materials are mirror-like ($R = 180°$) at all angles, except for silver Teflon®, which has a distinct retardance of $R = 115°$ at the specular point and a range of values elsewhere, and aluminum, which had a retardance of $R = 180°$ at the specular point and decreasing values into the diffuse region. The peculiar retardance of silver Teflon® also appeared in its bistatic behavior (Figure 17). Finally, in terms of depolarization power, all the materials are nondepolarizing ($\Delta = 0$) at the specular point and have increasing depolarizing power into the diffuse region. The white paint sample actually has a relatively constant depolarization power of $\Delta = 0.7$ to 0.9 in the diffuse region.

The significance of the trends identified in Table 5 and Table 6 become more apparent when considering the polarimetric signatures of objects covered in these same spacecraft materials. In Chapters 4 and 5, it is shown that the polarimetric properties of a non-resolved object are governed by the distributions of property values identified in Table 5 and Table 6. For now, the results of Experiment *A*, such as the high depolarization power ($\Delta > 0.7$) of glossy white paint and the unique retardance values (e.g., $R = 114°$ at monostatic specular) of silver Teflon® do suggest that active polarimetry may offer some additional utility over passive systems, which cannot probe these specific features.

3.4.5. Error Analysis

Error bounds on the estimated polarimetric properties were computed using Eq. 40. Figure 19 plots the same monostatic polarimetric properties as in Figure 18, but now with 3σ error bars. In general, the estimated diattenuation, retardance, and depolarization power have consistent error bounds of $3\sigma_D = 0.05$, $3\sigma_R = 5°$, and $3\sigma_\Delta = 0.05$, respectively. A closed-form or empirical formula for the error bound on polarizance is not found in the literature, but is likely similar to that of diattenuation. These error bounds are used in Chapter 5, where simulated properties of non-resolved objects (given the polarimetric BRDFs measured here in Experiment *A*) are compared to the experimentally-determined polarimetric properties of non-resolved objects in Experiment *B*.

3.4.6. Anisotropy

All the polarimetric BRDFs, MRDFs, and properties presented in Sections 3.4.1 through 3.4.4 were measured at a fixed incident azimuth angle $\phi_i = 0°$ (arbitrarily defined). However, a given material may exhibit *anisotropy*, by which the behavior of the material depends on the azimuth angle of the incident light. For a brief demonstration of the issue of anisotropy, the polarimeter was used to measure polarimetric MRDFs at one additional azimuth angle (i.e., $\phi_i = 90°$) for three of the spacecraft materials: glossy white paint, matte black paint, and silver Teflon®. Figure 20 shows these materials' polarimetric properties for azimuth angles of $\phi_i = 0°$ (identical to Figure 18) and $\phi_i = 90°$. According to the plots, the glossy white paint and matte black paint are isotropic, since their polarimetric properties (vs. θ) are identical (within their error bounds) at the two azimuth angles. By contrast, silver Teflon® exhibits some anisotropic behavior. The diattenuation, polarizance, and depolarization power (vs. θ) are similar at the two azimuth angles, but the retardance (R) profile is remarkably different. At both azimuth angles, the retardance of silver Teflon® is $R = 155°$ at the specular point ($\theta = 0°$), then trends downward for $\phi_i = 0°$ but upward for $\phi_i = 90°$ with increasing θ. These results demonstrate the possibility of anisotropic polarimetric behavior. A high resolution scan over different incident azimuth angles for all the spacecraft materials was beyond the scope of this thesis research. In future work, anisotropies could be measured in more detail, which would improve the ability to predict the behavior of arbitrarily oriented object surfaces.

3.5. Summary of Experiment A

Experiment A measured the polarimetric BRDFs and MRDFs of several spacecraft materials, which allowed estimation of their geometry-dependent Mueller matrices and polarimetric properties. The materials exhibited notable trends in their polarimetric behavior as a function of the illumination and viewing geometry. At specular points, metallic surfaces (i.e., aluminum and titanium) exhibited mirror-like behavior ($D = 0$, $R = 180°$, $\Delta = 0$), while paints and thin films (e.g., Kapton®) were diattenuating ($D > 0$), as expected from Fresnel reflection. Meanwhile, all these materials tended to be more depolarizing in the monostatic diffuse regime, since diffuse reflections tend to be depolarized by surface roughness [16, 88]. Silver Teflon® followed the trends of a metallic surface, with the exception of its distinctly finite band of retardance values in the specular and diffuse regions.

Experiment A considered the polarimetric behavior of "coupon" samples of spacecraft materials. However, the actual phenomenology of interest to space surveillance is the polarimetric signature of a non-resolved object. After all, space debris fragments are 3D objects that would be non-resolved when measured by a ground-based polarimetric laser radar. Intuitively, it is expected that the polarimetric signature of a non-resolved object would be an aggregate sum of the polarimetric behavior of all its coupon-like surface facets, each oriented differently with respect to the laser and receiver. Consequently, polarimetric BRDFs measured here in Experiment A (as in previous studies) contribute to object signatures, but they do not completely explain the phenomenology of non-resolved polarimetry. This knowledge gap is the motivation for Experiment B (Chapter 4) and the subsequent M&S (Chapter 5).

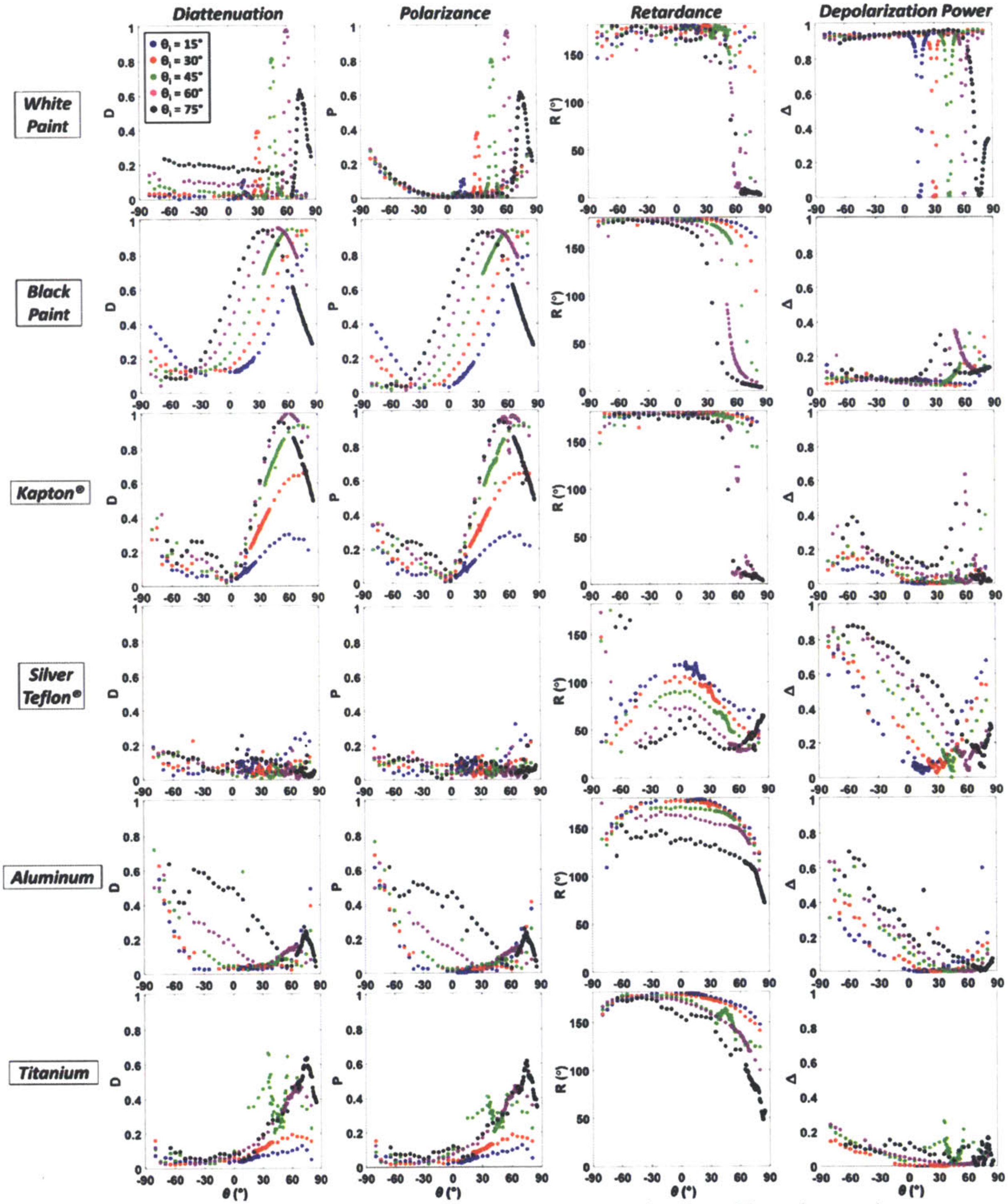

Figure 17: Measured bistatic polarimetric properties from Experiment *A*

Table 5: Trends in bistatic polarimetric properties from Experiment *A*

<table>
<tr><th rowspan="2">Spacecraft Material</th><th colspan="3">Diattenuation (D) and Polarizance (P)</th><th colspan="3">Retardance (R)</th><th colspan="3">Depolarization Power (Δ)</th></tr>
<tr><th>Back. $(\theta < 0^\circ)$</th><th>Forw. $(\theta > 0^\circ)$</th><th>Specular $(\theta \approx \theta_i)$</th><th>Back. $(\theta < 0^\circ)$</th><th>Forw. $(\theta > 0^\circ)$</th><th>Specular $(\theta \approx \theta_i)$</th><th>Back. $(\theta < 0^\circ)$</th><th>Forw. $(\theta > 0^\circ)$</th><th>Specular $(\theta \approx \theta_i)$</th></tr>
<tr><td>White Paint</td><td rowspan="3">< 0.5</td><td rowspan="3">0 – 1</td><td rowspan="3">0 – 1*</td><td rowspan="5">180º</td><td rowspan="3">0 - 180°</td><td rowspan="3">0 - 180°*</td><td>1</td><td>0 - 1</td><td rowspan="6">0*</td></tr>
<tr><td>Black Paint</td><td rowspan="3">< 0.5</td><td rowspan="5">< 0.5</td></tr>
<tr><td>Kapton®</td></tr>
<tr><td>Titanium</td><td colspan="3" rowspan="3">< 0.5</td><td colspan="2">> 40°</td></tr>
<tr><td>Aluminum</td><td colspan="2">> 70°</td><td rowspan="2">0 - 1</td></tr>
<tr><td>Silver Teflon®</td><td colspan="3">30° to 120°</td></tr>
</table>

* Specular trends do not apply to matte black paint

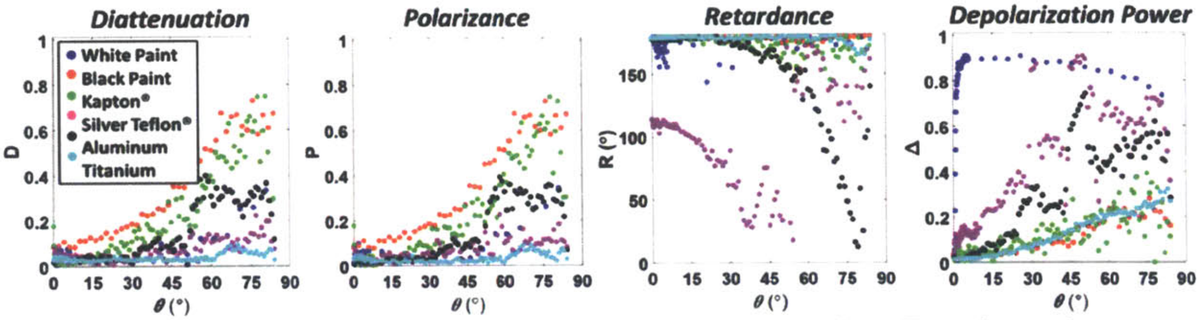

Figure 18: Measured monostatic polarimetric properties from Experiment *A*

Table 6: Trends in monostatic polarimetric properties from Experiment *A*

Spacecraft Material	Diattenuation (*D*) and Polarizance (*P*)		Retardance (*R*)		Depolarization Power (Δ)	
	Diffuse ($\theta > 0°$)	Specular ($\theta \approx 0°$)	Diffuse ($\theta > 0°$)	Specular ($\theta \approx 0°$)	Diffuse ($\theta > 0°$)	Specular ($\theta \approx 0°$)
White Paint	< 0.4	< 0.1	180°	> 150°	0.7 - 0.9	0
Black Paint	< 0.8			180°	< 0.3	
Kapton®		0.2	> 150°		< 0.5	
Silver Teflon®	< 0.3	< 0.1	0° - 180°	115°	< 0.9	
Aluminum	< 0.4			180°	< 0.7	
Titanium	< 0.2		180°		< 0.3	

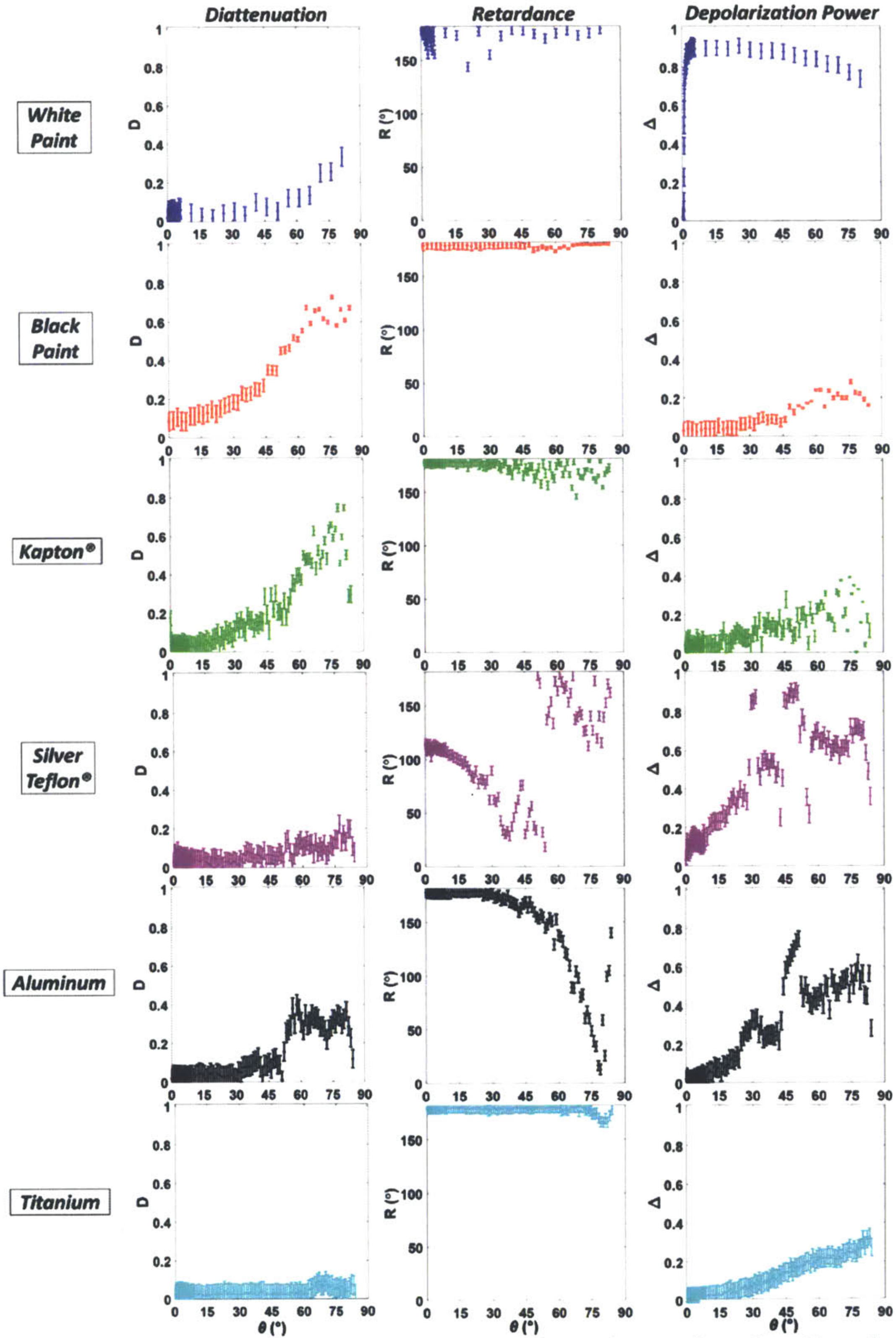

Figure 19: Measured monostatic polarimetric properties with ±3σ error bars from Experiment *A*

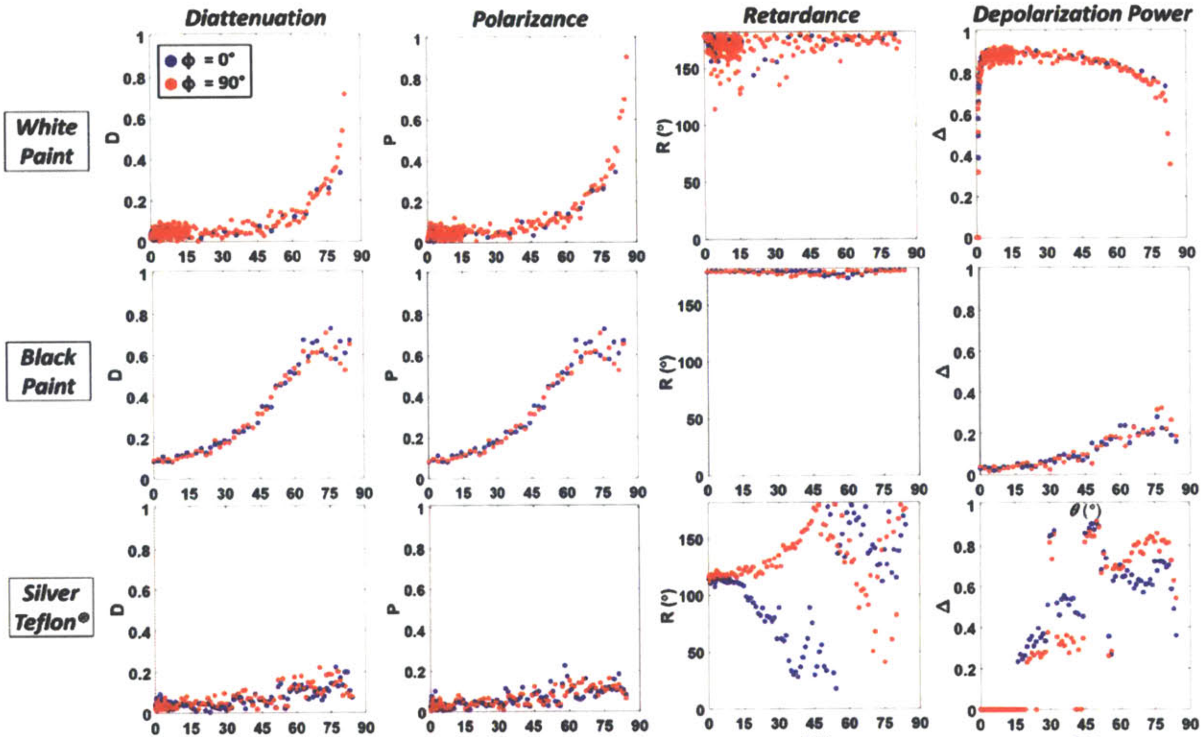

Figure 20: Polarimetric properties of glossy white paint, matte black paint, and silver Teflon® for incident azimuth angles $\phi_i = 0°$ and 90° from Experiment *A*

This page has been intentionally left blank.

4. Experiment *B* - Polarimetric Images

This chapter describes the design, execution, and results of Experiment *B*. The purpose of Experiment *B* is to experimentally determine the polarimetric behavior of objects that are covered or coated in spacecraft materials. Experiment *B* uses a bench-top polarimetric imager with a camera to take polarimetric images of objects, thereby allowing the experimental estimation of its non-resolved polarimetric signature. The results suggest that the signature of a non-resolved object is the weighted sum of the polarimetric behaviors of its constituent material. The measurements performed here constitute a novel exploration of the phenomenology of non-resolved active polarimetry. The results of Experiment *B* are later used to validate the simulation used to explore this phenomenology in more detail.

4.1. Setup and Procedure

The setup for Experiment *B* is a bench-top *polarimetric imager* (diagram in Figure 21; picture in Figure 22). The polarimetric imager is simply an upgraded version of the polarimeter in Experiment *A* (Figure 9). The polarimetric imager only measures objects in a quasi-monostatic geometry, so bistatic imagery is not possible. The monostatic single-pixel detector in Experiment *A* has been replaced with an indium gallium-arsenide (InGaAs) camera (Sensors Unlimited Inc. SU320KVIS-1.7RT) with a bit-depth of 8, i.e., the pixels take on values from 0 to 255. The final upgrade is the insertion of a negative (i.e., diverging lens) to expand the laser beam to illuminate an entire 3D object. The beam has a divergence of < 1°, which should be similar enough to the collimated beam in Experiment *A* for the purposes of this research.

The beam-path and operation of the polarimetric imager is identical to the polarimeter in Experiment *A*. The expanding beam (polarized horizontally) passes through a half-wave ($\lambda/2$) plate and quarter-wave ($\lambda/4$) plate, which are independently rotated to control the polarization state (Tx) of the transmitted beam. The beam then flood-illuminates the object being measured. The reflected light is measured by the camera in a quasi-monostatic geometry, where the laser and camera are separated by < 1°. The camera, just like the detectors in Experiment *A*, is preceded by a $\lambda/4$ plate and $\lambda/2$ plate, which are independently rotated to control the received polarization state (Rx) and a fixed linear polarizer. The fixed linear polarizer ensures that regardless of which Rx is being measured, the camera's pixels are always directly illuminated with the same polarization state, thereby circumventing any unexpected polarization-dependent responsivity.

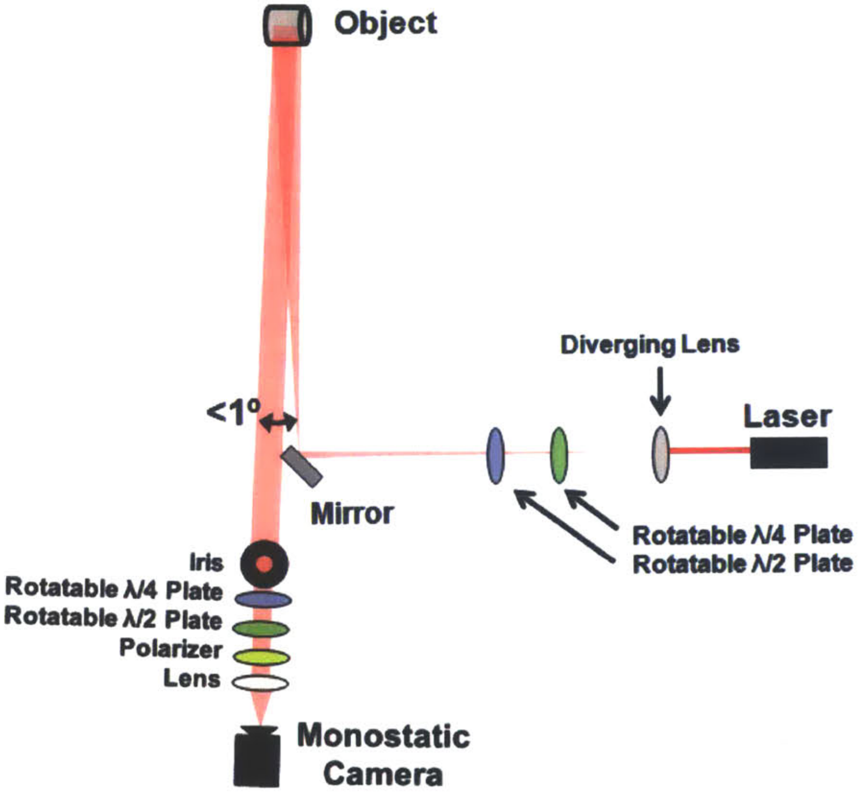

Figure 21: Diagram of bench-top polarimetric imager for Experiment *B*

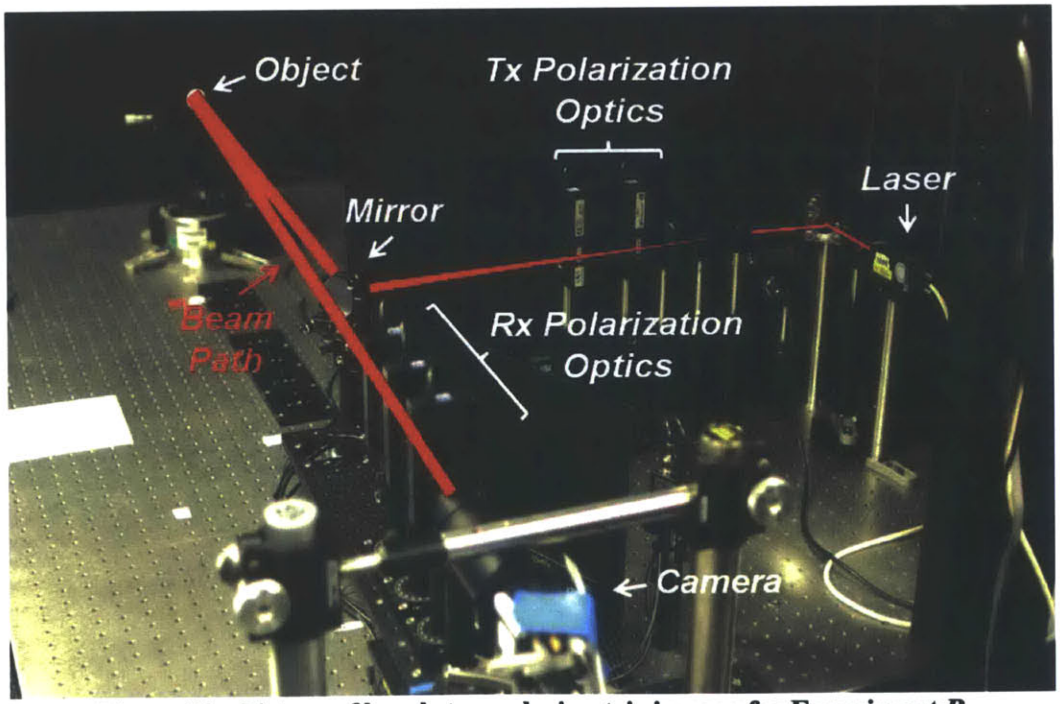

Figure 22: Picture of bench-top polarimetric imager for Experiment *B*

An image A^{TxRx} (256 x 320 matrix) of the illuminated object is taken for each of the 16 polarization pairs TxRx in Table 1. Figure 23 shows a hypothetical set of polarimetric images of an object that are expected to be obtained in Experiment *B*.

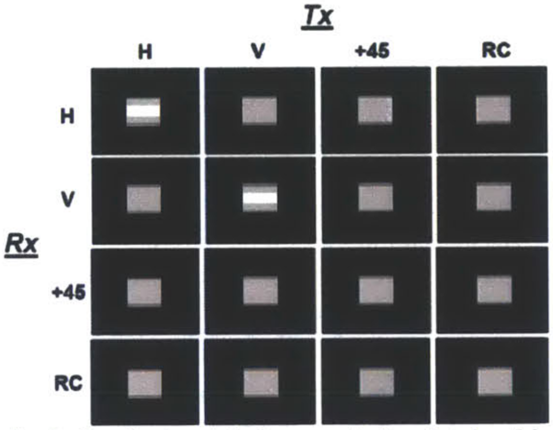

Figure 23: Hypothetical polarimetric images to be obtained in Experiment *B*

Each polarimetric image can be processed to determine what the object would like if it was non-resolved at that polarization pair TxRx. The first step in post-processing is to apply a non-uniformity-correction (NUC) to each raw image A^{TxRx}, which yields a corrected image C^{TxRx}. The process of calculating and applying a NUC is discussed in Section 4.1.1. The next step is to sum over all the pixels encompassing the object (*i,j* ∈ *Object*) to calculate the total intensity I_{TxRx} that would be returned by the object if it was measured with a single-pixel detector:

Eq. 63

$$I_{TxRx} = \sum_{i,j\in Object} C_{ij}^{TxRx}$$

These intensities I_{TxRx} can then be plugged into Eq. 27 to calculate the Mueller matrix and associated polarimetric properties of the non-resolved object.

4.1.1. Non-Uniformity Correction

In order to accurately process the images taken by the polarimetric imager, a non-uniformity correction (NUC) must be performed to account for non-uniformities among the responses of the camera's pixels. The linear response of each pixel (*i,j*) is governed by a unique slope α_{ij} and unique intercept β_{ij}. If pixel (*i,j*) is illuminated with input power C_{ij}, the pixel returns a raw value of A_{ij} as follows:

Eq. 64

$$A_{ij} = \alpha_{ij} C_{ij} + \beta_{ij}$$

Given the raw pixel value A_{ij}, the input power C_{ij} can be solved for as follows:

Eq. 65

$$C_{ij} = \frac{A_{ij} - \beta_{ij}}{\alpha_{ij}}$$

The slope-intercept (α_{ij}-β_{ij}) of each pixel is what constitutes the NUC. Any raw image *A* taken by the camera must be converted to a processed image *C*. This is known as "applying the NUC," so that all pixels are mapped to a uniformly defined value. Determination of the NUC is accomplished by modifying the setup in Figure 21, as shown in Figure 24. The target object is replaced by an integrating sphere, which is a hollow sphere with an internal Lambertian surface. The laser beam enters the sphere through a 4 inch diameter port in front of the sphere. The beam undergoes multiple diffuse reflections inside the sphere before exiting the front port. The result is a flat-field, unpolarized source, such that the front port appears as a uniformly bright circle. The choice of polarization pair TxRx is inconsequential for calculating the NUC.

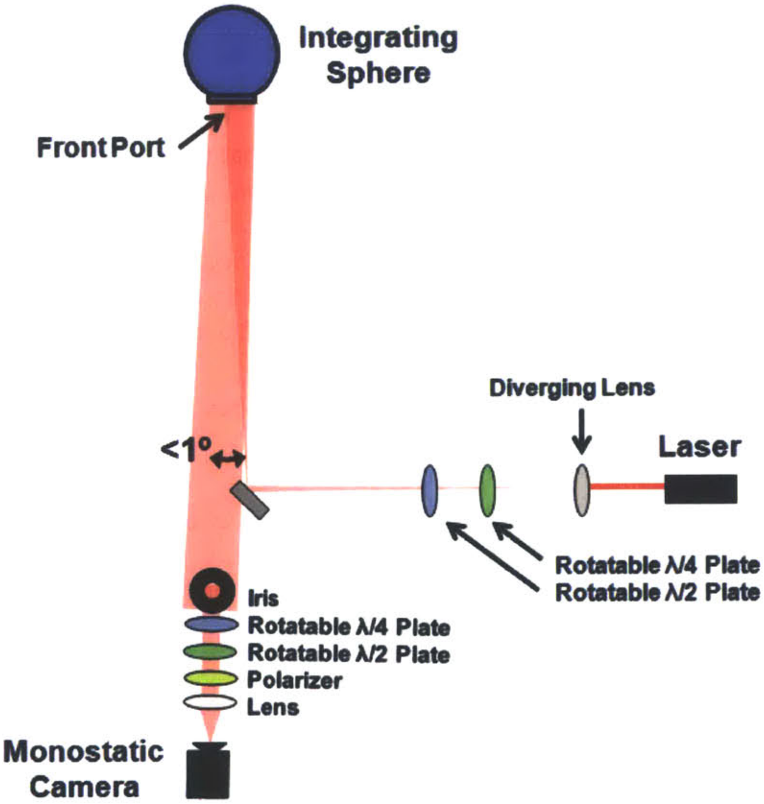

Figure 24: Diagram of setup for determining NUC for Experiment *B*

The procedure for calculating the NUC is as follows. Images A^{Off} and A^{On} of the integrating sphere's front port are taken with the laser OFF and ON, respectively. When the laser is OFF, each pixel sees an input power of $C^{Off} = 0$. When the laser is ON case, each pixel sees an input power of $C^{On} = 1$. These values can be plugged into Eq. 64 for each pixel (*i,j*) to yield:

Eq. 66

$$A_{ij}^{Off} = \beta_{ij}$$
$$A_{ij}^{On} = \alpha_{ij} + \beta_{ij}$$

The slope-intercept (α_{ij}-β_{ij}) of each pixel can be computed as follows:

Eq. 67
$$\begin{aligned}\beta_{ij} &= A_{ij}^{Off} \\ \alpha_{ij} &= A_{ij}^{On} - \beta_{ij} = A_{ij}^{On} - A_{ij}^{Off}\end{aligned}$$

Figure 25 illustrates the process of calculating the NUC for the polarimetric imager's camera. As expected, the image A^{OFF} is very dark. Even though the laser is OFF, each pixel (i,j) takes on a (generally) non-zero value equal to its intercept β_{ij} (according to Eq. 67). The image A^{ON} shows the circular front port of the integrating sphere. As expected, the port appears only roughly uniform due to non-uniformities among the pixels' slopes and intercepts. The right edge of the port is noticeably darker. However, this darkening is actually due to a protruding flange inside the right side of the sphere, rather than true pixel non-uniformities. By design, the objects measured in Experiment *B* all fall within the region outlined by the indicated white rectangle, which avoids the dark edge of the port. Calculation of the NUC [i.e., the slope-intercept (α_{ij}-β_{ij}) using Eq. 67] within the white rectangle should be valid.

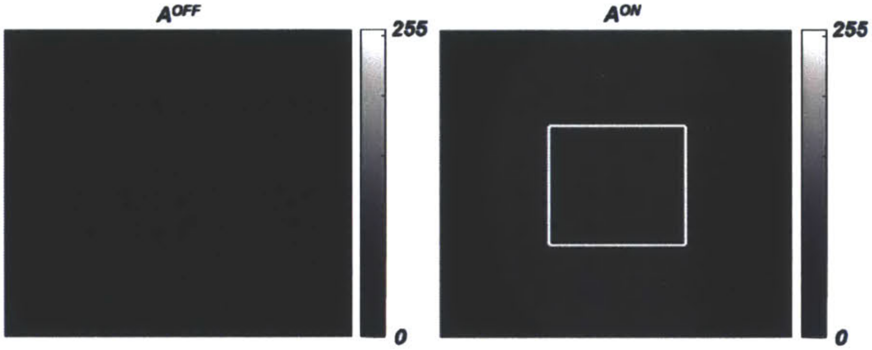

Figure 25: Images taken to determine NUC: laser OFF [left] and laser ON [right]

Figure 26 shows the results of applying the NUC to the region inside the white rectangle. The NUC converts the raw image A^{ON} to the corrected image C^{ON} using Eq. 65. As expected, the corrected image C^{ON} is perfectly uniform with a constant value of 1. The NUC calculated here is applied to every image taken by the polarimetric imager in Experiment *B*.

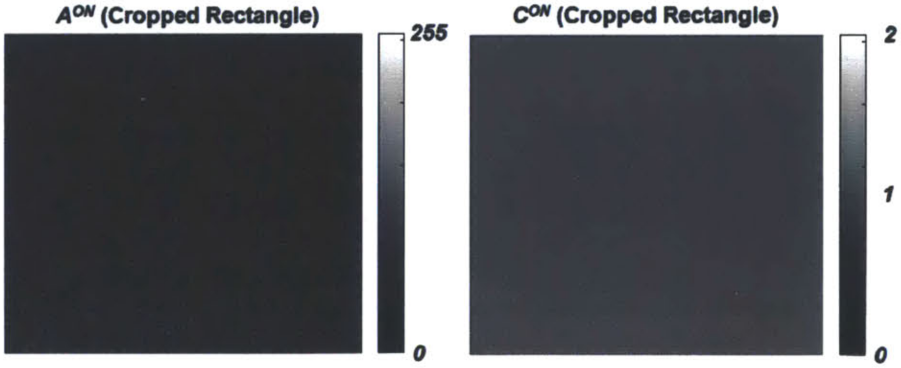

Figure 26: NUC result: raw A^{ON} [left]; corrected C^{ON} [right]

4.2. Validation

The polarimetric imager (Figure 21) in Experiment *B* was validated in terms of its ability to measure a reference sample with known MRDFs. It may seem counterintuitive to measure an MRDF with a camera, but this was made possible through modifications to the setup in Figure 21 and some specialized post-processing. To measure the MRDF of a material using the polarimetric imager, the object in Figure 21 is replaced with a "coupon" sample, as in Experiment *A*. During a monostatic scan, the sample is rotated to scan over various incident/scatter zenith angle $\theta = \theta_i = \theta_s$. At each angle θ, an image $A^{TxRx}(\theta)$ of the diverged laser beam is taken for a given polarization pair TxRx. The first step in post-processing is to apply the NUC to each raw image A^{TxRx}, which yields a corrected image C^{TxRx}. The next step is to sum over all the pixels encompassing a fixed region of the beam ($i,j \in Region$) to calculate the total intensity I_{TxRx}:

Eq. 68

$$I_{TxRx} = \sum_{i,j \in Beam} C_{ij}^{TxRx}$$

This intensity can be plugged into Eq. 42, repeated here, to calculate the MRDF:

Eq. 69

$$MRDF(\theta, Tx, Rx) = \frac{I_{TxRx}}{I_0 \Omega \cos\theta}$$

The solid angle Ω can be computed using Eq. 43, just as in Experiment *A*. However, it is not possible to directly measure the effective incident beam intensity I_0. Instead, I_0 must be determined indirectly by measuring a known reference sample and inferring the value of I_0. This was accomplished with the polarimetric imager by performing a monostatic scan of a sample of Spectraflect® at polarization HH and HV. Figure 27 shows the raw images A^{HH} of the sample at polarization HH and incident angles θ = 10°, 30°, 45°, and 60°. As expected for a Lambertian surface, the beam gets dimmer at higher incident angles. In kind, the corrected images C^{HH} also followed this trend. In calculating the total intensity I_{TxRx} returned by the sample, only the region outlined by the white rectangle was used in the summation in Eq. 68 (after applying the NUC). Some of the pixels, colored in red, were excluded from the calculation because they were saturated (i.e., had a value of 255) for at least one incident angle. Since the surface of the Spectraflect® sample exhibits the same behavior at all pixels, exclusion of these saturated pixels does not affect the result.

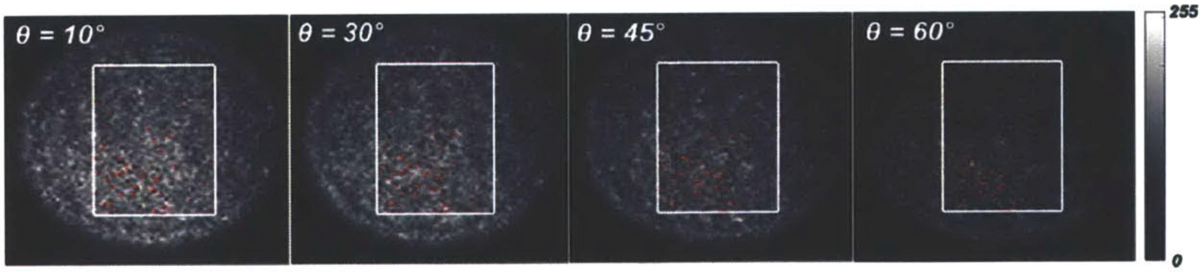

Figure 27: Raw polarimetric monostatic images A^{HH} of a laser beam illuminating a Spectraflect® sample at incident angles θ = 0°, 30°, 45°, and 60°

The intensities $I_{HH}(\theta)$ were calculated using Eq. 68 at $\theta = 10$, 30, 45, and 60°. This was repeated at polarization HV. Meanwhile, as introduced in the validation of Experiment *A* (Section 3.2), the manufacturer (Labsphere®) provided reference MRDFs values, i.e., $\mathrm{MRDF}_{\mathrm{ref}}(\theta)$, for Spectraflect® at polarization HU and $\theta = 10°$, 30°, 45°, and 60°. Following Pickering's method [93], the sum of the measured MRDFs at HH and HV should be equivalent to the reference data at HU. Setting Eq. 69 equal to the reference value $\mathrm{MRDF}_{\mathrm{ref}}(\theta)$ at angle θ, the incident power I_0 can be inferred using the following equation:

Eq. 70
$$I_0 = \frac{I_{TxRx}(\theta) + I_{TxRx}(\theta)}{MRDF_{ref}(\theta)\Omega\cos\theta}$$

The incident beam intensity I_0 should be constant for all angles θ. Consequently, a sufficient value for I_0 was found by averaging the results of Eq. 70 for $\theta = 10°$, 30°, 45°, and 60°. Having indirectly determined the value of I_0, it was possible to calculate the MRDF of Spectraflect® at HH and HV (and HU by summation) using Eq. 69. Figure 28 shows that the measured MRDF matches the reference data within ±5% of the reference values. This result validates the polarimetric imager's ability to accurately measure MRDF curves. Of course, in Experiment *B*, the polarimetric imager is not used to measure polarimetric MRDFs, but rather polarimetric images of objects. Nevertheless, this was a useful radiometric validation.

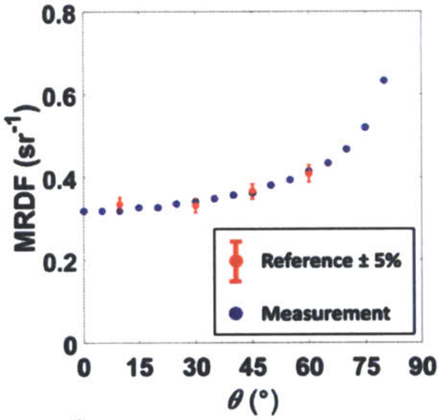

Figure 28: MRDF of Spectraflect® at polarizaton HU (measurement vs. reference) using the polarimetric imager from Experiment *B*

4.3. Measurement of Objects

Upon validation, the bench-top polarimetric imager was used to measure monostatic polarimetric images of objects (Figure 29) covered or coated in the spacecraft materials from Experiment *A*, including:

- **Cylinder Painted White**: an aluminum cylinder painted with glossy white paint (i.e., Aeroglaze® A276)
- **Sphere Painted White**: an aluminum sphere painted with glossy white paint

- **Cylinder Wrapped with silver Teflon®**: an aluminum cylinder wrapped in silver Teflon®, such that the silver Teflon® presents an azimuth angle of $\phi_i = 0°$ to the camera when the cylinder lies on its side (as in Figure 29).

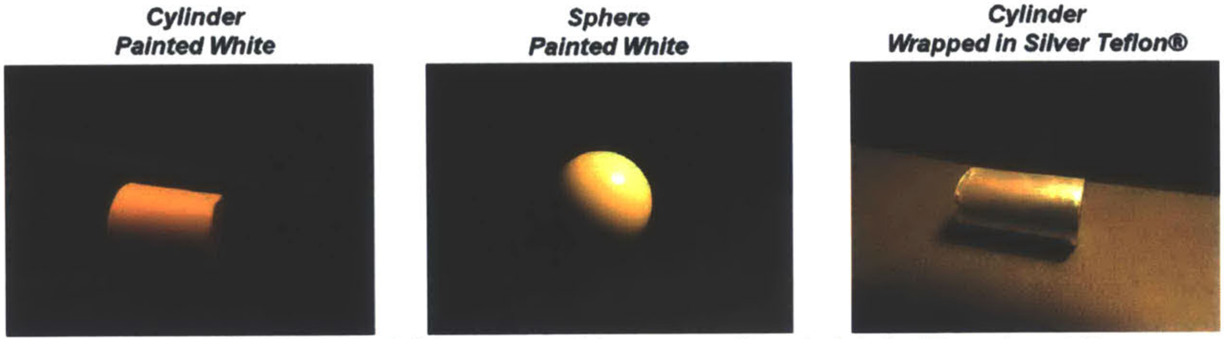

Figure 29: Pictures of objects covered in spacecraft materials for Experiment *B*

The objects were inserted as targets for the polarimetric imager, as depicted in Figure 30, in which the direction of the incident laser is represented by a red arrow. The two cylinders were mounted at 2° from a broadside orientation to avoid saturation by the specular reflection that would occur at 0°. Meanwhile, the white sphere could only be mounted in one unique way. Due to subtle imperfections in the coating, saturation did not occur appreciably around the sphere's expected specular reflection.

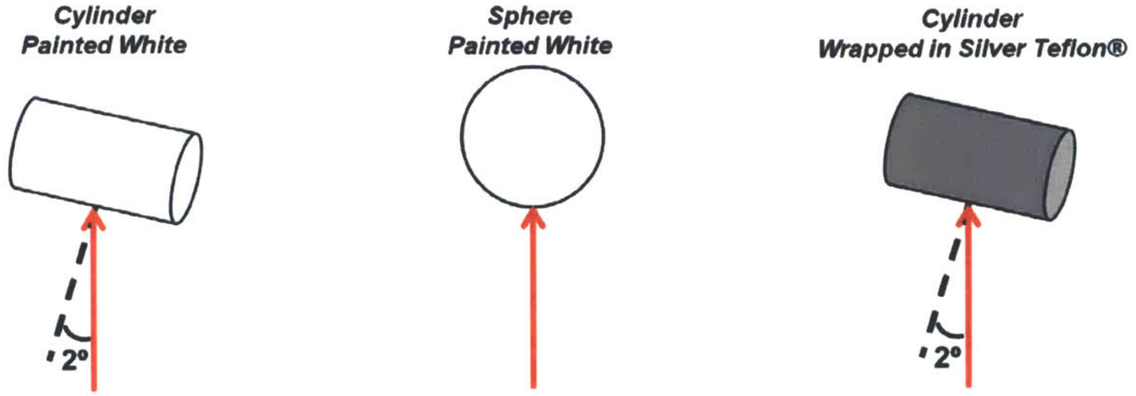

Figure 30: Orientation of objects for Experiment *B*

4.4. Results and Analysis

This section presents the results of Experiment *B* for the objects introduced above.

4.4.1. Polarimetric Images

Considered first are the monostatic polarimetric images of each object at the 16 polarization pairs from Table 1. Figure 31, Figure 32, and Figure 33 show the 16 raw polarimetric images (i.e., before applying the NUC) of the white cylinder, white sphere, and silver Teflon® cylinder, respectively. The bright circle (or halo) appearing around each object is the result of the laser beam reflecting off a mounting apparatus in the background. A darker or more streamlined mount would be advisable in future work. Some of the pixels have also been colored red, indicating that they were saturated for at least one of the polarization 16 pairs. Since only 0.002% of all object pixels (and only 0.008% of the specular stripe of the cylinders) is saturated, exclusion of these pixels should have a negligible effect on the calculation of polarimetric properties.

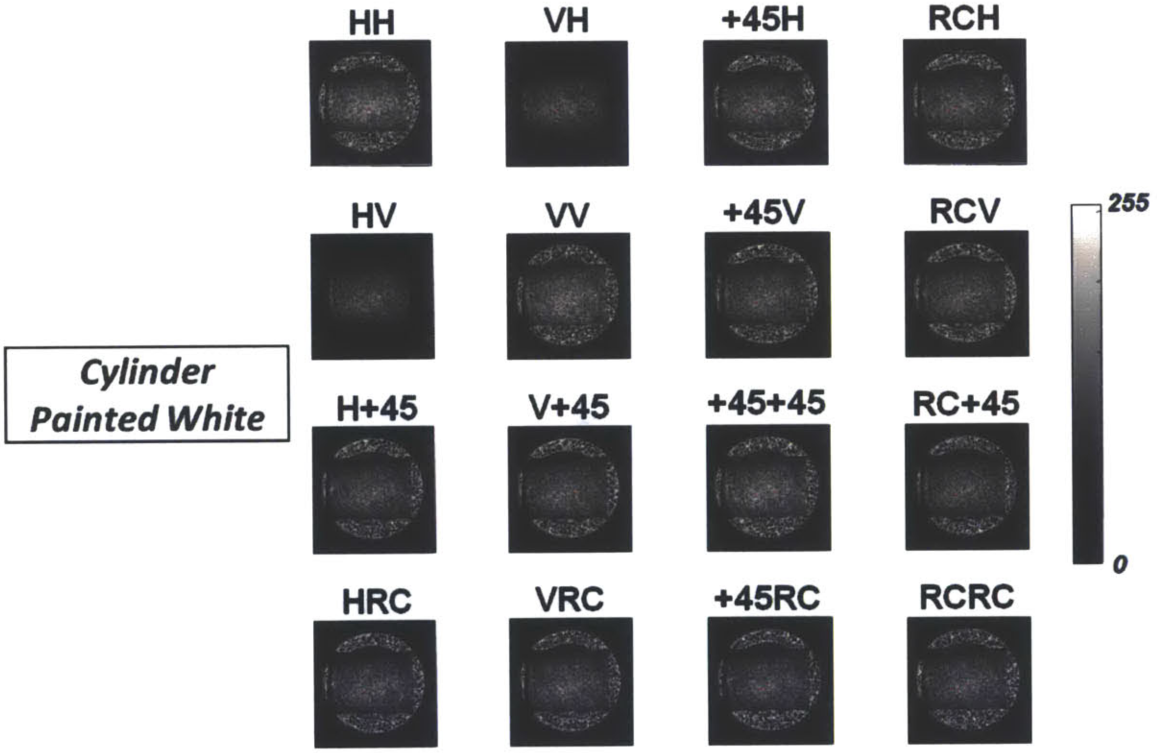

Figure 31: Measured polarimetric images of a cylinder painted with glossy white paint

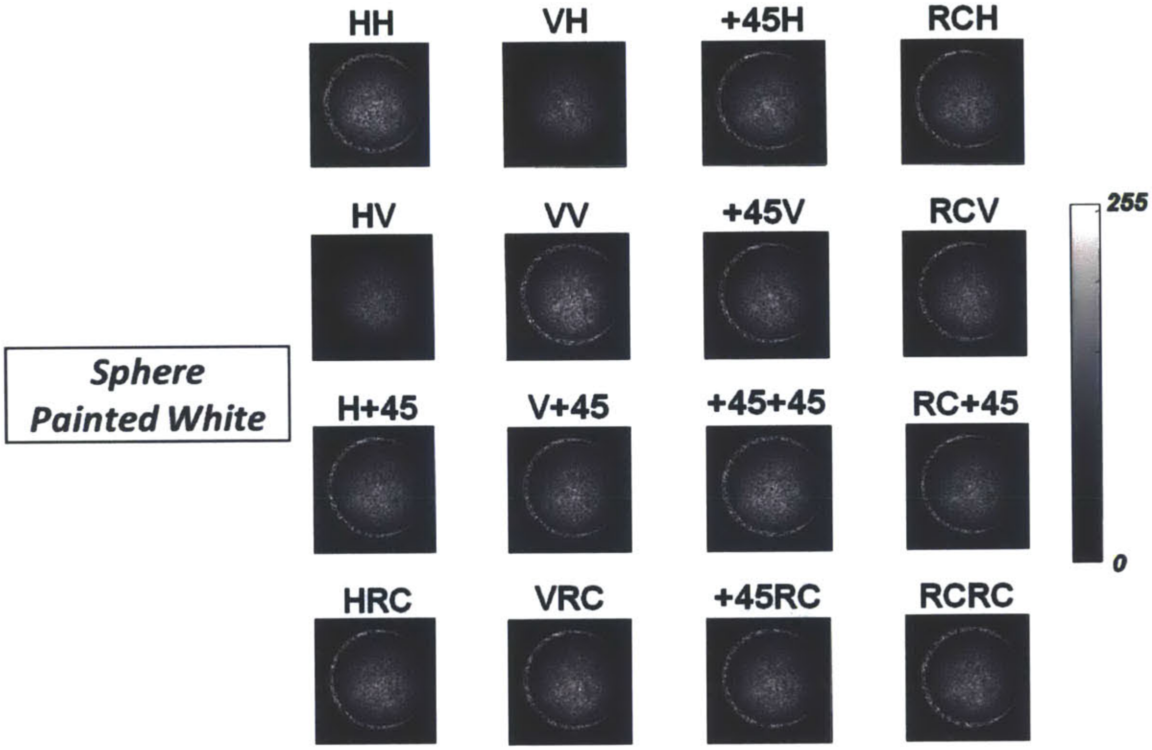

Figure 32: Measured polarimetric images of a sphere painted with glossy white paint

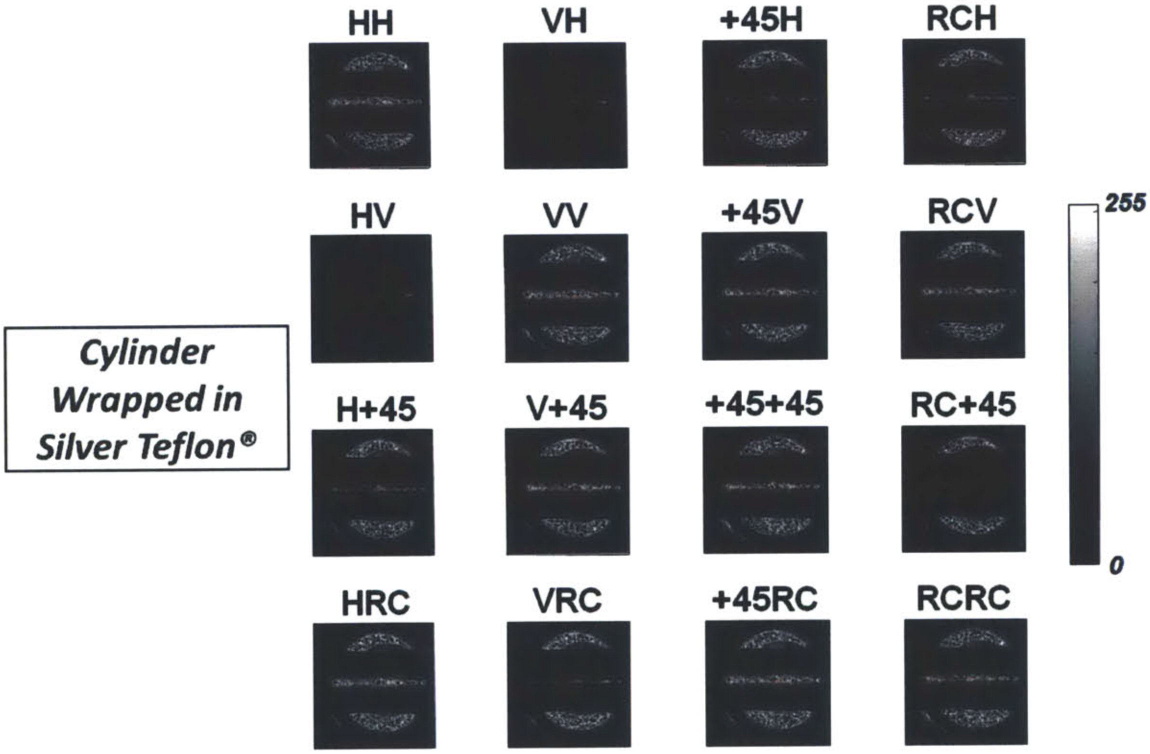

Figure 33: Measured polarimetric images of a cylinder wrapped in silver Teflon® at $\phi_i = 0$

A few observations in these polarimetric images are worth noting. As intended to avoid saturation, the white cylinder (Figure 31) does not exhibit a specular stripe along its length because it is oriented 2° away from broadside. By contrast, the cylinder wrapped in silver Teflon® (Figure 33) still exhibits a bright stripe along its length, even though it was also oriented 2° away from broadside. This occurs because silver Teflon® has a brighter and wider monostatic specular lobe than glossy white paint (Figure 15), such that a bright reflection still occurs at 2° from normal incidence. Even so, the bright stripe does not cause saturation. Finally, the white sphere (Figure 32) exhibits a bright spot around its center, but saturation does not occur appreciably.

4.4.2. Polarimetric Signatures of Objects

The polarimetric images were used to experimentally determine the non-resolved polarimetric signature of each object, in terms of its Mueller matrix and polarimetric properties. First, the NUC was applied to each image using Eq. 65. The pixels comp each object were then defined as in Figure 34. Summing over these pixels for each polarimetric image, Eq. 63 was used to calculate the total intensity I_{TxRx} that would be returned by each object when measured with a single-pixel detector for polarization pair TxRx.

Figure 34: Regions of pixels encompassing each object

The intensities I_{TxRx} were then plugged into Eq. 27 to calculate the Mueller matrix of each object, as if it was non-resolved. Table 7 lists the polarimetric properties computed from these Mueller matrices.

Table 7: Experimentally determined polarimetric properties of non-resolved objects

Object	D	R	Δ
Cylinder Painted White	0.03	179°	0.91
Sphere Painted White	0.01	171°	0.92
Cylinder Wrapped in Silver Teflon®	0.04	115°	0.64

The Mueller matrix and polarimetric signature of each object can be explained as follows:

- **Cylinder Painted White**: The polarimetric properties of the white cylinder are D = 0.03, R = 179°, and Δ = 0.91, which generally match the monostatic polarimetric properties of glossy white paint in the diffuse region, as measured in Experiment *A* (Figure 18). This relationship makes sense since the white cylinder is purposely oriented 2° away from broadside to prevent the specular reflection from saturating the camera, which means the camera only receives diffuse backscatter from every portion of the cylinder's surface.

- **Sphere Painted White**: The polarimetric signature of the non-resolved white sphere is similar to that of the white cylinder. The properties are D = 0.01, R = 171°, and Δ = 0.92, which generally match the monostatic polarimetric properties of glossy white paint in the diffuse region, as measured in Experiment *A* (Figure 18). This relationship makes sense. Although the sphere returns a small amount of specular reflection, the vast majority of the sphere's facets returns diffuse backscatter. Consequently, the white sphere's non-resolved signature is dominated by the diffuse behavior of glossy white paint.

- **Cylinder Wrapped in silver Teflon®**: The polarimetric properties of the silver Teflon® cylinder are D = 0.04, R = 115°, and Δ = 0.64. This outcome is explained by the monostatic properties of silver Teflon® (Figure 18). In Experiment *A*, silver Teflon® exhibited practically no diattenuation at all angles, which agrees with the cylinder's value of D = 0.04 here. An explanation of the cylinder's retardance and depolarization power is more complex. The cylinder is purposely oriented 2° away from broadside to prevent the specular reflection from saturating the camera, but a bright stripe still appears along its length. In Experiment *A*, silver Teflon® exhibited a peculiar retardance of R = 115° in the specular region, but the full range of retardances (R = 0 - 180°) in the diffuse region. The cylinder's retardance of R = 115° appears to be dominated by the retardance of its bright (i.e., specular) stripe. Apparently, the specular contribution is not perturbed by the range of retardances (R = 0 to 180°) contributed by diffuse reflections from the rest of the cylinder's body, perhaps because R = 115° lies near the middle of that range. Similar reasoning can be applied to the cylinder's depolarization power. In Experiment *A*, silver Teflon® exhibited a depolarization power of Δ = 0 around the specular, but a range of depolarization powers (Δ = 0 to 0.8) in the diffuse region. The cylinder's depolarization power of Δ = 0.65 appears to be some weighted average of the specular and diffuse contributions.

These results suggest that an object's non-resolved signature will be a weighted sum of the constituent material's geometry-dependent polarimetric behaviors. In the cases of the white cylinder and sphere, the signature is dominated by the diffuse behavior of glossy white paint. By contrast, the signature of the silver Teflon® cylinder is a less discernible, but still reconcilable, combination of the specular and diffuse behavior of silver Teflon®. The nuances of non-resolved object signatures are explored further by the simulations in Chapter 5.

The results also demonstrate the potential ability of active polarimetry to discriminate between objects composed of different materials. The two objects that were painted white, i.e., the cylinder and sphere, have identical polarimetric properties ($D \approx 0$, $R \approx 180°$, $\Delta = 0.9$), owing to the diffuse behavior of glossy white paint. The robustness of this signature for different object orientations is investigated further by the simulations in Chapter 5. Meanwhile, the cylinder paint white and the cylinder wrapped in silver Teflon® have identical diattenuation ($D \approx 0$) and high depolarization power ($\Delta = 0.91$ and 0.64, respectively), but distinct retardances of $R = 179°$ and 115°, respectively. Considering that the error bounds on estimated retardances were only $3\sigma_R = 13°$ in Experiment *A*, it may be expected that objects covered with silver Teflon® would be readily distinguishable from objects covered in white paint (and most other materials with mirror-like retardance of $R = 180°$) based on the observed retardance. The robustness of this distinction will be investigated further by the simulations in Chapter 5.

4.5. Summary of Experiment B

Experiment *B* measured polarimetric images of objects covered in spacecraft materials. The images were carefully processed to determine the polarimetric signature of the objects, as if they were non-resolved. The results made sense in light of the polarimetric BRDFs and properties measured in Experiment *A*. The polarimetric signature of a non-resolved object appears to be a weighted sum of the geometry-dependent polarimetric behavior of the object's constituent material.

Experiment *B* was an empirical investigation of the phenomenology of non-resolved active polarimetry. In theory, one could use the polarimetric imager from Experiment *B* to measure objects of any arbitrary shape and orientation. However, it would be more efficient to simulate these object signatures in software, rather than measure and process them. As discussed in Chapter 5, a simulation was developed to meet this need. The results of Experiment *B* were used to validate the simulation before using it to investigate the phenomenology of non-resolved active polarimetry in more detail.

This page has been intentionally left blank

5. Modeling and Simulation

This chapter describes the modeling and simulation that was developed to predict the polarimetric signatures of non-resolved objects. The simulation ingests the polarimetric MRDFs of a material (at a wavelength of λ = 1064 nm) and then geometrically determines the polarimetric signature of a non-resolved object covered in that material. The approach here is similar to others in the literature [98, 99] for modeling the spectral signatures of objects from known spectral BRDFs. The simulation was validated against the results of Experiment *B* for the white-painted sphere and two cylinders (white paint and silver Teflon®). Simulations were then run to explore the signatures of non-resolved objects for a variety of engagement scenarios, including monostatic measurements of stationary and tumbling objects of different shapes and dimensions, as well as bistatic measurements of objects with specular reflections. The results demonstrate that the phenomenology of non-resolve active polarimetric is quite rich. The polarimetric properties of a non-resolved object can be described as the weighted sum of the geometry-dependent polarimetric behaviors of its facets. The resulting signature is ultimately a complex function of the object shape, orientation, constituent material, and tumbling behavior.

5.1. Setup and Procedure

The simulation determines the monostatic polarimetric signature of a non-resolved, stationary object as follows. The modeling of tumbling objects is discussed in Section 5.1.1. It is assumed that an object is uniformly flood-illuminated by a collimated laser beam of polarization state Tx and a monostatic detector then measures the reflected light with polarization state Rx. The object (e.g., the cylinder in Figure 35) can be modeled as a set of triangular facets.

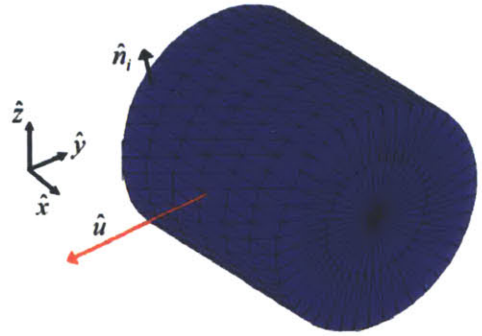

Figure 35: Surface model of cylinder

Each triangular facet n is described by its material type, area A_n, and unit surface normal $\hat{s}_n(y,p,r)$, the latter of which is a function of the object's yaw (y), pitch (p), and roll (r) :

Eq. 71
$$\hat{s}_n(y,p,r) = \mathfrak{R}_1(r)\mathfrak{R}_2(p)\mathfrak{R}_3(y)\hat{s}_n(0,0,0)$$

where $\hat{s}_n(0,0,0)$ is the surface normal of facet n when $y = p = r = 0$, and $\mathfrak{R}_1$, $\mathfrak{R}_2$, and $\mathfrak{R}_3$ are rotation matrices defined conventionally as:

Eq. 72
$$\Re_1(r)=\begin{bmatrix}1 & 0 & 0\\ 0 & \cos r & -\sin r\\ 0 & \sin r & \cos r\end{bmatrix}$$

Eq. 73
$$\Re_2(y)=\begin{bmatrix}\cos p & 0 & \sin p\\ 0 & 1 & 0\\ -\sin p & 0 & \cos p\end{bmatrix}$$

Eq. 74
$$\Re_3(y)=\begin{bmatrix}\cos y & -\sin y & 0\\ \sin y & \cos y & 0\\ 0 & 0 & 1\end{bmatrix}$$

For the remainder of this derivation, $\hat{s}_n(y,p,r)$ will be concisely written as $\hat{s}_n$, where the dependence on object's yaw, pitch, and roll is implied. If the co-located laser and detector are located along unit direction $\hat{u}$, then the incident zenith angle θ_n (also equal to the scatter zenith angle) presented by facet n is:

Eq. 75
$$\theta_n=\cos^{-1}(\hat{u}\bullet\hat{s}_n)$$

where • denotes the dot product. Additionally, the angle α_n between the horizontal, or xy, plane and the plane of incidence (i.e., the plane containing $\hat{u}$ and $\hat{s}_n$) for facet n is given by:

Eq. 76
$$\alpha_n=\cos^{-1}[\hat{z}\bullet(\hat{u}\times\hat{s}_n)]$$

Given the measured polarimetric MRDFs of the facet's material type, the material's monostatic Mueller matrix $M(\theta_n)$ can be calculated from Eq. 30. Since the measured $M(\theta_n)$ assumes the plane of incidence is horizontal (i.e., according to the geometry of the bench-top polarimeter in Figure 9), the matrix $M(\theta_n)$ must be rotated by the angle α_n to determine the effective Mueller matrix M_n of facet n:

Eq. 77
$$M_n=\Re_{4x4}(-\alpha_n)M(\theta_n)\Re_{4x4}(\alpha_n)$$

where $\Re_{4x4}$ is the 4 x 4 rotation matrix [15] given by:

Eq. 78
$$\Re_{4x4}(\alpha)=\begin{bmatrix}1 & 0 & 0 & 0\\ 0 & \cos 2\alpha & \sin 2\alpha & 0\\ 0 & -\sin 2\alpha & \cos 2\alpha & 0\\ 0 & 0 & 0 & 1\end{bmatrix}$$

Given M_n, the polarimetric MRDF value $MRDF_n^{TxRx}$ (in sr^{-1}) of facet n can be calculated similarly to Eq. 26:

Eq. 79 $$MRDF_n^{TxRx} = M_{row0}^{Rx} M_n \vec{S}^{Tx}$$

Accounting for a viewing factor $\cos(\theta_n)$ and the projected area $A_n^{proj} = A_n\cos(\theta_n)$ (along the direction $\hat{u}$, of the laser/detector), the laser radar cross section $LRCS_n^{TxRx}$ of facet *n* for polarization pair TxRx is:

Eq. 80 $$LRCS_n^{TxRx} = MRDF_n^{TxRx} \cos\theta_n A_n^{proj}$$

The cross section $LRCS_{obj}^{TxRx}$ of the entire object for polarization pair TxRx is the sum of the $LRCS_n^{TxRx}$ values of all *N* forward-facing facets (i.e., $\theta_n < 90°$):

Eq. 81 $$LRCS_{obj}^{TxRx} = \sum_{n=1}^{N} LRCS_n^{TxRx}$$

The object is assumed to be non-resolved, such that the reflected light from every facet is collected by a single-pixel detector. Given non-resolved measurements for 16 sufficient TxRx pairs (Table 1), the Mueller matrix $\vec{M}_{obj}$ (in vector form) of the entire object can be estimated from Eq. 23, rewritten here:

Eq. 82 $$\vec{M}_{obj} = H^{-1}\vec{I}$$

where the intensity vector $\vec{I}$ is composed of the measured $LRCS_{obj}^{TxRx}$ values (Eq. 39):

Eq. 83 $$\vec{I} = \begin{bmatrix} I_{Tx^1Rx^1} \\ I_{Tx^2Rx^2} \\ \cdots \\ I_{Tx^{16}Rx^{16}} \end{bmatrix} = \begin{bmatrix} LRCS_{obj}^{Tx^1Rx^1} \\ LRCS_{obj}^{Tx^2Rx^2} \\ \cdots \\ LRCS_{obj}^{Tx^{16}Rx^{16}} \end{bmatrix}$$

The object's estimated Mueller matrix can then be filtered and decomposed to calculate its polarimetric properties. In summary, the simulation developed in this research executes Eq. 75 through Eq. 83 to predict the monostatic polarimetric signature of a non-resolved object, given the measured polarimetric MRDF of the object's constituent materials measured in Experiment *A*. The simulation was implemented in Matlab®.

5.1.1. Tumbling Objects

The simulation nominally performs the steps outlined above to predict the signature of a *stationary* object. However, space surveillance targets will obviously not be stationary, either in position or rotation. In fact, space debris fragments can have tumbling rates from 0.1s to 10s of degrees per second [20, 29]. The polarimetric signature of a tumbling object is complicated because the object rotates by some amount in between serial polarization measurements. The effect of tumbling will depend on how the tumbling rate compares to the measurement rate. If all the polarization measurements can be completed quickly relative to the tumbling rate, the effect of tumbling may be negligible compared to the stationary case. However, as the tumbling rate increases, the polarization measurements will become increasingly disconnected, and the signature may become blurred.

In theory, the simulation here could be augmented to evaluate an object with arbitrary tumbling behavior by appropriately rotating the object in between simulating each polarization measurement. Such fidelity was beyond the scope of this research and is recommended for future work. However, as derived below, the case of a fast tumbling object (relative to the measurement rate) is actually simple enough to evaluate without any changes to the current simulation. For instance, consider an object that is tumbling fast about the yaw axis, while its pitch and roll are fixed at $p = r = 0$. A large number of intensity measurements are made for each polarization pair TxRx. For each measurement, the object is effectively oriented at a random yaw angle y. The effective intensity vector $\vec{I}_{yawing}$ for this situation is found by averaging over the continuous range of yaw angles (y = -180 to 180°):

Eq. 84

$$\vec{I}_{yawing} = \frac{1}{360}\begin{bmatrix} \int_{-180}^{+180} LRCS_{obj}^{Tx^1Rx^1}\,dy \\ \int_{-180}^{+180} LRCS_{obj}^{Tx^2Rx^2}\,dy \\ \cdots \\ \int_{-180}^{+180} LRCS_{obj}^{Tx^{16}Rx^{16}}\,dy \end{bmatrix} = \frac{1}{360}\int_{-180}^{+180}\begin{bmatrix} LRCS_{obj}^{Tx^1Rx^1} \\ LRCS_{obj}^{Tx^2Rx^2} \\ \cdots \\ LRCS_{obj}^{Tx^{16}Rx^{16}} \end{bmatrix} dy$$

Plugging Eq. 84 into Eq. 24, the Mueller matrix $\vec{M}_{yawing}$ for a quickly yawing object becomes:

Eq. 85

$$\vec{M}_{yawing} = H^{-1}\vec{I}_{yawing} = \frac{1}{360}\int_{-180}^{+180} H^{-1}\begin{bmatrix} LRCS_{obj}^{Tx^1Rx^1} \\ LRCS_{obj}^{Tx^2Rx^2} \\ \cdots \\ LRCS_{obj}^{Tx^{16}Rx^{16}} \end{bmatrix} dy = \frac{1}{360}\int_{-180}^{+180}\vec{M}_{obj}\,dy$$

Eq. 85 states that the Mueller matrix of a fast yawing object is simply the average Mueller matrix of a stationary object, where the average is taken over all yaw angles. Therefore, one can determine the signature of a fast yawing object by simulating stationary objects over the full range of yaw angles (at some resolution) and averaging the resulting Mueller matrices. Similar but more complex relationships surely exist for other fast tumbling behaviors, whether about a single rotation axis or multiple axes (e.g., a precession or nutation).

By contrast, a slowly tumbling object will have a signature unlike the stationary case or the fast tumbling case. In a medium-speed tumbling case, all the polarization measurements may be completed before the object completes one period of rotation. Consequently, the polarization measurements will be disconnected in a complex way that cannot be captured by an integral over all orientations. Instead, the simulation would have to be augmented to rotate the target incrementally as each polarization measurement is taken. In the simulations to follow, only stationary and fast tumbling objects are considered using the relationships derived above.

5.1.2. Limitations

The simulation has a few limitations besides the inability to handle arbitrarily tumbling objects. First, the simulation currently only allows objects with convex outer hulls, meaning any line connecting two points on the outer hull must be completely contained within the object. In other words, an object cannot have dimples, flanges, or any extensions creating a concavity. In future work, concave objects could be modeled by accounting for multiple reflections, shadowing, and other effects.

Another limitation is that the simulation can only predict signatures of objects measured in a monostatic geometry. The simulation of bistatic measurements requires consideration of out-of-plane reflections, i.e., light reflecting out of the plane of incidence of each facet. Since out-of-plane (bistatic) BRDFs were not measured in Experiment *A*, the simulation of bistatic signatures was not possible here. In future work, the simulation could be augmented to ingest in-plane and out-of-plane bistatic BRDF data (measured or modeled) to predict the bistatic polarimetric signatures of non-resolved objects. Nevertheless, the current simulation can still handle the degenerate case in which an object's bistatic signature is dominated by a specular reflection, since Experiment *A* did measure bistatic specular reflections at several incident angles ($\theta_i = 15°$, 30°, 45°, 60°, 75°). In the analysis to follow, the exploitation of bistatic specular reflection is explored in more detail.

One last limitation is related to the issue of *anisotropy*. As demonstrated in Experiment *A* (Section 3.4.6), a material can exhibit anisotropy, such that its polarimetric properties depend on the incident azimuth angle ϕ_i. For example, it was demonstrated that silver Teflon® has an anisotropic retardance, while glossy white paint and matte black paint were isotropic. In the current simulation, it is not possible to specify the azimuthal orientation ϕ of the material covering each facet. For isotropic materials, this shortcoming does not matter. Anisotropic materials, on the other hand, require this additional fidelity. However, this is inconsequential here since Experiment *A* did not rigorously measure azimuthal dependencies. In future work, the simulation could be augmented to specify the azimuth of each facet and ingest MRDFs (or BRDFs) measured at those azimuths. In Section 5.3, the complication of anisotropy is avoided by only considering isotropic materials (e.g., glossy white and matte black paint) or objects and orientations in which every facet presents the same azimuth angle (e.g., a broadside cylinder).

5.2. Validation

The simulation was validated against the results of Experiment *B* (Chapter 4). Experiment *B* measured three objects, specifically a cylinder painted white (oriented at 2° away from broadside), a sphere painted white, and a cylinder wrapped in silver Teflon® (also oriented at 2° away from broadside), and determined their polarimetric signatures, as if they were non-resolved. For comparison, the simulation was run to predict the signatures of these three objects (oriented identically to Experiment *B*), given the polarimetric BRDFs of the materials measured in Experiment *A*. Since glossy white paint is isotropic, the simulation can handle any arbitrarily shaped (or oriented) object that is painted white. Meanwhile, silver Teflon® is anisotropic, which means the simulation can only handle Teflon® objects whose facets all share the same incident azimuth angle, e.g., a broadside cylinder. The cylinder oriented 2° away from broadside does not meet this criteria, as all the surface facets do not present exactly the same azimuth angle. However, this detail will be temporarily ignored for the purpose of comparing the simulation to Experiment *B*. For greatest accuracy, the simulation was fed the polarimetric MRDFs of silver Teflon® at $\phi_i = 0°$ (from Experiment *A*) to match the azimuth angle used in Experiment *B*. Table 8 compares the polarimetric properties measured in Experiment *B* with the properties predicted from simulation, including diattenuation (*D*), retardance (*R*), and depolarization power (Δ). For each object, the simulated and experimental properties match within error bounds of $6\sigma_D = 0.10$, $6\sigma_R = 10°$, and $6\sigma_\Delta = 0.10$, accounting for 3σ from Experiment *A* (Section 3.4.5) (whose measured BRDFs were fed to the simulation) and 3σ from Experiment *B* (approximated to be the same as in Experiment *B*). These results validate the accuracy of the simulation relative to Experiment *B*.

Table 8: Polarimetric properties of non-resolved objects (Experiment *B* vs. Simulation)

Object	Orientation	*D*		*R*		Δ	
		Exp. B	Sim	Exp. B	Sim	Exp. B	Sim
Cylinder Painted White	2° from broadside	0.03	0.04	179°	176°	0.91	0.89
Sphere Painted White	n/a	0.01	0.04	171°	178°	0.92	0.88
Cylinder Wrapped in Silver Teflon®	2° from broadside	0.03	0.03	115°	107°	0.64	0.58

To further illustrate the validation visually, Figure 36 shows the polarimetric images measured in Experiment *B* (from Figure 33) side-by-side with the polarimetric images generated in simulation, for the cylinder wrapped in silver Teflon®. Visually speaking, the experimental and simulated images show the same relative brightness as a function of the polarization pair TxRx. The simulated images are obviously missing the circular mounting apparatus found in the experimental images, which is inconsequential to this comparison.

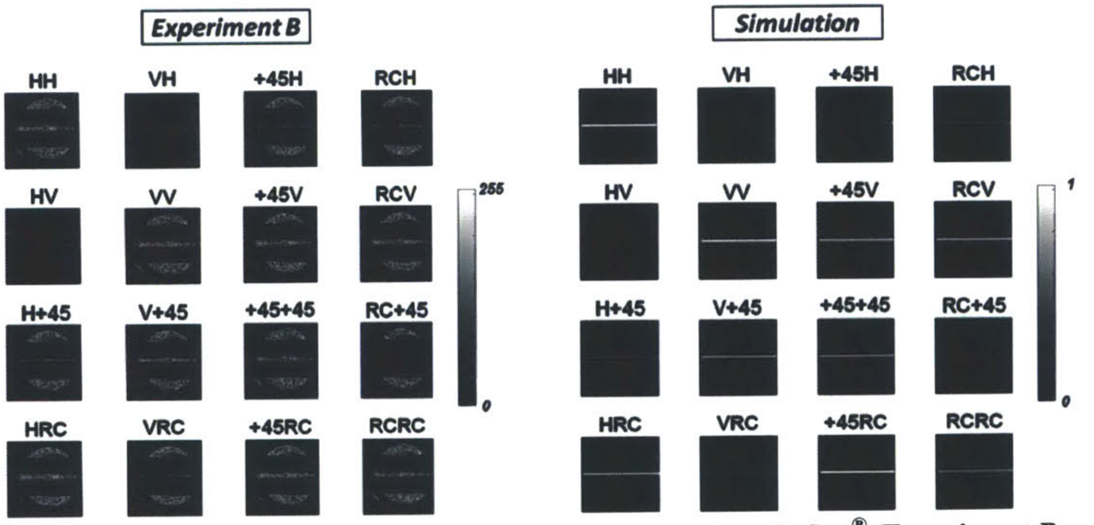

Figure 36: Polarimetric images of a cylinder wrapped in silver Teflon® (Experiment *B* vs. simulation)

5.3. Simulation of Object Signatures

Simulations were run to explore the signatures of non-resolved objects for a variety of engagement scenarios, including the monostatic interrogation of stationary and tumbling objects of different shapes and dimensions, as well as the bistatic interrogation of objects with specular reflections. Sections 5.3.1 through 5.3.3 present the results of these simulations for each engagement scenario with emphasis on the observed phenomenology. The exploitability of this phenomenology to characterize an object is discussed in Chapter 6.

5.3.1. Stationary Objects in Monostatic Geometry

The first engagement scenario is the monostatic measurement of a stationary object. When a stationary object is measured by an active polarimetric system, its orientation will not be known *a priori*. Depending on the object's orientation during the measurement, it will exhibit a different polarimetric signature. If the object assumes a random orientation, the observed polarimetric signature will also be random, according to some probability distribution. The objective of simulating stationary objects was to determine these probability distributions for several representative object shapes, including panels, spheres, and cylinders. The results of these simulations are discussed in the following sub-sections.

5.3.1.1. Panels

The first stationary object to consider is a panel, i.e., an infinitesimally thin plate, which is representative of spacecraft panels or flat shards of space debris. As shown in Figure 37(a), a panel was modeled simply as a pair of two triangular facets that form a rectangle (although a single triangular facet would have sufficed and given equivalent results). A panel was simulated for the six spacecraft materials measured in Experiment *A*. As defined in Figure 37(b), the yaw angle y between the panel's surface normal (dashed line) and the incident laser (red arrow) was varied from $y = 0$ to 90° with 1° resolution, while maintaining the same azimuth angle $\phi_i = 0$. At each yaw angle, the polarimetric signature of the panel was predicted using the measured polarimetric MRDFs from Experiment *A*.

(a) (b)

Figure 37: Simulated panel: (a) facet model; (b) yaw angle

The top row of Figure 38 shows the polarimetric properties (i.e., D, P, R, and Δ), of the simulated panels (for each material type) as functions of the yaw angle y. These plots are identical to the plots (Figure 18) of the measured monostatic properties as functions of θ from Experiment *A*. This result is expected since the stationary panels simulated here are the same as the stationary "coupon" samples measured in Experiment *A*. If it is assumed that the panel's yaw angle is drawn from a uniform distribution, then the bottom row of Figure 38 shows the resulting probability mass function (PMF) for each polarimetric property. The displayed PMFs are essentially histograms of the property values in the top row of Figure 38 with bin resolutions of 0.05 for *D*, *P* and Δ and 9° for *R*. Most of the distributions are concentrated at low values of *D*, low values of *P*, high values of *R*, and low values of Δ, except that panels with black paint and Kapton® have relatively broad distributions of *D* and *P*, panels with silver Teflon® have a broad distribution of *R* and Δ, and white paint has a narrow distribution of Δ above 0.75. These exceptions suggest the potential for some exploitability, as discussed further in Section 6.1. When considering potential exploitability, the reader is reminded here that only an active polarimetric system can estimate the properties of *D*, *R*, and Δ, while a passive system can only estimate the polarizance *P* (Section 2.5).

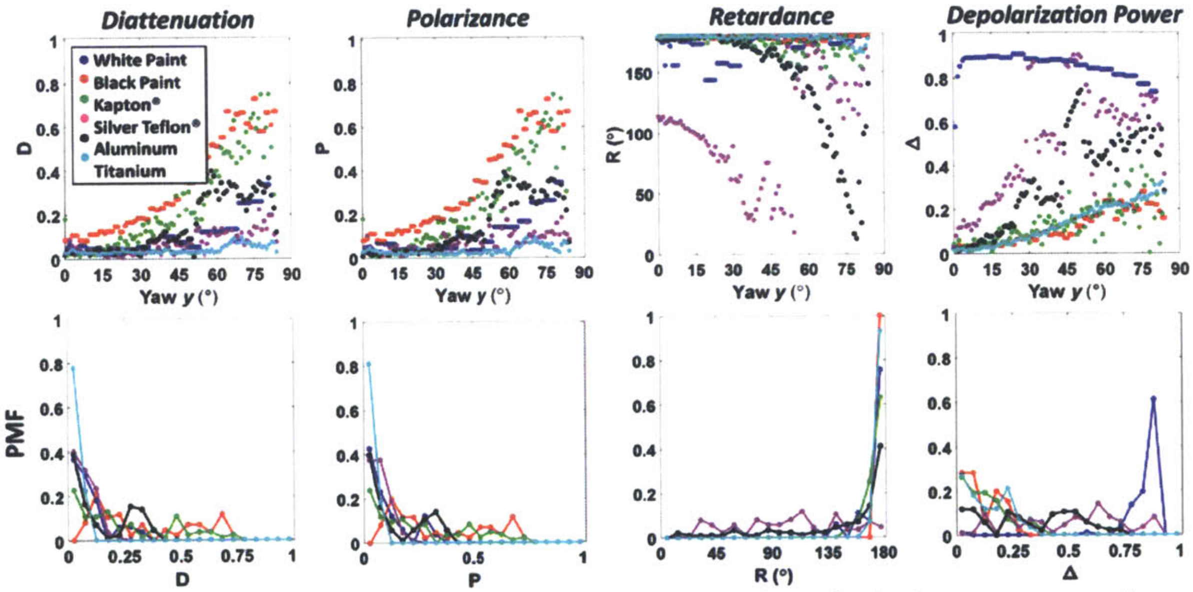

Figure 38: Simulated monostatic polarimetric properties of panels: (top) versus yaw angle; (bottom) probability mass functions

5.3.1.2. Spheres

The next stationary object to consider is a sphere, which is representative of some spacecraft bodies and chunky space debris fragments. As shown in Figure 39(a), a sphere was modeled as a set of ~3500 triangular facets, where each facet spans approximately 0.003 steradians. The facets of a sphere exhibit different azimuth angles ϕ_i, with respect to the incident laser, so the simulation could only handle spheres with isotropic coatings. Consequently, spheres were only simulated for two material types, i.e., glossy white paint and matte black paint, because they were the only materials shown to be isotropic in Experiment *A*. Due to its symmetry, a sphere should have the same polarimetric signature at all orientations. Regardless, the "yaw" angle of a simulated sphere was defined as the angle between a reference radius within the sphere (black line) and the incident laser (red arrow), as defined in Figure 39(b). The yaw angle *y* was varied from *y* = 0 to 90° with 5° resolution. At each yaw angle, the polarimetric signature of the sphere was simulated using the measured polarimetric MRDFs of glossy white paint and matte black paint from Experiment *A*.

(a) **(b)**

Figure 39: Simulated sphere: (a) facet model; (b) yaw angle

The top row of Figure 40 shows the polarimetric properties of the simulated spheres as functions of yaw angle. Because of the sphere's symmetry, the properties *D*, *P*, *R*, and Δ are constant at all angles. The bottom row of Figure 40 shows the corresponding PMFs, which are obviously only non-zero (i.e., with probability 100%) at the corresponding constant values from the top row.

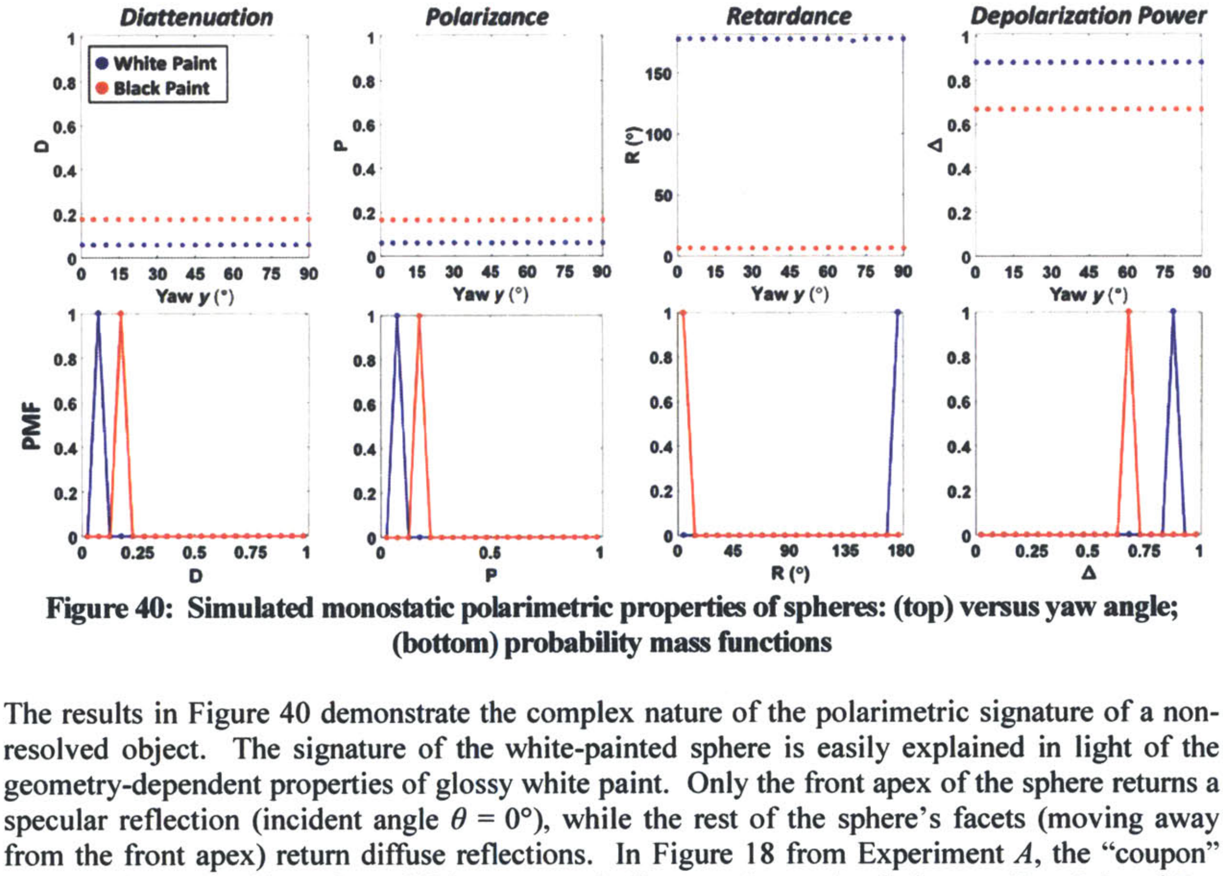

Figure 40: Simulated monostatic polarimetric properties of spheres: (top) versus yaw angle; (bottom) probability mass functions

The results in Figure 40 demonstrate the complex nature of the polarimetric signature of a non-resolved object. The signature of the white-painted sphere is easily explained in light of the geometry-dependent properties of glossy white paint. Only the front apex of the sphere returns a specular reflection (incident angle $\theta = 0°$), while the rest of the sphere's facets (moving away from the front apex) return diffuse reflections. In Figure 18 from Experiment *A*, the "coupon" sample of glossy white paint exhibits very weak diattenuation and polarizance ($D < 0.1$ and $P < 0.1$), mirror-like retardance ($R \approx 180°$), and high depolarization power ($\Delta = 0.7$ to 0.9) at all diffuse angles. Similarly, in Figure 40, the white sphere exhibits $D = 0.06$, $P = 0.06$, $R = 178°$, and $\Delta = 0.88$. Apparently, the many diffuse facets dominate the relatively small specular apex.

By contrast, the signature of the black-painted sphere contradicts the measured geometry-dependent properties of matte black paint. In Figure 18, the "coupon" sample of matte black paint exhibits steeply increasing diattenuation with angle ($D = 0.1$ to 0.8), mirror-like retardance at all angles ($R = 180°$), and slowly increasing depolarization power ($\Delta = 0$ to 0.3) with angle. However, the black sphere in Figure 40 does not completely match this behavior. On the one hand, the diattenuation ($D = 0.17$) of the black sphere makes sense, since it is within the range of geometry-dependent diattenuation ($D = 0.1$ to 0.8) exhibited by black paint. The sphere's diattenuation is weighted toward the low end of this range by the strong return of the specular facets, which themselves have relatively low diattenuation. On the other hand, the black sphere's retardance and depolarization power have no clear correspondence with the geometry-dependent behavior of black paint. In fact, the black sphere has a retardance of $R = 6°$, while black paint has a fairly constant retardance of $R = 180°$ at all incident/scatter angles. The black sphere's depolarization power ($\Delta = 0.67$) is also counterintuitive, since black paint's geometry-dependent depolarization power never rises above $\Delta = 0.5$. These discrepancies are not intuitive, but are, nevertheless, outcomes of the mathematics in Eq. 75 - Eq. 83.

The mechanism behind these discrepancies can be explained as follows. Black paint exhibits considerable diattenuation, especially at high incident angles. Recall that diattenuation is the preferential reflection of certain polarization states relative to others. These preferentially reflected polarization states (e.g., H) are geometrically defined with respect to the plane of incidence. Meanwhile, consider a ring of facets on the sphere that all lie at some distance (i.e., radius) from the front apex (i.e., center). Each facet in this ring is hit by the laser at the same incident angle, but the orientation of the plane of incidence for each facet varies uniformly from 0° to 360° (relative to the horizontal plane). Via diattenuation, each facet in the ring preferentially reflects certain polarization states that are defined with respect to its local plane of incidence. Since these planes of incidence are uniformly distributed from 0° to 360°, the entire ring returns a mix of differently-oriented, preferentially-reflected polarization states. The aggregate result for the whole sphere is an apparent depolarization, rather than a strong diattenuation. In other words, the sphere geometrically converted each facet's individual diattenuation ($D = 0.1$ to 0.8) into an aggregate depolarization power ($\Delta = 0.67$).

The simulations here show that the signature of a non-resolved object can be quite complex, even for a seemingly simple object shape like a sphere. In general, the signature of an object is a weighted sum of the polarimetric behaviors of the geometry-dependent polarimetric behaviors of its facets. In some cases (e.g., the sphere with glossy white paint), the signature bears a close resemblance to the geometry-dependent polarimetric behavior of the constituent material. In other cases (e.g., the sphere with matte black paint), the aggregate behavior is unlike that of any individual facet, due to the way the facets' behaviors combine geometrically.

5.3.1.3. Cylinders

The last stationary object to consider is a cylinder, which is representative of a spent rocket stage, spacecraft bus, or other elongated debris fragment [99]. As shown in Figure 41(a), a cylinder was modeled such that its circular perimeter is spanned by the bases of 36 triangular facets (i.e., 10° per facet). Due to its symmetry, a cylinder only needs to be varied in yaw to explore all unique orientations, as illustrated in Figure 41(b).

(a) (b)

Figure 41: Simulated cylinder: (a) facet model; (b) yaw angle

5.3.1.3.1. Broadside Cylinders

At a broadside orientation ($y = 0$), a cylinder's facets all exhibit the same azimuth angle ϕ_i with respect to the incident laser, so the simulation could handle broadside cylinders covered in any of the space materials measured in Experiment *A*. Broadside cylinders were simulated for each material type and the results are shown in Table 9. Each cylinder had a length that was twice the diameter of its circular end-cap.

Table 9: Monostatic polarimetric properties of broadside cylinders

Material Type	D	P	R	Δ
White Paint	0.02	0.01	179°	0.02
Black Paint	0.17	0.16	179°	0.03
Kapton®	0.18	0.18	178°	0.06
Silver Teflon®	0.03	0.02	114°	0.03
Aluminum	0.02	0.01	178°	0.02
Titanium	0.03	0.03	179°	0.02

For each material type, the properties of the broadside cylinder in Table 9 coincide closely with the properties (Figure 18) of the material itself at the specular point (incident angle $\theta = 0°$). This occurs because the signature is apparently dominated by the stripe of specular ($\theta = 0°$) facets occurring along the body of the broadside cylinder, as opposed to the non-specular facets outside of this stripe. For example, the white cylinder has a signature of $D = 0.02$, $P = 0.02$, $R = 179°$, and $\Delta = 0.02°$, which matches the behavior of glossy white paint at the specular point. The result stands in contrast to the white sphere (Figure 40), whose signature is dominated by the large number of diffuse facets.

5.3.1.3.2. Randomly Oriented Cylinders

If a cylinder is oriented away from broadside, its polarimetric signature will change. However, at yaw angles such that $0° < y < 90°$, the cylinder's facets assume different azimuth angles ϕ_i, so the simulation could only handle off-broadside cylinders with isotropic coatings. Consequently, off-broadside cylinders were only simulated for two material types, i.e., glossy white paint and matte black paint, because they were the only materials shown to be isotropic in Experiment *A*. For each of these materials, the yaw angle was varied from $y = 0$ to 90° with 1° resolution. At each yaw angle, the polarimetric signature of the cylinder was simulated using the measured polarimetric MRDFs of glossy white paint and matte black paint from Experiment *A*. Once again, each cylinder had a length that was twice the diameter of its circular end-cap. The top row of Figure 42 shows the polarimetric properties of the simulated cylinders as functions of yaw angle. The bottom row of Figure 42 contains the corresponding PMFs.

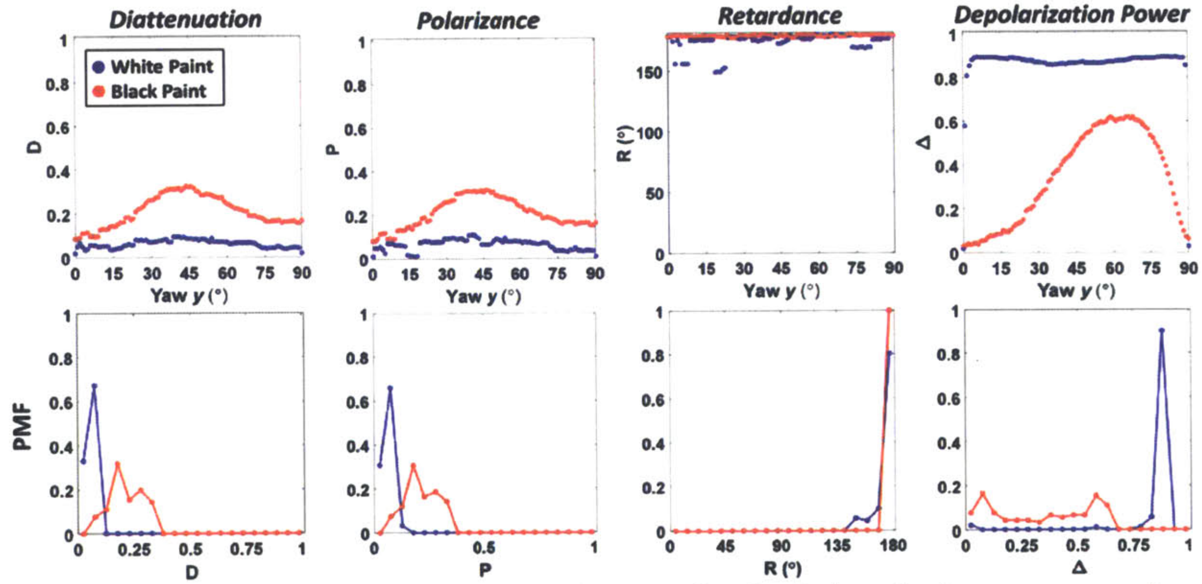

Figure 42: Simulated monostatic polarimetric properties of cylinders: (top) versus yaw angle; (bottom) probability mass functions

Figure 42 further demonstrates the complexity of the polarimetric signature of an arbitrarily oriented object. A cylinder is different than the two previously considered object shapes, in that its facets present a range of incident angles (unlike the panel) and it is not rotationally symmetric (unlike the sphere). As a result, a cylinder's polarimetric signature has a complex dependence on its orientation (i.e., yaw) that further depends on its constituent material. In Figure 42, the white-painted cylinder has a fairly constant polarimetric signature (i.e., $D < 0.1$, $P < 0.1$, $R \approx 180°$, and $\Delta \approx 0.89$) with respect to yaw angle, except around $y = 0°$ and $90°$, where the signature is dominated by the cylinder's specular broadside stripe and end-cap, respectively, and the depolarization power drops to $\Delta \approx 0$ (identical to glossy white paint's behavior at $\theta = 0°$). This result coincides with the constant polarimetric behavior of glossy white paint in the diffuse regime (Figure 18). By contrast, the black-painted cylinder has a considerable dependence on yaw angle. The black cylinder's retardance is constant at $R = 180°$, but its diattenuation varies from $D = 0.09$ at broadside ($y = 0°$) to $D = 0.35$ at $y = 45°$ and down to $D = 0.2$ on its end ($y = 90°$), and its depolarization power varies from $\Delta \approx 0$ at broadside to $\Delta = 0.65$ at $y = 65°$ and back down to $\Delta \approx 0$ on its end. The convex shape of the D and Δ plots (as a function of yaw) occur because the signature wavers from being dominated by specular facets at broadside and on-end to being more weighted by diffuse facets in between. The marked difference in yaw-dependence between the two materials is reflected in the white cylinder's narrow PMFs and the black cylinder's broad PMFs in the bottom row of Figure 42. If a stationary cylinder-shaped object is interrogated when it is randomly oriented, its observed properties will be governed by these distributions. A narrow PMF of polarimetric properties, as with a white cylinder, would allow the constituent material to be more easily identifiable, whereas a broad PMF would make any distinction less clear.

5.3.1.3.3. Short and Long Cylinders

Another parameter to consider is the ratio of the cylinder's length to the diameter of its end-cap. Short and long cylinders (relative to their diameter) will have different signatures. To explore this dependence, white-painted and black-painted cylinders were simulated for different ratios of length to diameter, i.e., 1, 2, 5, 20, and 50. For each combination of material and length-to-diameter ratio, the yaw angle was varied from $y = 0$ to 90° with 1° resolution.

The top and bottom rows of Figure 42 show the PMFs for the white and black cylinders, respectively. The results reveal that for both white and black paint, a cylinder's PMFs tend to broaden with increasing length-to-diameter ratio. This makes sense as follows. The end-cap and a single axial slice of the curved body of a cylinder each exhibit a different polarimetric behavior. As the cylinder becomes longer, its signature becomes more dominated by the curved body's behavior, which broadens the range of signatures exhibited by the entire cylinder at different orientations. Even so, the effect on the PMFs is not substantial. For example, the PMF for the diattenuation of a white cylinder has a range of $D = 0$ to 0.15 for a length-to-diameter ratio of 1 and range of $D = 0$ to 0.25 for a ratio of 50. Consequently, short and long cylinders covered in the same material have roughly the same polarimetric signature. This connotes a certain degree of robustness to the relative dimensions of an object. However, as shown in Section 5.3.1.4, the value of this robustness may be limited. A short cylinder may look the same as a long one, but may not look the same as another non-elongated object, such as a sphere.

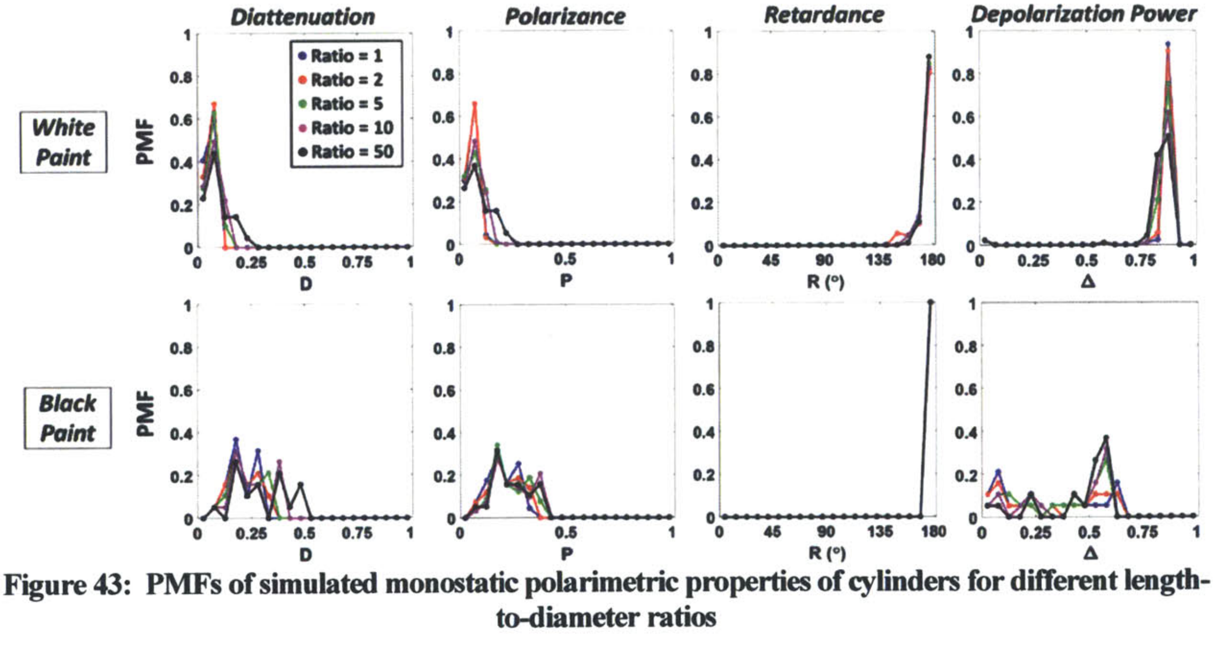

Figure 43: PMFs of simulated monostatic polarimetric properties of cylinders for different length-to-diameter ratios

5.3.1.4. Random Shape and Orientation

The previous sub-sections discussed stationary objects with representative shapes. However, in the context of space surveillance, the shape of a space debris fragment is likely to be arbitrary and unknown *a priori*. In lieu of simulating objects with arbitrary shapes, Figure 44 overlays the PMFs of the panels, spheres, and cylinders (length-to-diameter ratio of 2) from the previous sub-sections. Only objects with glossy white paint and matte black paint were considered due to their isotropy. The results reveal that objects with the same material may or may not have the same signature for different object shapes. For instance, the signature of a white-painted object is robust to object shape. The PMFs for a white sphere and white cylinder are almost identical, while the PMFs of a white panel are in the same range (per D, P, R, and Δ) but only slightly broader. By contrast, the signature of a black-painted object depends significantly on object shape. The PMFs for a black panel, sphere, and cylinder bear little resemblance with another. This suggests it may be difficult to identify an object's constituent material independent of its shape. On the other hand, if an object's constituent material is known *a priori*, its shape may be inferred from its PMF estimated through repeated interrogations.

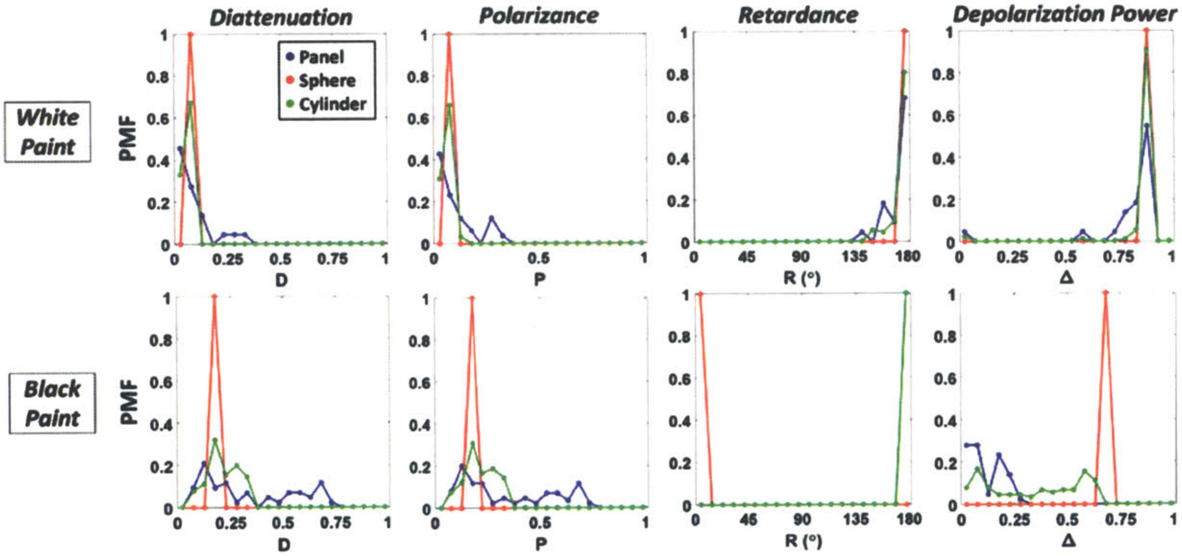

Figure 44: PMFs of simulated monostatic polarimetric properties of different object shapes

5.3.2. Tumbling Objects in Monostatic Geometry

The next engagement scenario is the monostatic measurement of a tumbling object. The effect of tumbling will depend on how the tumbling rate compares to the measurement rate. Simulations were run for two tumbling behaviors: slow and fast. The goal of these simulations was to determine the effect of tumbling on an object's signature and consider the challenges and opportunities presented by tumbling objects.

5.3.2.1. Slow Tumble

The first tumbling behavior to consider is a slow tumble. Here the object is assumed to be tumbling so slowly (relative to the measurement rate) that the observed signature is still approximately that of a stationary object. As a result, if the object's orientation at the moment of interrogation is unknown *a priori*, then its signature at that moment will be drawn from the distributions (i.e., the PMFs) for stationary objects, as in Section 5.3.1. Since the object is tumbling, a subsequent interrogation at another random time would yield a different signature drawn from same distributions. Exploitability of the signatures of slowly tumbling objects through repeated interrogation is discussed further in Chapter 6.

5.3.2.2. Fast Tumble

The second tumbling behavior to consider is a fast tumble. Here the object is assumed to be tumbling so fast that each polarization measurement is taken with the object at a random orientation. In this case, the observed Mueller matrix of the object is given by Eq. 85, i.e., the average Mueller matrix of the object over all orientations. Fast tumbling objects are simulated below for the case of a panel and a random shape (i.e., panel, sphere, or cylinder).

5.3.2.2.1. Panel

The first case to consider is a panel that is tumbling fast about the yaw axis (Figure 37). The Mueller matrix of a fast yawing panel was determined for the six spacecraft materials measured in Experiment *A* by simulating stationary panels over the full range of yaw angles (y = 0° to 90° with 1° resolution, while maintaining $\phi_i = 0°$) and averaging the resulting Mueller matrices. The average Mueller matrix was then decomposed to compute the rapidly yawing panel's polarimetric signature, as shown in Table 10.

Table 10: Simulated monostatic polarimetric properties of fast tumbling panels

Material Type	D	P	R	Δ
White Paint	0.02	0.01	179°	0.06
Black Paint	0.16	0.17	179°	0.06
Kapton®	0.15	0.15	178°	0.04
Silver Teflon®	0.03	0.02	114°	0.03
Aluminum	0.02	0.01	178°	0.02
Titanium	0.03	0.03	180°	0.03

All the tumbling panels exhibit essentially no depolarization power ($\Delta \approx 0$). Most of the panels exhibit a diattenuation of $D \approx 0$ and polarizance of $P \approx 0$, except for the black-painted panel and Kapton® panel ($D = 0.16$ and $P = 0.15$, respectively). This makes sense since stationary panels (Figure 38) for black paint and Kapton® exhibit values from $D = 0.1$ to 0.8 with increasing yaw, while they exhibit $D = 0$ to 0.3 for the other materials over all yaw angles. For each material, the diattenuation of the tumbling panel is weighted towards the low end of the stationary panels' range by the low diattenuation of the bright broadside panel ($y \approx 0$). All the panels exhibit a retardance of $R \approx 180°$, except the silver Teflon® panel has a retardance of $R = 114°$, which all match the retardance values of their respective stationary panels at broadside (Figure 38). It should be recalled here that only an active polarimetric system would be able to estimate the retardance (*R*) of a fast tumbling panel and, therefore, identify the unique retardance of silver Teflon®. A passive system would only be able to estimate the polarizance (*P*) (as could an active system), which is at least distinguishing of panels with black paint and Kapton®.

5.3.2.2.2. Random Shape

The second case to consider is a randomly-shaped object that is tumbling fast about the yaw axis (Figure 37). In lieu of simulating objects with arbitrary shapes, the usual three representative shapes (e.g., panels, spheres, and cylinders [length-to-diameter ratio of 2]) were simulated for purposes here. Only objects with glossy white paint and matte black paint were considered due to their isotropy. For each object shape and material, the Mueller matrix was determined by simulating stationary cases over the full range of yaw angles ($y = 0$ to 90° with 1° resolution) and averaging the resulting Mueller matrices. The average Mueller matrix was then decomposed to compute the fast yawing object's polarimetric signature, as shown in Table 11.

Table 11: Simulated monostatic polarimetric properties of fast tumbling objects with different shapes

Material Type	Object Shape	D	P	R	Δ
White Paint	**Panel**	0.02	0.02	179°	0.06
	Sphere	0.06	0.06	178°	0.88
	Cylinder	0.01	0.01	179°	0.12
Black Paint	**Panel**	0.16	0.17	179°	0.06
	Sphere	0.17	0.17	7°	0.67
	Cylinder	0.17	0.17	180°	0.42

In Table 11, the only data that are new are the signatures of the cylinders, since the signatures of fast yawing panels were just presented above and the signatures of yawing spheres are the same as stationary spheres (discussed previously). The signature of the fast yawing cylinders appears to be some weighted average of the distributions exhibited by a stationary, but randomly oriented cylinder (Figure 42). The white-painted cylinder exhibits no diattenuation or polarizance ($D \approx 0$, $P = 0$) and mirror-like retardance ($R = 180°$), in accordance with the narrow distributions of *D*, *P*, and *R* in Figure 42. The depolarization power $\Delta = 0.12$ of the yawing white cylinder is weighted down heavily by the nonexistent depolarization power ($\Delta = 0$) of a stationary cylinder at broadside or on-end ($y = 0°$ or 90°, respectively) as opposed to the high depolarization power ($\Delta = 0.89$) at other orientations. The black-painted yawing cylinder has mirror-like retardance ($R = 180°$), as does a stationary black cylinder at any orientation. Its depolarization power ($\Delta = 0.42$) lies near the middle of the depolarization powers exhibited by a randomly oriented, stationary black cylinder.

Overall, Table 11 demonstrates that a fast tumble, for a given constituent material, does not diminish the dependence of a signature on the object's inherent shape, despite the expectation that tumbling might blur this distinction. The dependence on shape is most evident in the exhibited depolarization power of the white-painted objects. White-painted panels, spheres, and cylinder (that are fast tumbling) all exhibit the same values of diattenuation ($D \approx 0$), polarizance ($P \approx 0$), and retardance ($R \approx 180°$). However, the only shape to exhibit strong depolarization is the sphere ($\Delta = 0.88$). This stands as another examples in which only an active polarimetric system would be able differentiate a sphere from other shapes based on the estimated depolarization power.

5.3.3. Objects in Bistatic Geometry

The last engagement scenario to be discussed is the bistatic measurement of objects with strong specular reflections. As discussed earlier, the simulation developed here can only, in general, predict the signatures of objects measured in a monostatic geometry, because the simulation would need to be fed out-of-plane polarimetric BRDFs in order to handle bistatic geometries. Nevertheless, the current simulation can still handle the degenerate case in which an object's bistatic signature is dominated by a specular reflection, because Experiment *A* did measure bistatic specular reflections at several incident angles (θ_i = 15°, 30°, 45°, 60°, 75°). The possibility of a signature being dominated by a specular reflection was already demonstrated by the monostatic signatures presented above, e.g., the stationary panels at a yaw angle of $y = 0°$ and stationary cylinders at broadside and on-end.

In the following analysis, it is assumed that an object is being interrogated in a bistatic geometry and that the resulting signature is being dominated by specular reflections from a crop of surface facets. If the laser and receiver are separated by an angle of $2\theta_i$, then these specular reflections would arise from facets being illuminated at an incident angle of θ_i with the receiver lying in the plane of incidence to receive the specular reflection. In this scenario, the signature of the object would match the behavior of the specular reflection of the constituent material for an incident angle of θ_i. Figure 45 plots the resulting signature for all the materials from Experiment *A* at incident angles of θ_i = 15°, 30°, 45°, 60°, and 75°. The data points are identical to the property values from Figure 17 at the specular points, i.e., at $\theta = \theta_i$. Of particular note are the plots of diattenuation. The paints and Kapton® exhibit a peak diattenuation at an angle of θ_i = 60° (and decreasing diattenuation away from this point), which indicates that θ_i = 60° is nearest to the respective Brewster's angles of these materials. According to Fresnel's laws of reflection, perfect diattenuation is achieved at Brewster's angle, at which point no p-polarized light is reflected [80].

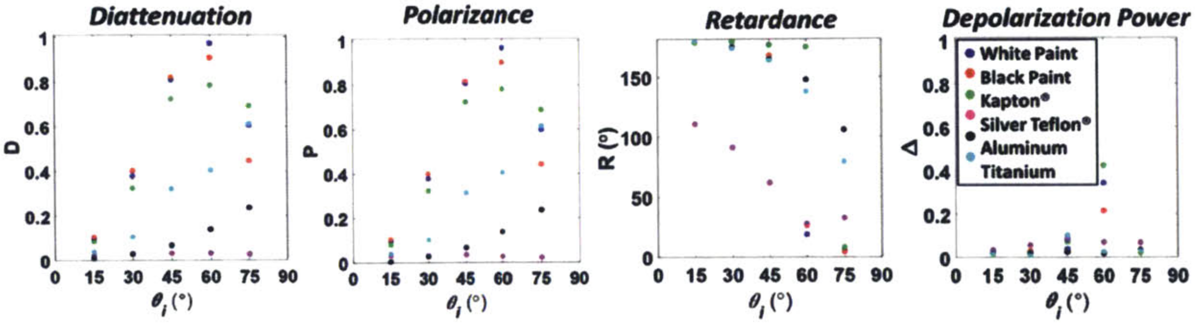

Figure 45: Measured polarimetric properties of bistatic specular reflections from Experiment *A*

5.4. Summary of Simulations

In summary, simulations were run to explore the polarimetric signatures of non-resolved objects for a variety of engagement scenarios, including the monostatic measurement of stationary and tumbling objects of different shapes and dimensions, as well as the bistatic measurement of objects with specular reflections. The results demonstrated that the signature of a non-resolved object is complex in origin, but can be described as the weighted sum of the geometry-dependent polarimetric behaviors of its facets. In some cases (e.g., a white-painted sphere in a monostatic geometry), the signature bears a close resemblance to the geometry-dependent polarimetric behavior of the constituent material, while in other in other cases (e.g., a black-painted sphere), the signature is unlike the behavior of the constituent material, due to the way the facets' behaviors combine geometrically. This phenomenology was investigated for several engagement scenarios. The first scenario was the monostatic measurement of stationary objects. A randomly oriented, yet stationary object exhibits a signature that is random according to some probability distribution (i.e., the PMFs presented above). These distributions tend to be concentrated at low values of *D*, low values of *P*, high values of *R*, and low values of Δ. Some exceptions to this trend include the broad range of retardance and diattenuation values exhibited by randomly oriented panels covered in silver Teflon® and matte black paint, respectively, and the high depolarization power exhibited by white-painted panels and cylinders.

Another engagement scenario was the monostatic measurement of tumbling objects. In the case of an object tumbling so slowly that its observed signature is still approximately that of a stationary object, the signature of the object will be random according to the same distribution as a randomly oriented, yet stationary object with the same shape. By contrast, a fast tumbling object exhibits a new phenomenology, such that the observed Mueller matrix will be the average Mueller matrix of the object over all orientations. The signature of a fast tumbling object depends significantly on its shape, e.g., fast tumbling panels exhibit no depolarization power but some diattenuation (for some materials), while fast tumbling cylinders show no diattenuation but moderate to high depolarization power (for white and black paint).

The last engagement scenario investigated was the bistatic measurement of objects with a strong specular reflection. The signatures of these objects are dominated by the behavior of the crop of surface facets whose specular reflection is directed at the receiver. Diattenuation due to Fresnel reflection is particularly evident in these signatures when the angle between the laser and receiver is moderately high.

With this understanding of the phenomenology of non-resolved active polarimetry, Chapter 6 will discuss the potential exploitability of this phenomenology for characterizing objects and the implications for space surveillance.

.

This page has been intentionally left blank

6. Discussion

This chapter discusses the exploitability of non-resolved active polarimetry and its implications for space surveillance. Several opportunities are discussed for exploiting this phenomenology to characterize an object in terms of its constituent material, shape, orientation, and other features. Most of the identified opportunities depend on the observed retardance and depolarization power, which are only obtainable with an active system, as opposed to a passive one. Some challenges and limitations are also discussed, such as the overlap among the signatures of objects with different constituent materials and the potential need for *a priori* information. Measurement campaigns may be optimally planned using a look-up table that identifies the measurements required for estimating different polarimetric properties. For space surveillance applications, active polarimetry may be effectively exercised using strategic operational schemes, including short- and long-duration interrogations of objects, and repeated interrogations of tumbling objects that are synchronized with their tumbling periods. Regardless of the operational scheme, active polarimetry may be used to characterize, fingerprint, and monitor space objects in a number of unique and valuable ways.

6.1. Exploitability

The simulations in Chapter 5 suggest several potential challenges and opportunities associated with the phenomenology of non-resolve active polarimetry. The greatest challenge is that the signatures of different objects are often similar, at least for the materials and shapes considered in this study. Randomly oriented, yet stationary objects tend to have overlapping signature distributions despite having different constituent materials. In the case of panel-shaped objects, most distributions are concentrated at low values of D, low values of P, high values of R, and low values of Δ. Consequently, if a panel-shaped object is interrogated when it is randomly oriented, its observed properties are generally not indicative of a single material. Fast tumbling objects, regardless of the material, also tend to have similar signatures (again, low D, high R, low Δ).

Nevertheless, opportunities to use this phenomenology to characterize an object do exist. Some exploitation is possible through the single interrogation (i.e., one set of measurements to compute the object's Mueller matrix) of a stationary or slowly tumbling object, e.g., monostatic measurements of a panel. Despite the overlap among the distributions for panel-shaped objects with different constituent materials (Figure 38), there are a few notable exceptions. For example, the only panels to ever have a diattenuation of $D > 0.5$ are the ones covered in black paint or Kapton® (oriented at relatively high yaw angle of $y > 60°$). Therefore, if a randomly oriented panel exhibits a diattenuation of $D > 0.5$ and the six materials studied here are the only possible identities, then one could conclude that the panel must be painted black or covered in Kapton®. The same can be said when considering the polarizance (P) of a randomly oriented panel, since polarizance values followed trends similar to diattenuation. Another instance to consider is when the observed depolarization power of a panel is very high. Specifically, if the observed value is $\Delta = 0.85$, then the only two possible materials are white paint and silver Teflon®. Since white paint and silver Teflon® panels (randomly oriented) exhibit $\Delta = 0.85$ with approximate probabilities of 0.5 and 0.05, respectively, one could conclude that the panel has a 91% and 9%

chance of being covered in white paint and silver Teflon®, respectively. Again, this assumes that the six materials here are the only possible materials and that they are equally likely to be present. A similar opportunity for exploitation exists for the property of retardance. Only aluminum and silver Teflon® panels ever exhibit values of $R < 130°$, such that an observed low retardance would narrow down the possible identities to these two materials (with a stronger indication for silver Teflon®). The examples cited here are technically only applicable to the case of panel-shaped objects with this exact set of possible constituent materials. However, they demonstrate the potential for identifying, narrowing down, or classifying the constituent material of an object, especially if the object's approximate shape and list of possible material types is known *a priori*.

A single interrogation may also be useful for objects with strong bistatic specular reflections (Figure 45). Depending on the angle of separation $2\theta_i$ between the laser and receiver, the constituent material of the object may be identified or categorized. For example, when $\theta_i = 45°$ or 60°, only specular objects covered in glossy white paint and Kapton® exhibit $D > 0.5$ or $P > 0.5$, due to the polarizing nature of Fresnel reflection at moderately high incident angles. Matte black paint also exhibits $D > 0.5$ (and $P > 0.5$), except this coating does not exhibit a specular reflection. In terms of retardance, only objects covered in silver Teflon® exhibit values in the $R < 130°$ range for incident angles $\theta_i < 45°$. Of course, in order to exploit a bistatic specular signature, the object must be interrogated at a moment at which the specular reflection hits the receiver. This type of planning and synchronization is one of the potential strategies discussed next for space surveillance applications.

Further exploitation may be possible through repeated interrogation of a slowly tumbling object. Depending on the shape and material of the object, a single interrogation may be useful enough. However, since the object is, in fact, tumbling, a new opportunity arises that can take advantage of the freely offered rotational diversity. For a single interrogation, the signature of a slowly tumbling object will be drawn from a probability distribution as if the object was stationary but randomly oriented. Subsequent interrogation would yield a different signature according to the same distribution. Consequently, repeated interrogation of a slowly tumbling object would provide an estimate of this distribution, which may be indicative of its constituent material, if its shape is known *a priori*, or its shape, if its constituent material is known *a priori*. In general, narrow distributions correspond to materials whose polarimetric behavior is not significantly geometry-dependent (e.g., glossy white paint) and object shapes with significant rotational symmetry (e.g., a sphere). By contrast, broad distributions correspond to materials whose polarimetric behavior is significantly geometry dependent (e.g., black and white paint) and object shapes lacking rotational symmetry (e.g., panels and cylinders). One could use a matched filter scheme [100] to compare the observed distribution to a bank of known distributions. This technique may be more robust if the distributions for several polarimetric properties are considered simultaneously.

Fast tumbling objects can also be exploited. Despite the expectation that tumbling might blur an object's signature such that any distinction between shapes and materials is lost, the simulations demonstrated that some exploitability may still be possible. For example, a fast tumbling panel covered in silver Teflon® still exhibits that distinct retardance of $R = 114°$ (Table 10). The signature of a fast tumbling object may also be indicative of its shape, since fast tumbling panels exhibit no depolarization power but some diattenuation (for some materials), while fast tumbling cylinders show no diattenuation but moderate to high depolarization power (for white and black paint) (Table 11).

In summary, many of the opportunities for exploiting the phenomenology of non-resolved polarimetry would only be possible with an active polarimetric system. A passive system is only able to estimate a target's polarizance P (Section 2.5), which can only be exploited in some circumstance For instance, a high polarizance ($P > 0.5$) in a bistatic specular reflection is indicative of paints and Kapton®, compared to the low polarizance of metallic surfaces (e.g., aluminum). However, polarizance is not a distinguishing factor in most other circumstances. For example, silver Teflon® exhibits a unique distribution of retardances ($R < 113°$) in the case of a slow tumbling panel and a unique retardance of $R \approx 114°$ in the case of a fast tumbling panel, but not a unique polarizance signatures. In the case of a fast tumbling object with white or black paint but of unknown shape (Table 11), polarizance is not indicative of any particular shape, but a high depolarization power ($\Delta > 0.6$) is indicative of a sphere. Therefore, an active polarimetric system would be needed to probe the retardance and depolarization power of a target and make these distinctions.

6.2. Measurement Requirements

It has been implicitly assumed throughout this thesis that the objective of active polarimetry is to estimate the Mueller matrix of a target. However, depending on the application and the exact polarimetric properties that one is trying to exploit, it may not always be necessary to determine the entire Mueller matrix. If only a subset of the 16 Mueller matrix elements needs to be estimated, then only a subset of the 16 prescribed polarization pairs (Table 1) needs to be measured. The minimum set of measurements required to estimate any of the Mueller matrix elements can be determined from Eq. 22, repeated here:

Eq. 86

$$I_{TxRx} = s_0^{Rx} = \sum_{i=0}^{3} m_{0i}^{Rx} \sum_{j=0}^{3} s_j^{Tx} m_{ij}$$

Eq. 86 indicates which intensity measurements I_{TxRx} are functions of which Mueller matrix elements m_{ij}, by virtue of the non-zero elements of the transmitted (Tx) Stokes vector $\vec{S}^{Tx}$ and the Mueller matrix M^{Rx} of the receiver (Rx) optics. For example, suppose that only the top-left elements m_{00} of the Mueller matrix is of interest. According Eq. 22, m_{00} can be estimated from a single intensity measurement I_{UU} at polarization pair UU, i.e., transmitting unpolarized light and receiving unpolarized light. This can be concluded as follows. The Stokes vector for an unpolarized laser beam is $\vec{S}^U = [1\ 0\ 0\ 0]^T$ (Eq. 2), where the only non-zero element is $s_0^U = 1$. Meanwhile, the receiver matrix M^U for receiving unpolarized light is

Eq. 87

$$M^U = \begin{bmatrix} 1 & 0 & 0 & 0 \\ 0 & 0 & 0 & 0 \\ 0 & 0 & 0 & 0 \\ 0 & 0 & 0 & 0 \end{bmatrix}$$

where the only non-zero element is $m_{00}^U = 1$. Plugging $\vec{S}^U$ and M^U into Eq. 86, the intensity measurement I_{UU} is related to m_{00} as follows:

Eq. 88 $$I_{UU} = m_{00}$$

Therefore, element m_{00} of the unknown Mueller matrix is given directly by I_{UU}. However, it should be assumed that a polarimetric laser radar would not be able to measure I_{UU}, since lasers are generally polarized (not perfectly unpolarized) and the receiver would not be able to measure unpolarized and polarized light without a beamsplitter (adding unnecessary loss) or a flip-in polarizer (inconvenient). Under the constraint that one cannot transmit or receive unpolarized (U) light, estimation of m_{00} immediately becomes more involved. In fact, the minimum set of measurements required to estimate m_{00} is {HH, HV, VH, and VV}, which results in the following system of equations:

Eq. 89
$$\begin{aligned} I_{HH} &= 0.5(m_{00} + m_{10} + m_{01} + m_{11}) \\ I_{HV} &= 0.5(m_{00} - m_{10} + m_{01} - m_{11}) \\ I_{VH} &= 0.5(m_{00} + m_{10} - m_{01} - m_{11}) \\ I_{VV} &= 0.5(m_{00} - m_{10} - m_{01} + m_{11}) \end{aligned}$$

Eq. 89 is a system of four (4) equations and four (4) unknowns (m_{00}, m_{10}, m_{01}, and m_{11}), due to the inherent coupling among these matrix elements. Consequently the set of measurements that enable the estimation of m_{00} will simultaneously enable the estimation of m_{10}, m_{01}, and m_{11}. Adding the measurement pairs {H+45, V+45}, {HRC, VRC}, {+45H, +45V}, or {RCH, RCV} to the set {HH, HV, VH, and VV} also enables estimation of m_{21}, m_{31}, m_{12}, or m_{13}, respectively. In an analogous way, the set {+45+45, +45-45, -45+45, and -45-45} enables simultaneous estimation of m_{00}, m_{20}, m_{02}, and m_{22}, and the addition of the pair {+45RC, -45RC} to this set also enables estimation of m_{32}. The set {RCRC, RCLC, LCRC, and LCLC} enables simultaneous estimation of m_{00}, m_{30}, m_{03}, and m_{33}, and the addition of the pair {RC+45, RC-45} to this set also enables estimation of m_{23}. In summary, estimation of m_{00}, m_{10}, m_{01}, m_{11}, m_{20}, m_{02}, m_{22}, m_{30}, m_{03}, or m_{33} requires 4 total active measurements, while estimation of m_{21}, m_{31}, m_{12}, m_{13}, m_{32}, or m_{23} requires 6 total active measurements. Estimation of a single element from the former or latter group enables simultaneous estimation of 3 or 4 other elements, respectively.

The measurement requirements for estimating specific polarimetric properties follow intuitively from here. Some properties, e.g., retardance (R) and depolarization power (Δ), can only be computed after decomposing the full Mueller matrix. Therefore, estimation of R and Δ requires the usual 16 measurements that are needed to estimate the entire Mueller matrix first. Other properties do not require the estimation of the full Mueller matrix. For example, according to Eq. 12 and Eq. 16, the diattenuation vector $\vec{D}$ and diattenuation D can be computed from the first row of the Mueller matrix, i.e., elements m_{00}, m_{01}, m_{02}, and m_{03}. Therefore, the estimation of $\vec{D}$ and D requires the measurement set {HH, HV, VH, VV, +45H, +45V, RCH, RCV}, which are needed to estimate these underlying Mueller matrix elements. Similarly, the polarizance vector $\vec{P}$ and polarizance P (Eq. 12) can be computed from the first column of the Mueller matrix, i.e., elements m_{00}, m_{10}, m_{20}, and m_{30}. Therefore, estimation of $\vec{P}$ and P requires the measurement set {HH, HV, H+45, HRC, VH, VV, V+45, VRC}.

The analysis above can be summarized in the form of a look-up table (Table 12) that lists the measurements required to estimate any individual Mueller matrix element or polarimetric property. For comparison, measurement requirements are provided for both passive (Rx-control only) and active (Tx- and Rx-control) systems, where it is assumed that neither type of system can receive unpolarized light (i.e., Rx $\neq$ U) and an active system cannot transmit unpolarized light (i.e., Tx $\neq$ U) for the practical reasons mentioned previously. As indicated in the table, a passive system can only estimate the first column (m_{00}, m_{10}, m_{20}, and m_{30}) of the Mueller matrix, which includes the polarizance vector $\vec{P}$ and polarizance (P). Despite this limitation, it is worth noting that a passive system can estimate these properties with fewer measurements (e.g., 4 passive vs. 8 active measurements to estimate P), due to the unique Stokes vector $\vec{S}^U = [1\ 0\ 0\ 0]^T$ of unpolarized sunlight that is unavailable to an active system.

If the exact elements and polarimetric properties that one wants to exploit are known beforehand, measurement campaigns may be optimally planned by referencing Table 12 and only performing the required measurements. This type of planning will minimize the time required to interrogate an object and therefore maximize the number of objects than can be interrogated over a given period of time. Reduced interrogation times also mean that faster tumbling rates may become negligible.

Table 12: Look-up table of measurement requirements for estimating different polarimetric properties, assuming it is impossible to receive or transmit (for active) unpolarized light

Polarimetric Property	Passive		Active	
	Rx	# of Meas.	TxRx	# of Meas.
M, R, and Δ			HH HV H+45 HRC VH VV V+45 VRC +45H +45V +45+45 +45RC RCH RCV RC+45 RCRC	16
D			HH VH +45H RCH HV VV +45V RCV	8
P	H V +45 RC	4	HH HV H+45 HRC VH VV V+45 VRC	8
m_{23}			+45+45 +45-45 -45+45 -45-45 RC+45 RC-45	6
m_{13}			HH HV VH VV RCH RCV	6
m_{12}			HH HV VH VV +45H +45V	6
m_{32}			+45+45 +45-45 -45-45 -45+45 +45RC -45RC	6
m_{31}			HH HV H+RC VH VV V+RC	6
m_{21}			HH HV H+45 VH VV V+45	6
m_{30}	RC LC	2	RCRC RCLC LCRC LCLC	4
m_{03} and m_{33}				
m_{20}	+45 -45	2	+45+45 +45-45 -45+45 -45-45	4
m_{02} and m_{02}				
m_{00} and m_{10}	H V	2	HH HV VH VV	4
m_{01} and m_{11}				

6.3. Implications for Space Surveillance

The exploitability of active polarimetry can be discussed in the context of space surveillance. A critical aspect of using active polarimetry for space surveillance will be the ability to embrace, rather than shun the tumbling behavior of space objects. While most active satellites have attitude control and therefore predictable orientations [30], space debris is uncontrolled and can have tumbling rates from 0.1s to 10s of degrees per second [29]. The tumbling period of a space object will likely not be known *a priori*. However, passive telescopes can often ascertain an object's tumbling period using "light curves," i.e., monitoring the brightness of an object as a function of time and noting the periodicity [20]. A laser radar may also determine the tumbling period by monitoring fluctuations in the object's return versus time (for a constant polarization pair). If the tumbling rates of space objects can be estimated or at least bounded, several operational schemes are possible for interrogating objects with a ground-based laser radar, including single short-duration interrogations, single long-duration interrogations, and interrogations of tumbling objects that are synchronized with their tumbling periods. Using active polarimetry, space objects may then be characterized, fingerprinted, and monitored in a number of unique and valuable ways.

6.3.1. Operational Schemes

The most basic operational scheme is a single, *short-duration* interrogation of a space object. The idea is to quickly estimate the signature of the object before it rotates substantially so that it can be considered stationary. If thousands of laser pulses are required per polarization measurement (which is typical for a reasonable probability of detection) and 16 polarization measurements are required per interrogation, then a laser system with a pulse repetition frequency (PRF) of 100 Hz [9] (i.e., 100 pulses per second) would take ~160 s to complete a single interrogation [9]. If an object is considered stationary when it rotates only 5° during an interrogation, then this limits the allowable tumbling rate to ~0.03°/s (i.e., 5° divided by 160 s). Therefore, only space debris with the slowest of tumbling rates would meet the criteria of a "stationary" object. This constraint would be mitigated if fewer polarization measurements were needed per interrogation (e.g., 4 for estimating D). Short-duration interrogations could also be repeated for the purpose of estimating the distribution of polarimetric signatures offered by a tumbling object. Because the object must be approximately stationary during each interrogation, this scheme is once again constrained to space objects with the slowest of tumbling rates. As described earlier, the observed distribution of polarimetric properties could be compared to a bank of distributions for possible material types and object shapes.

The next simplest scheme is a single, *long-duration* interrogation of a space object. The idea here is to make polarization measurements of a space object over a long period of time, during which the object ideally completes at least one tumbling period. A typical LEO object will be in view of a ground station for about 12 minutes, e.g., a circular orbit with an altitude and inclination of 1,000 km and 28.5°, respectively, when viewed from Hawaii with a minimum elevation angle of 3°) [30]. With this timeframe, the object would need to have a tumble rate of at least 0.5°/s (as the majority of debris do [29]) to complete one 360° rotation during a single pass. The minimum required tumbling rate will be lower for objects with higher orbital altitudes and will vary depending on the location and constraints of the ground station. To ensure evenly weighted averaging over all orientations, it may be necessary to interrogate an object over several ground passes. Under the condition that the object is interrogated over one or several tumbling periods, the observed Mueller matrix will be the average Mueller matrix of the object over all achieved orientations, i.e., the same as a fast tumbling object. The simulations above demonstrated that fast tumbling objects with different constituent materials can have distinguishing polarimetric signatures, e.g., a fast tumbling panel with silver Teflon® has a distinct retardance of $R = 114°$, compared to the mirror-like retardance of $R = 180°$ exhibited by panels covered in the other material types.

Fast tumbling space objects could also be interrogated with polarization measurements that are synchronized with their tumbling periods. The fundamental challenge associated with a relatively fast tumble rate is that the object rotates significantly between sequential intensity measurements. These measurements can become intractably disconnected unless a long-duration interrogation is used to average them out, as prescribed above. However, another strategy is to synchronize the timing of these measurements with the tumbling period T of the object, which could be ascertained by an auxiliary passive telescope or the laser radar itself (via light curves). If the 16 usual polarization pairs are to be measured, the idea is to measure HH at time $t = 0$, HV at $t = T$, H45 at $t = 2T$, and so on. Through this synchronization, the object will be oriented identically for each measurement, such that it is effectively held stationary over the course of the interrogation. A different orientation could be interrogated by making these same polarization measurements at times δ, $T + \delta$, $2T + \delta$, and so on, which have all been staggered by a constant time δ. Repeating this over many orientations will lead to an estimate of the distribution of polarimetric signatures offered by the tumbling object, as was suggested for repeated, short-duration interrogations of slowly tumbling objects. What may ultimately occur is that each polarization pair (e.g., HH, HV, etc.) is measured continuously for one full tumbling period, so the measurements can be synchronously processed per orientation (or stagger tine δ). The concept is to use synchronized measurements to determine the signature of a fast tumbling object as if it was stationary at one orientation. Such a scheme may be difficult or impossible for multi-axis tumbling behaviors such as precession or nutation.

Whether an object is tumbling fast or slowly, its signature may be especially revealing at an orientation with a strong specular reflection. A specular orientation could be identified in the object's light curve and then interrogated using synchronized measurements. In Section 5.3.1, a broadside cylinder (with its specular stripe) exhibited a unique monostatic retardance ($R = 114°$) for a silver Teflon® covering and an elevated diattenuation ($D = 0.18$) for a Kapton® covering compared to $D \approx 0$ for other materials. Signatures at specular orientations may be especially useful in a bistatic geometry. As identified earlier, only specular objects covered in glossy white paint and Kapton® exhibit $D > 0.5$ when the specular comes from facets with an incident angle of $\theta_i = 45°$ to $60°$, i.e., the laser and receiver are separated in angle by $2\theta_i = 90°$ to $120°$, or 1200 to 2100 km on the ground for a LEO object with an altitude of 1000 km.

6.3.2. Debris Characterization

Regardless of the operational scheme, active polarimetry may be used to characterize and monitor space objects in a number of unique and valuable ways. The simulations in Chapter 5 demonstrate that objects can certainly have distinguishing signatures, depending on their constituent materials, shapes, and orientations. A signature may be indicative of a single material (e.g., a fast tumbling panel with $R \approx 114°$ must be made of silver Teflon®) or a single shape (e.g., a fast tumbling object painted white with $\Delta \approx 0.88$ must be a sphere). In other cases, a signature may be exclusive of certain materials, e.g., a randomly oriented panel with $D > 0.5$ cannot be metallic. Of course, these examples assume that the six spacecraft materials and three canonical shapes investigated in this research are the only possibilities. Consequently, a *priori* information may be necessary to help reduce the number of possible materials and shapes expected (e.g., based on the genealogy or other features of the object) and to focus on the properties and measurements best suited for identification and classification purposes. Polarimetric information may also be fused with RF, spectral, and orbital features to maximize discrimination power [9, 101]. Knowing a debris fragment's material type is critical for determining other characteristic such as its mass, ballistic coefficient and susceptibility to drag, potential to damage a spacecraft in a collision [2, 7, 20], source and creation mechanism, and the feasibility of removing it from orbit [21].

Active polarimetry has more to offer than the pure discrimination of materials and shapes. The polarimetric signature of an individual object may also serve as a "fingerprint" to identify that same object in the future. Such a fingerprint might be useful for associating observed objects with catalogued ones (or declaring a new object), especially if objects tracks are closely spaced or have significant uncertainty [102]. The fingerprint could also be monitored for changes that may indicate corresponding changes in the object's surfaces due to space aging and erosion [94]. The ability to remotely characterize the effects of the space environment on both space debris and active satellites would be invaluable to the success of future spacecraft development and operations, including material and orbit selection. One could also measure polarimetric "light curves," as opposed to the traditional intensity-based ones, to determine tumbling rates and behaviors. For example, the depolarization power of a black-painted cylinder (Figure 42) is a highly convex function of yaw angle that could be analyzed to calculate the period of a tumbling cylinder. Knowledge of current and changing tumbling rates is especially critical to active debris removal efforts in which the debris objects must be physically secured [37].

6.3.3. Comparison with Current Capabilities

Active polarimetry offers several advantages over current space surveillance capabilities. The foremost advantage is the ability to ascertain features of objects that are either difficult or impossible for other techniques to obtain. Compared to passive polarimetry, active polarimetry can estimate additional polarimetric features, especially retardance and depolarization power (Section 6.1), that can be indicative of certain materials and shapes or enhance an object's fingerprint. These polarimetric features may be more robust than spectral or intensity-based information, since the atmosphere is basically non-birefringent. A polarimetric laser radar can also interrogate debris any time of day, since it is not restricted by the position of the sun like a passive telescope. Compared to conventional polarimetric radars that use radio waves, active polarimetry performed at optical wavelengths (e.g., λ = 1064 nm) would be sensitive to finer surface roughness and smaller features. Finally, relative to *in situ* sensors and other space-based sensors, active polarimetry is a remote sensing technique that can be performed from a ground-station and could by demonstrated with modest modifications to current laser radars (Section 6.3.5).

Of course, active polarimetry has its disadvantages and limitations as well. Active interrogation of space objects requires several safety and legal considerations, including coordination (in the US) with the Federal Aviation Administration (FAA) and the Air Force's Laser Clearinghouse [103]. Permission of the owner may be required before illuminating certain space objects, e.g., satellites, or objects near them. Advanced laser systems also face global political concerns about the militarization of space, especially for space-based systems [30].

6.3.4. Link Budget

The potential performance of a polarimetric laser radar for space surveillance can be assessed in terms of a link budget. The beam width (or divergence) θ_T of a laser with wavelength λ and transmit aperture diameter D_T is nominally given by [104]:

Eq. 90
$$\theta_T = \frac{K_a \lambda}{D_T}$$

where K_a is the aperture illumination constant. For propagation through the atmosphere, the diameter D_T in Eq. 90 must be replaced by the Fried parameter r_0 [105] (since $D_T >> r_0$ for most systems) to account for the broadening effects of atmospheric turbulence:

Eq. 91
$$\theta_T = \frac{K_a \lambda}{r_0}$$

The peak power P_R received by a monostatic laser radar system is given by the laser range equation [104], augmented here to account for attenuation η_{pol} due to polarization filtering by the receiver:

Eq. 92
$$P_R = \frac{E_{pulse} / t_{pulse}}{R_{tgt}^2 \Omega_T} (\rho A_r) \frac{A_C}{R_{tgt}^2 \Omega_r} \eta^2 \eta_{pol}$$

where E_{pulse} is the energy per pulse, t_{pulse} is the temporal pulse width, $\Omega_T = (\theta_T)^2$ is the solid angle subtended by the transmitted beam, R_{tgt} is the range to the target, A_r is the target area, ρ is the target reflectance, Ω_r is the solid angle subtended by the reflected (i.e., scattered) light, A_c is the clear area of the receiver aperture, and η is the one-way transmittance of the atmosphere.

Assuming a coherent system in which the local oscillator power is increased to provide shot-noise limited operation, the signal-to-noise ratio (*SNR*) per pulse is given by [104]:

Eq. 93
$$SNR = \frac{P_R t_{pulse}}{hc / \lambda} \eta_D$$

where η_D is the quantum efficiency (i.e., electrons generated per photon) of the sensor, $h = 6.626 \times 10^{-34}$ J·S is Planck's constant, and $c = 2.998 \times 10^8$ m/s is the speed of light.

Table 13 Parameter values for nominal link budget

Parameter	Value	Comment
E_{pulse}	2 J	Mt. Stromlo system parameters [9]
t_{pulse}	5 ns	
λ	1064 nm	
A_c	$\pi \cdot 0.9^2$ m^2	
A_r	0.25 m^2	Nominal LEO debris object
ρ	0.1	
R_{tgt}	1000 km	
K_a	2.44	Uniform aperture illumination [104]
Ω_r	π	Standard diffuse target [104]
η	0.9	Zenith transmittance from ground to space [104]
η_{pol}	0.5	Attenuation by a polarizer for an unpolarized return, assuming a perfectly depolarizing target
η_D	0.5	Nominal [104]
r_0	7 cm	Typical value at a wavelength of 1064 nm [106]

Parameter values for a hypothetical laser radar engagement are listed in Table 13, based on specifications of the laser radar system at Mt. Stromlo [9], nominal characteristics of a debris object in LEO, and nominal environmental parameters. Plugging the values in Table 13 into Eq. 91 through Eq. 93, the SNR ratio per laser pulse is computed to be ~32. This is comparable to the SNR of 50 in Experiment *A* (i.e., since these measurements had a standard deviation of 2% of the mean), which achieved error bounds of $3\sigma_D = 0.05$, $3\sigma_R = 5°$, and $3\sigma_\Delta = 0.05$ (Section 3.4.5) on the estimated diattenuation (*D*), retardance (*R*), and depolarization power (Δ), respectively. This suggests that a ground-based polarimetric laser radar, e.g., the system at Mt. Stromlo augmented to perform active polarimetry, would have enough statistical certainty to exploit the polarimetric properties of debris objects in some situations. For example, the retardance ($R = 114°$) of a broadside cylinder (Table 9) or other fast tumbling panels (Table 10) covered in silver Teflon® would be separated from the mirror-like retardance ($R = 180°$) of other material coverings by more than $6\sigma_R = 0.1$ and would therefore be highly distinguishable. Likewise, the depolarization power ($\Delta = 0.88$) of a fast tumbling white sphere (Table 11) would be statistically distinguishable from other fast tumbling white objects of other shapes ($\Delta < 0.12$). By the same criterion, other situations would be less distinguishable, e.g., the depolarization power of a fast tumbling white panel ($\Delta = 0.06$) compared to a fast tumbling white cylinder ($\Delta = 0.12$) (Table 11). In future work, the statistical separation between different materials, shapes, and orientations should be analyzed in the context of system parameters (e.g., laser power, aperture size), the types of objects of interest (e.g., size and range), and specific discrimination algorithms (e.g., maximum likelihood estimators [MLE], matched filters, or data fusion schemes).

6.3.5. *Implementation*

Active polarimetry could be successfully demonstrated with minimal modification to an existing laser radar system. On transmit, lasers are usually already polarized, so only retarders (~1% absorption) would need to be installed. The receiver would require retarders and a polarizer (η_{pol} = 50% loss for an unpolarized return). To reduce interrogation times, different Rx polarizations could also be measured in parallel through the use of beamsplitters and multiple detectors. However, this architecture would result in a 50% signal loss per beamsplitter, which would reduce the sizes and ranges of measurable space objects. During operation, polarization switching could be done quickly with Pockels cells (~10 ns) or liquid crystal retarders (~10 ms) [107]. Alternatively, one could use a dual rotating retarder (DRR) scheme in which two rotating retarders (e.g., quarter-wave plates) are placed in the optical train: one at the output of the laser (controlling Tx) and another (followed by a linear polarizer) in front of the sensor (controlling Rx) [91, 108]. Measurements are taken continuously as each retarder rotates at its own set angular frequency. The Fourier coefficients of the time-varying intensity can be written as linear functions of the target's Mueller matrix elements, such that Fourier analysis reveals the unknown Mueller matrix. Unlike the method used in Experiment *A* and *B*, a DRR scheme avoids the need for sequential polarization switching and measurements.

7. Conclusion

This chapter concludes the thesis with a summary of all the research findings and contributions and recommendations for future work. This thesis investigated the potential utility of active polarimetry for space surveillance with an emphasis on understanding the phenomenology of non-resolved object signatures. The research took both an experimental and modeling and simulation (M&S) approach. The concept of the approach was to experimentally determine the polarimetric behavior of space materials in order to simulate polarimetric signatures of non-resolved objects covered in those materials. In Experiment *A*, measurements were conducted at a wavelength of 1064 nm to determine the polarimetric BRDF (both bistatic and monostatic) of several spacecraft materials, including glossy white paint, matte black paint, aluminum alloy, titanium allow, black Kapton®, and silver Teflon®. In Experiment *B*, polarimetric images were taken of objects that were covered in spacecraft materials to determine the objects' polarimetric signatures as if they were non-resolved. A simulation was also developed and validated by Experiment *B* to predict the polarimetric signature of non-resolved objects, given the (measured) polarimetric BRDFs of their constituent materials. The simulation was used to explore the signatures of non-resolved objects targets in a variety of engagement scenarios, including the monostatic interrogation of stationary and tumbling objects of different shapes and dimensions and the bistatic interrogation of specular objects. The experiment-and-simulation architecture in this research could be used to assess the utility of active polarimetry for any application.

The results demonstrate that the polarimetric signature of a non-resolved object is complex, but can be described as the weighted sum of the geometry-dependent polarimetric behaviors of its facets. In some cases, the signature bears a close resemblance to the behavior of the constituent material, e.g., a white-painted sphere exhibits $D = 0$, $R = 180°$, and $\Delta = 0.89$ in a monostatic geometry, which matches the behavior of glossy white paint in the monostatic diffuse regime. In other cases, the signature is unlike the behavior of any individual facet due to the way the facets' behaviors combine geometrically, e.g., a black-painted sphere exhibits $\Delta = 0.67$, unlike the behavior of matte black paint at any angle ($\Delta < 0.4$). It is shown that the effective Mueller matrix of a fast tumbling object is simply the average Mueller matrix of the object over all orientations.

Several opportunities may exist for exploiting the signatures of non-resolved objects, at least in the context of the specific materials and shapes studied here. The signature of a stationary or slowly tumbling object can help exclude certain material identities, e.g., a slowly tumbling panel-shaped object with a diattenuation of $D > 0.5$ (or polarizance $P > 0.5$) cannot be metallic based on the distribution of possible signatures of metal surfaces. A fast-tumbling panel-shaped object covered in silver Teflon® exhibits the characteristic retardance ($R = 115°$) of silver Teflon® in a monostatic geometry. The monostatic signature of a fast tumbling object can still be indicative of its shape, e.g., a white-painted sphere still exhibits a distinctly high depolarization power ($\Delta = 0.88$) compared to the low depolarization power ($\Delta < 0.12$) of a fast tumbling panel-shaped object or cylinder with the same coating. Since a passive system can only estimate an object's polarizance (P), current optical telescopes would not be able to determine and exploit many of these distinguishing features such as retardance depolarization power.

Several operational schemes for interrogating space objects with a ground-based polarimetric laser radar were proposed, including short- and long-duration interrogations and interrogations whose measurements are synchronized with the tumbling period of the object. The utility of polarimetric features is discussed in terms of the ability to discriminate between objects with different materials, shapes, and orientations, and to obtain fingerprints that can be used to identify objects in the future and monitor their changes. Active polarimetry could be demonstrated in the field through reasonable modifications to existing ground-based laser radars for space surveillance. A look-up table was proposed to determine the number of measurements required for estimating different polarimetric properties. The table may be referenced to optimally plan a measurement campaign in the field that maximizes the number of objects measurable in a given period of time.

In summary, the results of this research suggest that active polarimetry at optical wavelengths would be a valuable addition to the current suite of space surveillance techniques. The premise of this research was that the laser radars currently used to track space debris could also be used to perform active polarimetry on that debris and characterize it in a way that other techniques cannot. Compared to the spectral, polarimetric, and intensity-based features gathered by passive telescopes and the RF features obtained by radars, active polarimetry at optical wavelengths may offer more robust features that can be used to determine a debris object's material type, shape, orientation, and tumbling behavior. Passive polarimetry with telescopes can only estimate an object's polarizance, and active polarimetry with radars (at radio wavelengths) has only been used to infer an object's shape (i.e., spherical nature) and is insensitive to surface roughness that is smaller than radio wavelengths. By contrast, active polarimetry at optical wavelengths can obtain an object's Mueller matrix and its associated optical features, especially diattenuation, retardance and depolarization power, where the former two depend on the material's indices of refraction and crystalline structure, and the latter depends on fine surface roughness (smaller than radio wavelengths) and the degree of volumetric scattering.

The relative advantages of active polarimetry are evident in the context of several important observational scenarios. For example, knowledge of an object's mass and tumbling behavior is critical for future debris removal efforts [24, 37], but is difficult to obtain with current space surveillance techniques. The light curves that are traditionally used to determine tumbling rates rely on temporal fluctuations in intensity (or spectral content), which occur by virtue of an object's changing orientation and the material's index of refraction. These light curves can be difficult to interpret when intensity fluctuations are small or fast [24, 28]. Active polarimetry may overcome this by observing fluctuations in additional features, e.g., depolarization power which is a highly convex function of angle in the case of matte black paint (Figure 42) and may provide greater temporal contrast in general. Active polarimetry may also help infer a debris object's mass by identifying its material type using a hyper-dimensional array of optical polarimetric features (e.g., D, P, R, Δ), as well as intensity-based, spectral, RF, and orbital features. For instance, if a debris object's surface material can be identified as white paint (e.g., due to its strong depolarization power) or silver Teflon$^{®}$ (due to its unique retardance), and it is known *a priori* that the parent satellite's outer hull was composed of certain structural metals (e.g., aluminum or steel) with these same thermal coatings, then the density and mass (e..g., using RF size estimates) of that debris could be estimated. Another scenario in which active polarimetry can be useful is the monitoring of the long-term effects of space erosion, which may induce roughness on the surfaces of space debris and satellites and could be assessed in terms of an increase in the observed depolarization power over time. In other scenarios, the rich array of active polarimetric features can be used as a fingerprint to identify or classify individual objects and improve the ability to associate observations with previously catalogued object tracks. All of these examples address the space surveillance community's general desire to obtain as much as information about debris as possible [14]. An accurate understanding of the space debris population is critical for all future efforts to remove debris already in orbit, mitigate the creation of additional debris, and protect satellites from collisions.

7.1. Future Work

This research sets the stage for several promising avenues for future work including:

- **Phenomenology Studies**: Several aspects of the phenomenology of non-resolved active polarimetry deserve more investigation. The experiments in this research demonstrated that a materials' polarimetric behavior can depend significantly on the illumination and viewing geometry. Future experiments should be conducted to determine the polarimetric BRDFs of materials at additional geometries, including hemispherical (i.e., out-of-plane) reflection measurements to facilitate bistatic signature modeling and a swath of azimuth angles to characterize anisotropic materials [88]. Spectral dependences could also be explored for additional exploitability, although polarimetric features are generally expected to be only a slowly varying function of wavelength [55]. Experiments may be especially warranted at a wavelength of λ = 532 nm, since many laser radars operate at this wavelength [11, 90]. Additional spacecraft materials should be measured to accumulate a library of their polarimetric BRDFs and geometry-dependent Mueller matrices. In simulation, more complex and realistic shapes should be considered, including ones with concave surfaces. Overall, additional experiments and M&S are needed to better understand the phenomenology expected from real-world space surveillance targets.

- **Algorithm Development**: Given such a rich and nuanced phenomenology, robust algorithms will be needed to categorize and discriminate between the polarimetric signatures of different targets [59, 82]. Algorithms will likely need to consider more polarimetric properties than were discussed in this research, such as individual components of its diattenuation, retardance, and polarizance vectors. The optimal algorithm may need to fuse polarimetric, spectral, RF, and orbital features into one hyper-dimensional data array [101]. Depending on which polarimetric properties are deemed to be the most exploitable, operational schemes can be developed to optimize measurement campaigns and streamline post-processing.

- **System Architecture and Design**: This research nominally assumed a monostatic, ground-based laser radar for much of its analysis. However, the best system architecture and design has yet to be determined. A bistatic ground-based system, while more complex with respect to measurement planning and execution, may be able to exploit unique phenomenology related to bistatic diattenuating properties. Space-based laser radars for space debris monitoring have also been proposed in the literature [45, 44]. These systems will have the advantage (over ground-based systems) of being free of any polarization or attenuation effects of the atmosphere. Regarding polarization effects, this advantage may be overstated since the atmosphere has proven to be essentially non-birefringent [18] and polarization-preserving for the purpose of polarization-shift keying in laser communications [19].

If further laboratory experiments, simulations, and algorithm development can establish that a space object's polarimetric signature is robustly exploitable, then a field test may be appropriate in the future. An existing laser radar system could eventually be augmented to perform active polarimetry on orbiting space objects and validate the concept of operation in the field.

8. Bibliography

[1] Inter-Agency Space Debris Coordination Committee, *Stability of the Future LEO Environment,* 2013.

[2] N. J. Johnson and D. S. McKnight, Artificial Space Debris, Malabar, FL: Krieger Publishing Company, 1991.

[3] Inter-Agency Space Debris Coordination Committee, *Space Debris Mitigation Guidelines,* 2007.

[4] D. J. Kessler and B. G. Cour-Palais, "Collision frequency of artificial satellites: the creation of a debris belt," *Journal of Geophysical Research,* vol. 83, no. A6, pp. 2637-2646, 1978.

[5] J. C. Liou, "An active debris removal parametric study for LEO environment remediation," *Advances in Space Research,* vol. 47, pp. 1865-1876, 2011.

[6] NASA, *The Threat of Orbital Debris and Protecting NASA Space Assets from Satellite Collisions,* 2009.

[7] N. N. Smirnov, Ed., Space Debris: Hazard Evaluation and Mitigation, New York: Taylor and Francis, 2002.

[8] "US Strategic Command," [Online]. Available: https://www.stratcom.mil/factsheets/11/Space_Control_and_Space_Surveillance/.

[9] J. D. Eastment, D. N. Ladd and C. J. Walden, "Technical description of radar and optical sensors contributing to joint UK-Australian satellite tracking, data fusion and cueing experiment," in *Advanced Maui Optical and Space Surveillance Technologies Conference,* Wailea, HI, 2014.

[10] J. Sang, J. C. Bennett and C. Smith, "Experimental results of debris orbit predictions using space tracking data from Mt. Stromlo," *Acta Astronautica,* vol. 102, pp. 258-268, 2014.

[11] Z.-P. Zhang, F.-M. Yang, H.-F. Zhang, Z.-B. Wu, J.-P. Chen, P. Li and W.-D. Meng, "The use of laser ranging to measure space debris," *Research in Astronomic and Astrophysics.*

[12] L. Hennegrave, M. Pyanet, H. Haag, G. Blanchet, B. Esmiller, E. Samain, J. Paris and D. Albanese, "Laser ranging with the MeO telescope to improve orbital accuracy of space debris," *Proc. SPIE,* vol. 8739, pp. 87390J-87390J-12, 2013.

[13] G. Kirchner, F. Koidl, F. Friederich, I. Buske, U. Volker and W. Riede, "Laser measurements to space debris from Graz SKR station," *Advances in Space Research,* vol. 51, pp. 21-24, 2013.

[14] G. C. Giakos, R. H. Picard, P. D. Dao and P. Crabtree, "Object detection and characterization by monostatic ladar bidirectional reflectance distribution function (BRDF) using polarimetric discriminants," *Proc. SPIE, Electro-Optical Remote Sensing, Photonic Technologies, and Applications III,* vol. 7482, 2009.

[15] K. Rochford, "Polarization and Polarimetry," *National Institute of Standards and Technology.*

[16] J. R. Schott, Fundamentals of Polarimetric Remote Sensing, Bellingham, WA: SPIE Press, 2009.

[17] S. Tapia, W. I. Beavers and J. Y.-K. Gho, "Photopolarimetric observations of satellites," *SPIE,* vol. 1317, 1990.

[18] N. Gisin, G. Ribordy, W. Tittel and H. Zbinden, "Quantum cryptography," *Reviews of Modern Physics,* vol. 74, 2002.

[19] M. Toyoshima, H. Takenaka, Y. Shoji, Y. Takayama, Y. Koyama and H. Kunimori, "Polarization measurements through space-to-ground atmospheric propagation path by using a highly polarized laser source in space," *Optics Express,* vol. 17, no. 25, pp. 22333-22340, 2009.

[20] T. Schildknecht, "Short Course: Observing and Characterizing Space Debris," in *Advanced Maui Optical and Space Surveillance Technologies Conference*, Wailea, HI, 2015.

[21] J. Missel and D. Mortari, "TAMU Sweeper with Sling-Sat for Space Debris Removal," Texas A&M University.

[22] W. I. Beavers and L. W. Swezey, "Firepond ODERACS Photopolarimetry," *M.I.T. Lincoln Laboratory Project Report STK-226,* November 1994.

[23] W. I. Beavers and L. W. Swezey, "Photopolarilnetric Object Characterization and Size Measurment," *M.I.T. Lincoln Laboratory Project Report STK-234,* April 1995.

[24] J. Stryjewski, D. Hand, D. Tyker, S. Murali, M. Roggermann and N. Peterson, "Real Time Polarization Light Curves for Space Debris and Satellites," in *Advanced Maui Optical and Space Surveillance Technologies Conference*, Wailea, HI, 2010.

[25] S. Prasad, Q. Zhang and R. Plemmons, "Shape and pose recovery of solar-illuminated surfaces from compressive spectral-polarimetric image data," in *Advanced Maui Optical and Space Surveillance Technologies Conference*, Wailea, HI, 2013.

[26] C. L. Stokely, J. L. Foster, E. G. Stansbery, J. R. Benbrook and Q. Juarez, "Haytack and HAX radar measurements of the orbital debris environment; 2003," November 2006.

[27] R. Sridharan, W. I. Beavers, E. M. Gaposchkin, R. L. Lambour and J. E. Kansky, "A case study of the debris characterization by remote sensing," *M.I.T. Lincoln Laboratory Technical Report 1045,* December 1998.

[28] T. Schildknecht, E. Linder, J. Silha, M. Hager, N. Koshkin, E. Korobeinikova, S. Melikiants, L. Shakun and S. Strakhov, "Photometric monitoring of non-resolved space debris and data-bases of optical light curves," in *Advanced Maui Optical and Space Surveillances Technologies Conference*, Wailea, HI, 2015.

[29] C. R. Binz, M. A. Davis, B. E. Kelm and C. I. Moore, “Optical Survey of the Tumble Rates of Retired GEO Satellites,” in *Advanced Maui Optical and Space Surveillance Technologies Conference*, Wailea, HI, 2014.

[30] J. R. Wertz and W. J. Larson, Space Mission Analysis and Design, El Segundo, CA: Microcosm Press, 1999.

[31] G. C. Giakos, R. H. Picard, P. D. Dao, P. N. Crabtree and P. J. McNicholl, “Polarimetric Wavelet Phenomenology of Space Materials,” in *IEEE International Conference on Imaging Systems and Techniques*, Batu Ferringhi, Malaysia, 2011.

[32] J. Peterman, “Design of a Fully Automated Polarimetric Imaging System for Remote Characterization of Space Materials,” in *The Univerity of Akron*, MS Thesis, 2012.

[33] M. Reddy, “Advanced Object Characterization and Monitoring Techniques Using Polarimetric Imaging,” in *The University of Akron*, MS Thesis, 2009.

[34] J. Hanson, "The Forgotten Cold Way Plan that Put a Ring of Copper Around the Earth," *WIRED,* 13 October 2013.

[35] NASA Orbital Debris Program Office, *Chinese Anti-satellite Test Creates Most Severe Orbital Cloud in History,* 2007.

[36] NASA Orbital Debris Program, *Satellite Collision Leaves Significant Debris Clouds,* 2009.

[37] S.-I. Nishida and S. Kawamoto, "Strategy for capturing of a tumbling space debris," *Acta Astronautica,* vol. 68, pp. 113-120, 2011.

[38] NASA Orbital Debris Program Office, 2013.

[39] M. Gruss, "U.S. Plans $6 Billion Investmnet in Space Situational Awareness," *Space News,* 9 October 2015.

[40] "NASA Orbital Debris Program Office," [Online]. Available: http://orbitaldebris.jsc.nasa.gov/index.html.

[41] "ESA Space Debris Office," [Online]. Available: http://www.esa.int/Our_Activities/Operations/Space_Debris.

[42] D. T, "A Deep-Space UFO Mystery Solved," *Sky and Telescope,* p. 26, December 2002.

[43] B. Greene, G. Yuo and M. Christ, "Laser tracking of space debris," in *13th International Workshop n Laser Ranging*, Washington, D.C., 2002.

[44] J. Dong and Q. Hu, "Space debris detection with space-based avalanched photodiode laser radar," *Chines Optics Letters,* vol. 5, no. Supplement, pp. S176-S179, 2007.

[45] S. V. Garnov, A. V. Moiseeva, P. Y. Nosatenko, V. N. Fomin and A. B. Tserevitinov, "Estimation of the characteristics of a promisiing orbital lidar for space debris monitoring".

[46] "Orbtial Debris Surface Examinatons," [Online]. Available: http://orbitaldebris.jsc.nasa.gov/measure/surfaceexam.html.

[47] "Long Duration Exposure Facility," [Online]. Available: http://setas-www.larc.nasa.gov/LDEF/index.html.

[48] K. Grinter, "Retrieval of LDEF provided resolution, better data," *Spaceport News,* vol. 50, no. 1, 2010.

[49] A. Moussi, D. Drolshagen, J. McDonnell, J. Mandeville and A. Kearsley, "Results of Impact Analysis of HST Service Mission 3B Solar Arrays," in *Fourth European Conference on Space Debris*, Darmstadt, Germany, 2005.

[50] "Space Debris Monitor," [Online]. Available: http://www.ard.jaxa.jp/eng/pickup/sdm.html.

[51] J. Liou, R. Corsaro, F. Giovane, C. Anderson, A. Sadilek, M. Burchell and J. Hamilton, "DRAGONS – A Micrometeoroid and Orbital Debris Impact Sensor," in *International Symposium on Space Technology and Science*, Kobe-Hyogo, Japan, 2015.

[52] W. Bauer, O. Romberg and M. F. Barscke, "Space Environment Characterisation by applying an innovative Debris Detector," in *Advanced Maui Optical and Space Surveillance Technologies Conference*, Wailea, HI, 2015.

[53] J. Liou, "Orbital Debris Modeling," in *Canadian Space Agency*, St Hubert, Quebec, Canada, 2012.

[54] G. Stansbery and M. Matney, Interviewees, [Interview]. 21 November 2013.

[55] J. S. Tyo, D. L. Goldstein, D. B. Chenault and J. A. Shaw, “Review of passive imaging polarimetry for remote,” *Applied Optics,* vol. 45, no. 22, pp. 5453-5469, 2006.

[56] J. L. Pezzaniti and R. A. Chipman, "Mueller matrix imaging polarimetry," *Optical Engineering,* vol. 34, no. 6, 1995.

[57] P. Refregier, F. Goudail and N. Roux, "Estimation of the degree of polarization in active coherent imagery by using the natural representation," *Journal of the Optical Society of America A,* vol. 21, no. 12, 2004.

[58] S. Breugnot and P. Clemenceau, "Modeling and performance of polarimetric active imager at 806nm," *Optical Engineering,* vol. 30, no. 10, pp. 2681-2688, 2000.

[59] C. S. Chun and F. A. Sadjadi, "Polarimetric laser radar target classification," *Optics Letters,* vol. 30, no. 14, pp. 1806-1808, 2005.

[60] J. S. Baba, J.-R. Chung, A. H. DeLaughter, B. D. Cameron and G. L. Cote, "Development and calibration of a m automated Mueller matrix polarization imaging system," *Journal of Biomedical Optics,* vol. 7, no. 3, pp. 341-349, 2002.

[61] S. Demos and R. Alfano, "Optical polarization imaging," *Applied Optics,* vol. 36, no. 1, 1977.

[62] A.-B. Mahler, P. Smith, R. Chipman, G. Smith, N. Raouf, A. David, B. Hancock, G. Gutt and D. J. Diner, "High-accuracy spectropolarimetric imaging using photoelastic modulator-based cameras with low-polarization coatings".

[63] G. D. Gilbert, "Improvement of Underwater Visbility by Reduction of Backscatter with a Circular Polarization Technqiue," *Underwater Photo-Optics I, Proc. SPIE,* vol. 7, 1966.

[64] D. W. Tyler, A. M. Phenis, A. B. Tietgen, M. Virgen, J. D. Mudge, J. S. Stryjewski and J. A. Dank, "First high-resolution, passive polarimetric images of boosting rocket exhaust plumes," in *Advanced Maui Optical and Space Surveillance Technologies Conference,* Wailea, HI, 2009.

[65] M. P. Stoll and J. Zallat, "Laser polarimetry at 10.6 m and modeling of scattering by soils and particulate media," *SPIE,* vol. 3059.

[66] B. G. Hoover and J. S. Tyo, "Polarization components analysis for invariant discrimination," *Applied Optics,* vol. 46, no. 34, 2007.

[67] S. Tan and R. M. Narayanan, "Design and performance of a multiwavelength airborne polarimetric lidar for vegetation remote sensing," *Applied Optics,* vol. 43, no. 11, 2004.

[68] G. C. Giakos, L. Fraiwan, N. Patnekar, S. Sumrain, G. B. Mertzios and S. Periyathamby, "A Sensitive Optical Polarimetric Imaging Technique for Surface Defects Detection of Aircraft Turbine Engines," *IEEE Transcations on Instrumentatiojn and Measurement,* vol. 53, no. 1, 2004.

[69] G. C. Giakos, "Multifusion Multispectral Lightwave Polarimetric Detection Principles and Systems," *IEEE Transactons on Instrumentation and Measurement,* vol. 55, no. 6, 2006.

[70] M. Hayman, S. Spuler, B. Morley and J. VanAndel, "Polarization lidar operation for measuring backscatter phase matrices of oriented scatterers," *Optics Express,* vol. 20, no. 28, 2012.

[71] NOAA National Severe Storms Laboratory, "Dual-pol radar technology," 2014.

[72] D. A. Lavigne, M. Breton, M. Pichette, V. Larochelle and J.-R. Simard, "ENHANCED MILITARY TARGET DISCRIMINATION USING ACTIVE AND PASSIVE POLARIMETRIC IMAGERY," *IEEE IGARSS,* 2008.

[73] J. Hough, "Polarimetry: a powerful diagnostic tool in astronomy," *Astronomy and*

Geophysics, vol. 47, no. 3, 2006.

[74] D. Giuili, "Polarization diversity in radars," *Proceedings of the IEEE,* vol. 74, no. 2, 1986.

[75] X. Cheng, Y.-z. Li and X.-s. Wang, "Antenna polarization optimization for target detection in non-Gaussian clutter," *International Journal fo Antenna and Propagation,* vol. 2015.

[76] A. Parsa and N. H. Hansen, "Comparison of vertically and horizontally polarized radar antennas for target detection in sea clutter — An experimental study," in *IEEE National Radar Conference*, 2012.

[77] M. G. Czerwinski and J. M. Usoff, "Development of the Haystack Ultrawideband Satellite Imaging Radar," *Lincoln Laboratory Journal,* vol. 21, no. 1, 2014.

[78] "The Orbital DEbris RAdar Calibration Spheres," [Online]. Available: http://orbitaldebris.jsc.nasa.gov/measure/oderacs.html. [Accessed 2016].

[79] Z. Liu, Q. Zhong, X. Yu, Q. J. Wang and Y. Zhang, "Surface roughness measurement by depolarization method," *Applied Optics,* vol. 54, no. 18, 2015.

[80] E. Hecht, Optics, Boston: Pearson, 2002.

[81] S. R. Cloude, "Conditions for the physical realisability of matrix operatrors in polarimetry," in *SPIE Polarization Considerations for Optical Systems II,* 1989.

[82] F. Boulvert, G. Le Brun, B. Le Jeune, J. Cariou and L. Martin, "Decomposition algorithm of an experimental Mueller matrix," *Optics Communications,* vol. 282, no. 5, pp. 692-704, 2009.

[83] S.-Y. Lu and R. A. Chipman, "Interpretation of Mueller matrices based on polar decomposition," *Journal of the Optical Society of America A,* vol. 13, no. 5, pp. 1106-1113, 1996.

[84] G. Strang, Introduction to Applied Mathematics, Wellesley, MA: Wellesley-Cambridge Press, 1986.

[85] D. Goldstein, Polarization Light, New York: Marcel Decker, Inc., 2003.

[86] J. R. Taylor, An Introduction to Error Analysis: The Study of Uncertainties in Physical Measurements, Sausalito, CA: University Science Books, 1997.

[87] D. M. Hayes, "Error propagation in decomposition of Mueller matrices," in *SPIE: Polarization: Measurement, Analysis, and Remote Sensing,* 1997.

[88] J. C. Stover, Optical Scattering: Measurement and Analysis, 1995.

[89] F. E. Nicodemus, "Directional reflectance and emissivity of an opaque surface," *Applied Optics,* vol. 4, no. 7, pp. 767-773, 1965.

[90] A. B. Gschwendtner and W. E. Keicher, "Development of coherent laser radar at Lincoln Laboratory," *Lincoln Laboratory Journal,* vol. 12, no. 2, 2000.

[91] R. M. A. Azzam, "Photopolarimetric measurement of the Mueller matrix by Fourier analysis of a single detected signal," *Optics Letters,* vol. 2, no. 6, 1978.

[92] Labsphere, Inc., 2015. [Online]. Available: http://www.labsphere.com.

[93] J. E. Solomon, "Polarization imaging," *Applied Optics,* vol. 20, no. 9, pp. 1537-1544, 1981.

[94] M. R. Reddy, "Effect of low earth orbit atomic oxygen on spacecraft materials," *Journal of Material Science,* vol. 30, pp. 281-307, 1995.

[95] L. Corporation, *Aeroglaze A276 Reflective Polyurethane, Low Outgassing,* 2004.

[96] *Aeroglaze Z306 Polyurethane Coating,* Lord Corporation, 2013.

[97] D. G. Gilmore, Ed., Spacecraft Thermal Control Handbook: Volume 1 - Fundamental Technologies, 2nd ed., El Segundo, CA: The Aerospace Press, 2002.

[98] A. Willison and D. Bedard, "Light curve simulation using spacecraft CAD models and empirical material spectral BRDFs," in *Advanced Maui Optical and Space Surveilllance Technologies Conference*, Wailea, HI, 2015.

[99] R. Linares, M. Shoemaker, A. Walker, P. M. Mehta, D. M. Palmer, D. C. Thompson, J. Koller and J. L. Crassidis, "Photometric data from non-resolved objects for space object characterization and improved atmospheric modeling," in *Advanced Maui Optical and Space Surveillance Technologies Conference*, Wailea, HI, 2013.

[100] A. V. Oppenheim, A. S. Willsky and S. H. Nawab, Signals ans Systems, Upper Saddle River, NJ: Prentice Hall, 1996.

[101] R. Linares, J. L. Crassidis, C. J. Wetterer, K. A. Hill and M. K. Jah, "Astrometric and Photometric Data Fusion for Mass and Surface Material Estimation using Refined Bidirectional Reflectance Distribution Functions-Solar Radiation Pressure Model," in *Advanced Maui Optical and Space Surveillance Technologies Conference*, Wailea, HI, 2013.

[102] N. Singh, J. T. Horwood, J. M. Aristoff, A. B. Poore, C. Sheaff and M. K. Jah, "Multiple hypothesis tracking (MHT) for space surveillance: results and simulation studies," in *Advanced Maui Optical and Space Surveillance Technologies Conference*, Wailea, HI, 2013.

[103] M. Wright, M. Troy, J. Roberts, J. Kovalik and W. T. Roberts, "Recent research at the JPL Optical Communications Telescope Laboratory," in *Advanced Maui Optical and Space Surveillance Technologies Conference*, Wailea, HI, 2006.

[104] A. V. Jelalian, Laser Radar Systems, Boston: Artech House, 1991.

[105] D. L. Fried, "Optical Resolution Through a Randomly Inhomogeneous Medium for Very Long and Very Short Exposures," *Journal of the Optical Society of America,* vol. 56, no. 10, 1966.

[106] E. Hines, Interviewee, *Senior Technical Staff, MIT Lincoln Laboratory.* [Interview]. 12 May 2016.

[107] N. L. Seldomridge, J. A. Shaw and K. S. Repasky, "Dual-polarization lidar using a liquid crystal variable retarder," *Optical Engineering,* vol. 45, no. 10, p. 106202, 2006.

[108] M. H. Smith, "Optimization of a dual-rotating-retarder Mueller matrix polariemter," *Applied Optics,* vol. 41, no. 13, pp. 2488-2493, 2002.